High Resolution Neutron Spectroscopy of Excitations in Superconductors

Vorgelegt von

Nathalie Munnikes

aus Haarlem (Niederlande)

Contents

Abstract

In this work, anomalies of acoustic phonons are studied in the elemental superconductors Nb and Pb and in lead-thallium and lead-bismuth. By using high-resolution spin-echo neutron spectroscopy, energy resolutions in the range of μeV were reached, which corresponds to an improvement of several orders of magnitude compared to conventional neutron spectroscopy. Several renormalization effects and anomalies appear at phonon energies near the energy gap 2Δ and at temperatures above and below the superconducting transition temperature T_c. Whereas the relative changes of the linewidths and energies agree well with predictions based on BCS theory, the absolute values differ significantly. Surprisingly, Kohn anomalies coincide with $2\Delta(T = 0\,\mathrm{K})$ both in Nb and Pb. By means of neutron spectroscopy on several $\mathrm{Pb}_{1-x}\mathrm{Bi}_x$ and $\mathrm{Pb}_{1-x}\mathrm{Tl}_x$ alloys, it could be demonstrated that the energy gap $2\Delta(T = 0\,\mathrm{K})$ follows the energy of the Kohn anomaly as it changes in the alloys.

Abstract (German)

In dieser Arbeit wurden Anomalien akustischer Phononen in den elementaren Supraleitern Nb und Pb und in Blei-Thallium und Blei-Wismuth Legierungen untersucht. Mittels hochauflösender Spin-Echo Neutronenspektroskopie wurden Auflösungen im Bereich einiger μeV erreicht, was einer Verbesserung von mehreren Größenordnungen im Vergleich zu konventioneller Neutronenspektroskopie entspricht. Bei Phononen-Energien nahe der Energielücke 2Δ und bei Temperaturen um die Sprungtemperatur T_c treten verschiedene Renormalisierungseffekte und Anomalien auf. Während die relativen Änderungen der Linienbreiten und der Energien gut übereinstimmen mit Vorhersagen basierend auf der BCS-Theorie, weichen die Absolutwerte signifikant davon ab. Überraschend ist die Koinzidenz einer Kohn-Anomalie mit $2\Delta(T = 0\,\mathrm{K})$, sowohl in Nb als auch in Pb. Mittels Neutronenspektroskopie an verschiedenen $Pb_{1-x}Bi_x$ und $Pb_{1-x}Tl_x$ Legierungen konnte gezeigt werden, dass die Energielücke $2\Delta(T = 0\,\mathrm{K})$ der Energie der sich in den Legierungen ändernden Kohn Anomalie folgt.

1. Introduction

In conventional superconductors, itinerant electrons are bound in pairs by vibrations of the crystal lattice. The resulting composite particles, the Cooper pairs, have no net spin and a strongly correlated center of mass motion. They constitute the superconducting (sc) condensate, which can be described by a macroscopic quantum wavefunction. The electronic system decreases in energy, which manifests itself in a lack of states measured from the Fermi edge: the energy gap Δ. This course of events was successfully described by Bardeen, Cooper and Schrieffer (bcs) in 1957 [1]. The bcs theory incorporates the attractive interaction by lattice vibrations (phonons) and the repulsive Coulomb forces between the electrons in a phenomenological effective potential. Eliashberg [2] and Morel and Anderson [3] explained in a more rigorous treatment that the strong Coulomb repulsion is overcome by the slow motion of the atom cores with respect to the electrons, which leads to a time-retardation and locality in space of the electron-phonon (e-ph) interaction.

Still, the Eliashberg theory is not parameter-free. The phonon properties in the form of the e-ph coupling factor $\alpha^2(\omega)$ multiplied by the phonon density of states (dos) $F(\omega)$ for frequency ω are traditionally modeled or taken from experiment [4, 5]. The single parameter

$$\lambda = 2 \int_0^\infty \frac{\alpha^2(\omega) F(\omega)}{\omega} \mathrm{d}\omega \tag{1.1}$$

is commonly used as a measure of the strength of the e-ph coupling in a material. The neglect of any momentum dependence is in fact a simplification, as the experimental energy gap magnitude may be anisotropic. For instance, the mean square deviation

$$\beta^2 = \frac{\overline{\Delta^2} - \left(\bar{\Delta}\right)^2}{\left(\bar{\Delta}\right)^2} \tag{1.2}$$

of the gap value distribution function in Nb is slightly below $\beta^2 \approx 0.01$, which amounts to $\sim 10\%$ fluctuations [6]. In Pb, the mean square deviation is roughly 0.01 as well, with the gap being peaked around two values, 2.4 and $3\,\mathrm{meV}$ [7].

Phonon linewidths could provide the e-ph coupling parameters for individual phonon wavevectors $\mathbf{q}$ and modes j and not only integrated values, if phonon decay from other sources than electron scattering can be neglected or separated. The normal conducting

state phonon linewidth due to e-ph interactions, $\Gamma_n^{\mathrm{e-ph}}$, is a measure of the phonon's importance to superconductivity via the relation [8]

$$\alpha^2(\omega)F(\omega) = \sum_{\mathbf{q},j} \frac{\Gamma_n^{\mathrm{e-ph}}(\mathbf{q},j)}{\pi N(0)\hbar\omega_{\mathbf{q},j}} \delta(\omega - \omega_{\mathbf{q},j}), \qquad (1.3)$$

with $\hbar$ Planck's constant, $N(0)$ the electronic density of states at the Fermi surface (FS) for both spin orientations and $\hbar\omega_{\mathbf{q},j}$ the phonon energy. The Dirac δ function is used.

The two main experimental methods to study conventional superconductors are tunneling spectroscopy and neutron spectroscopy. The differential conductance through a superconductor-insulator-metal tunnel junction, which is proportional to the so-called tunneling density of states $N_T(\omega)$, gives information about the size of the superconducting gap and, for strong-coupling superconductors, about $\alpha^2 F(\omega)$. An example showing how the phonon DOS is reflected in Eliashberg's generalized energy gap function $\Delta(\omega)$ and in $N_T(\omega)$ is shown in Fig. 1.1a. The simple BCS gap Δ_0 is equal to $\mathrm{Re}\,\Delta(\omega)$ in the low energy limit. The single phonon peak model at ω_0 creates a damping in the complex energy gap and a corresponding structure in $N_T(\omega)$ at $\omega_0 + \Delta_0$. Note the shifted scale: the tunneling density of states below Δ_0 is zero. The e-ph prefactor $\alpha^2(\omega)$ is taken to be constant in this example. Indeed, variations in $\alpha^2(\omega)$ seem to be generally small, as can be seen from calculations [9] for e.g. Nb, shown in Fig. 1.1b. As the dispersion of the transverse and longitudinal acoustic phonon modes flattens at the Brillouin zone boundary, $F(\omega)$ is peaked at the maximal values of the respective branches.

In contrast to tunneling, neutron spectroscopy allows to measure the momentum-resolved phonon band structure, which determines the overall phonon density of states $F(\omega)$. The band structure and phonon linewidths may be affected locally by the e-ph interaction in the form of Kohn anomalies [10]. In one dimension in the nearly free electron approximation, a phonon with wavevector equal to the Fermi surface spanning (nesting) vector $2\mathbf{k_F}$ and with negligible energy with respect to the electronic band structure energies would be able to excite electrons from one point at the Fermi edge to the other point. This would cause an instability in the phonon dispersion and, concomitantly, a Peierls transition of the periodic lattice. In three dimensions, electron excitations across the Fermi surface may cause a dip or kink in the phonon dispersion as displayed for the case of face-centered cubic (fcc) Pb in Fig. 1.2. Phonon energies generally do not permit transitions from deeper to higher level states, so that transitions stay close to the Fermi surface. Thus, if the phonon wavevector $\mathbf{q}$ exceeds an electron pocket spanning vector (green and blue arrow in Fig. 1.2a), a group of potential transition possibilities is lost. Equally so if $\mathbf{q}$ falls short of a hole-filled Fermi surface connection (red arrow). This may translate into upward and downward kinks in the dispersion, respectively: the Kohn anomalies. Phonons may couple with various strengths to different sections of the Fermi surface. Generally, the longitudinal branch couples more strongly to the electrons than the transverse branches, as can be seen in Fig. 1.2b. The larger and less concave or convex the connected sections are, the stronger a Kohn anomaly can become.
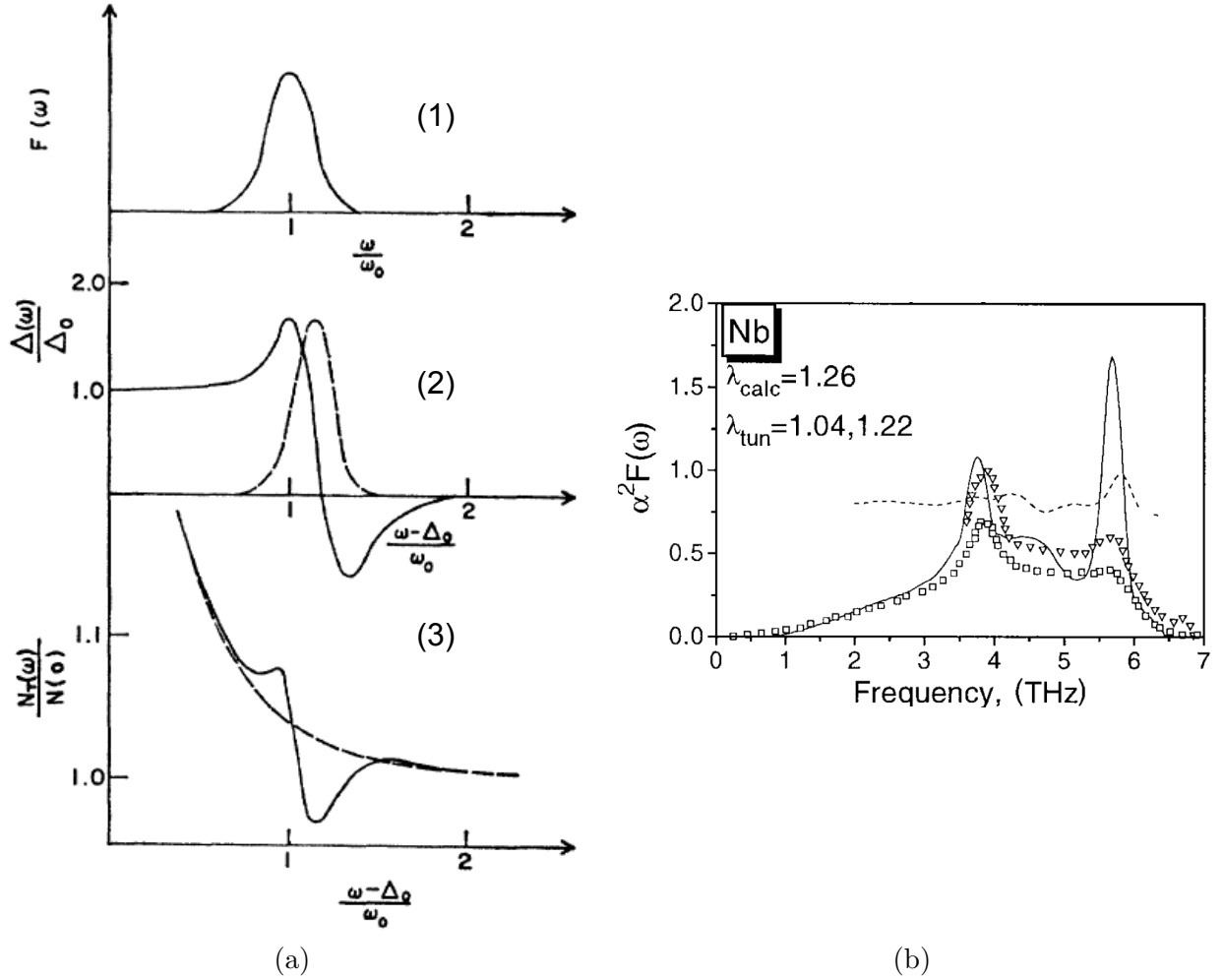
Figure 1.1.: *(a)(1) The phonon density of states $F(\omega)$ for a single phonon peak model. (2) The real (solid) and imaginary (dashed) parts of the gap function $\Delta(\omega)$ corresponding to the phonon model shown in (1). (3) The normalized tunneling density of states $N_T(\omega)/N(0)$ (solid) compared with the* BCS *form (dashed). From Ref. 4. (b) Spectral function $\alpha^2 F(\omega)$ for Nb calculated by Savrasov and Savrasov (full lines) and results from tunneling experiments (symbols). The behavior of $\alpha^2(\omega)$, defined as the ratio $\alpha^2 F(\omega)/F(\omega)$, is shown by dashed lines. From Ref. 9.*

Conventional triple-axis neutron experiments can scarcely resolve intrinsic phonon linewidths resulting from e-ph interaction. In the 1970s the Brookhaven group succeeded to observe changes of the linewidth of acoustic phonons across the superconducting transition temperature T_c in Nb [14] and Nb$_3$Sn [15]. They took advantage of the optimal spectrometer focusing condition, which only occurs for few phonons, and from the comparatively large phonon widths. A typical energy scan in the transverse acoustic phonon branch T2 along the [110]-direction in the first Brillouin zone of body-centered cubic (bcc) Nb is shown in Fig. 1.3. The phonon energy is in this case smaller than $2\Delta_0 \approx 3.1\,\text{meV}$. The absolute intrinsic linewidth in the superconducting state is assumed to be close to zero, as the
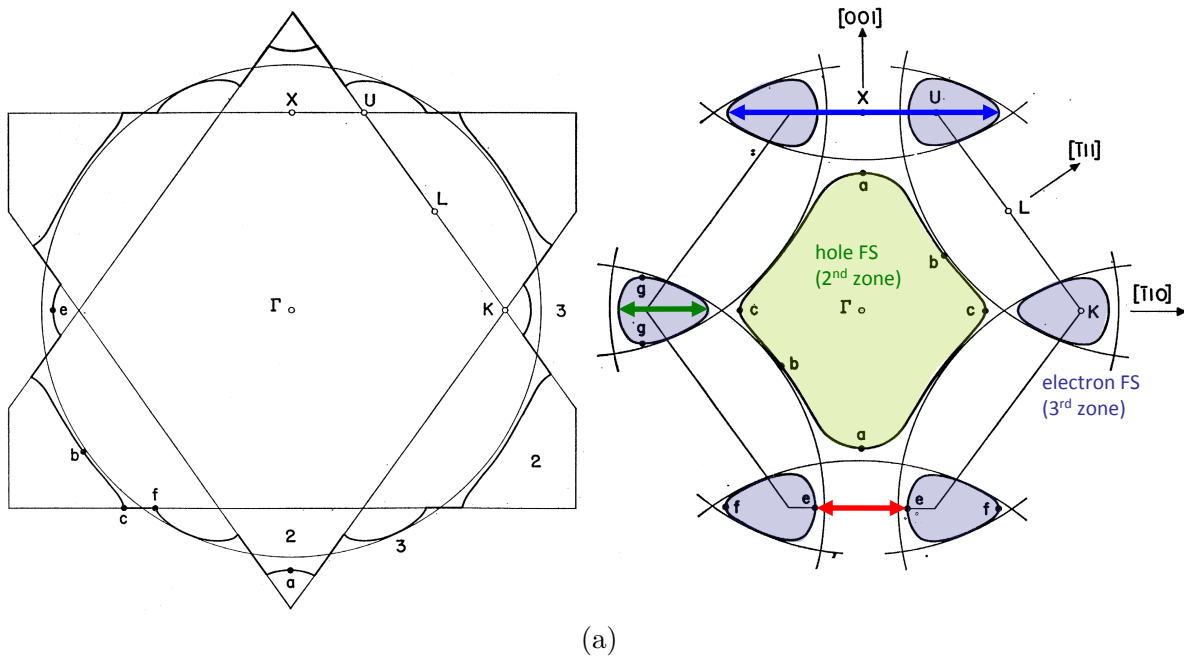
(a)
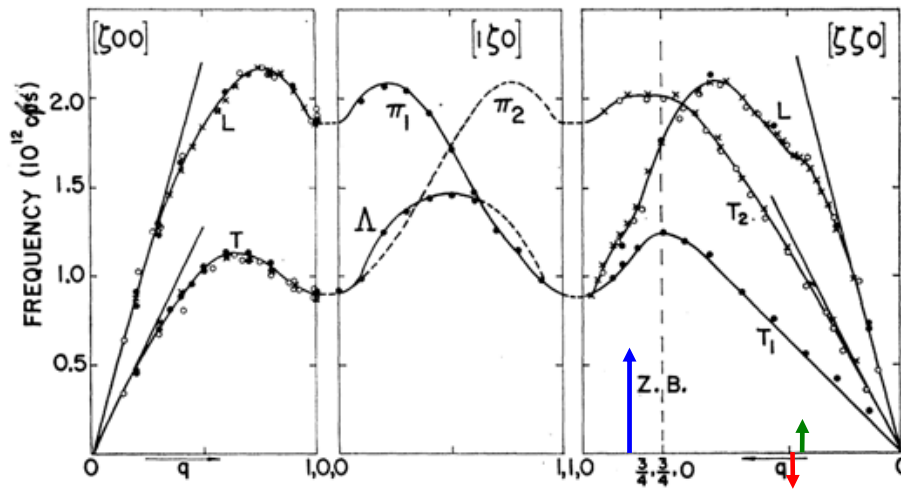
(b)

Figure 1.2.: *The origin of Kohn anomalies in the phonon dispersion. (a) Central* [110] *section of the Fermi surface in Pb in the extended-zone scheme (left) and the folded-zone scheme (right) compared with an empty-lattice model (circle and arcs). Possible nesting wavevectors ∥* [1̄10] *are indicated by arrows. Adapted from Ref. 11. (b) Effect on the phonon dispersion, measured by neutron spectroscopy: the vector lengths in panel (a) determine the lateral positions of the arrows with the same color. Upward and downward kinks (distinguished by the sign of the respective arrow) are seen in the longitudinal branch at these wavevectors. The lengths of the arrows in this panel roughly reflect the relative strength of the Kohn anomalies as was calculated in 1963* [12]. *Image from Brockhouse et al., Ref. 13.*
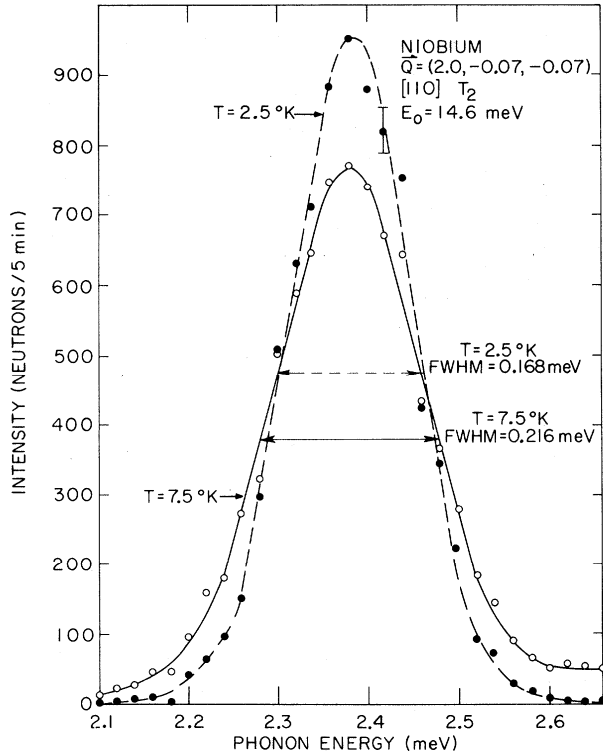
Figure 1.3.: *In 1975, Shapiro, Shirane and Axe reported changes in the spectral phonon linewidth in Nb measured by neutron spectroscopy as the sample becomes superconducting, shown here for the phonon at $[\zeta\zeta 0]\,T2$, $\zeta = 0.07\,r.l.u.$. E_0 is the incident neutron energy. From Ref. [14].*

energy of the phonon is not large enough to excite electrons across the gap. This means that the full width at half maximum (FWHM) of the gaussian peak at $T = 2.5\,\mathrm{K}$ is mostly caused by the instrumental broadening. The difference in the width between the two temperatures of $48\,\mu\mathrm{eV}$ is small by comparison. For other elemental superconductors like Pb, the attempt to resolve changes in the phonon linewidth using triple-axis spectroscopy failed.

The resolution in neutron spectroscopy was improved by several orders of magnitude by the combination of the spin-echo and the triple-axis spectroscopy (TAS) techniques [16, 17]. The instrument TRISP at the neutron source FRM II in Garching is the first dedicated spectrometer of this type that is able to resolve intrinsic phonon linewidths over broad energy and momentum regions. Stimulated by the early TAS experiments on Nb by Axe and Shirane, phonon linewidths in the elemental superconductors Pb and Nb were remeasured with high resolution. The temperature dependence of low-energy acoustic phonons in Pb was resolved for the first time and proved to follow the expected behavior [18]. The momentum dependence of the linewidth showed a peak located at the phonon energy corresponding to the width of the superconducting gap at zero temperature, $2\Delta_0$. This peak persisted up to high temperatures and was assigned to a Kohn anomaly. Figure 1.4

shows the published data, demonstrating the coincidence between the energy of a Kohn anomaly along the lowest acoustic phonon branch and the saturated energy gap $2\Delta_0$. The surprising fact is that such a coincidence was also visible in niobium [19, 20]. This lead to the hypothesis that there might be an as yet unidentified mechanism that links $2\Delta_0$ to the lowest energy Kohn anomaly [21].

$2\Delta_0$ is at first sight unrelated to a Kohn anomaly. The effect of the anomaly on the integrated value of $\alpha^2 F(\omega)$ is minor. The anomaly is a normal state property that the gap magnitude should have no bearing on. The way in which these phenomena – one determined by the Fermi surface topology, the other by the energy scale of the phonon band structure - come together is illustrated in Fig. 1.5. Panels (a) and (b) show the electron excitation by an acoustic phonon with $q = 2k_F$ in a 1-dimensional nearly free electron bandstructure in the normal and superconducting state, respectively. The angle with respect to the energy axis is in first approximation given by the slope c_T of the transverse acoustic phonon for $\omega \to 0$, i.e. $\omega_{\mathbf{q}} = c_T q$. Panels (c) and (d) show the same for two dimensions. Panel (e) shows calculated phonon linewidths for a 3-dimensional, perfectly cylindrical Fermi surface at various values of the superconducting gap [22] and bears a striking similarity to the experimental data shown in Fig. 1.4.

Figure 1.6 illustrates the situation in Nb and Pb. The respective lowest transverse acoustic phonon dispersions in the (q_x,q_y,0)-plane are modeled using neutron data. The average reported saturated gap values, $2\Delta(\text{Pb}) = 2.8\,\text{meV}$ and $2\Delta(\text{Nb}) = 3.1\,\text{meV}$, are shown together with the positions of the newly discovered Kohn anomalies along the [100] and [110] directions [20, 23]. The magnitude of the momentum-dependent saturated energy gap as determined from the phonon linewidth data departs from the average, seemingly to follow the phonon energy at the Kohn anomalies. This could explain the anisotropy of the energy gap observed in tunneling data.

The aim of this thesis is to further investigate the coincidence between the Kohn anomaly and the width of the energy gap. The strategy pursued is to study alloys of Pb with Bi or Tl. Adding up to 20% Bi to Pb increases the transition temperature T_c and the magnitude of $2\Delta_0$, whereas alloying Tl reduces these two quantities. It could be verified by neutron spectroscopy that the energy of the Kohn anomaly also shifts and stays linked to $2\Delta_0$ within experimental uncertainty.

The second main aim of this thesis is to study spectral lineshape anomalies at phonon energies close to $2\Delta_0$ and temperatures around T_c. Normally, the damping of phonons is exponential, leading to Lorentzian lineshapes. As explained in more detail in chapter 3, dramatically asymmetric phonon lineshapes were first observed in the borocarbide super-conductor YNi$_2^{11}$B$_2$C in 1996 [24]. The asymmetries were explained by Allen [25] as shifts of spectral weight across $2\Delta_0$ consistent with the BCS theory. Though these lineshape anomalies were thought not to be observable in elemental superconductors such as Pb and Nb, Weber reported such asymmetries in Nb using conventional TAS with comparatively low resolution but sophisticated data analysis [26]. At TRISP, such asymmetries were first
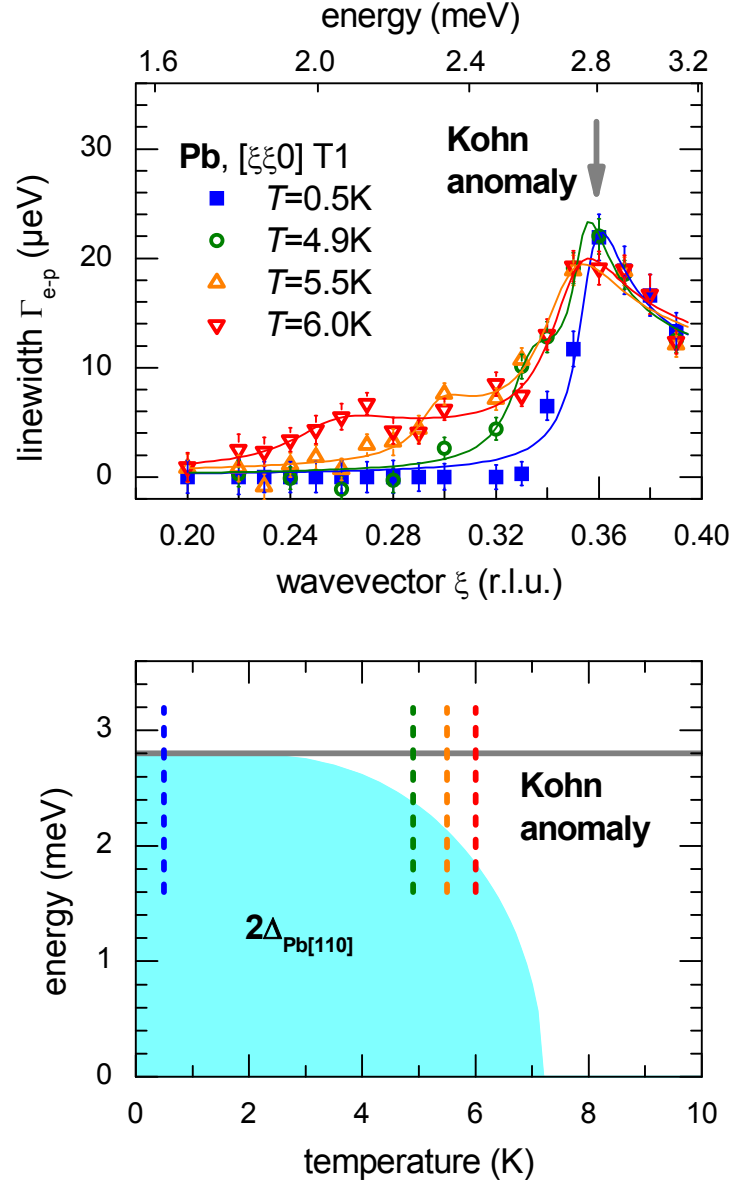
Figure 1.4.: *Coincidence of the saturated energy gap and a Kohn anomaly in Pb in the* $[110]$ *T1 phonon branch. Top panel: intrinsic phonon linewidths* $\Gamma_{e-p}(\mathbf{q})$ *measured on* TRISP *at various temperatures below* T_c. *Corresponding phonon energies are shown on the top axis. At* $\mathbf{q}_{KA} = [0.36, 0.36, 0]$, $\omega_{KA} = 2.8\,meV$, *the linewidth is broadened due to a Kohn anomaly. The linewidths reduce to zero for phonon energies below the gap* $2\Delta(T)$. *Bottom panel: dashed lines show the values of the energy and temperature at which the linewidth data from the top panel are recorded.* $2\Delta(T)$ *(blue area) and* ω_{KA} *(gray line) are both reflected in the linewidths. Freely adapted from Ref. 19.*

not observed despite the much better energy resolution. In a second, optimized experiment on TRISP, we could verify that such lineshape asymmetries in Nb are not observable as the linewidths are smeared out by the finite momentum resolution. The relation between linewidth and energy renormalization both in Nb and Pb are also analyzed in detail. The relative changes of the linewidth and the energy proved to be Kramers-Kronig consistent and follow the predictions by Allen based on BCS. The absolute values show significant deviations from the predictions based on *ab initio* calculations for the normal state and for Allen's predictions for the superconducting state. The reason for these discrepancies is not yet understood. Lattice defects and impurities might play an important role, as they possibly affect the electronic states, the interatomic forces and the electron-phonon coupling.

In a broader sense, this thesis ranks among the many ongoing endeavors in learning about electronic signatures on phonons, and the interplay of such effects with respect to superconductivity (see e.g. Ref. 27, 28 and references therein). The small effects of the superconducting state on the phonon spectrum, accessible by the neutron instrument TRISP, could enhance the understanding of conventional superconductors. As the phonon resonance is not quite unlike the formation of a spin-resonance mode in the unconventional cuprate and ferropnictide superconductors [29, 30], it could provide a basic reference for these yet to be explained materials.
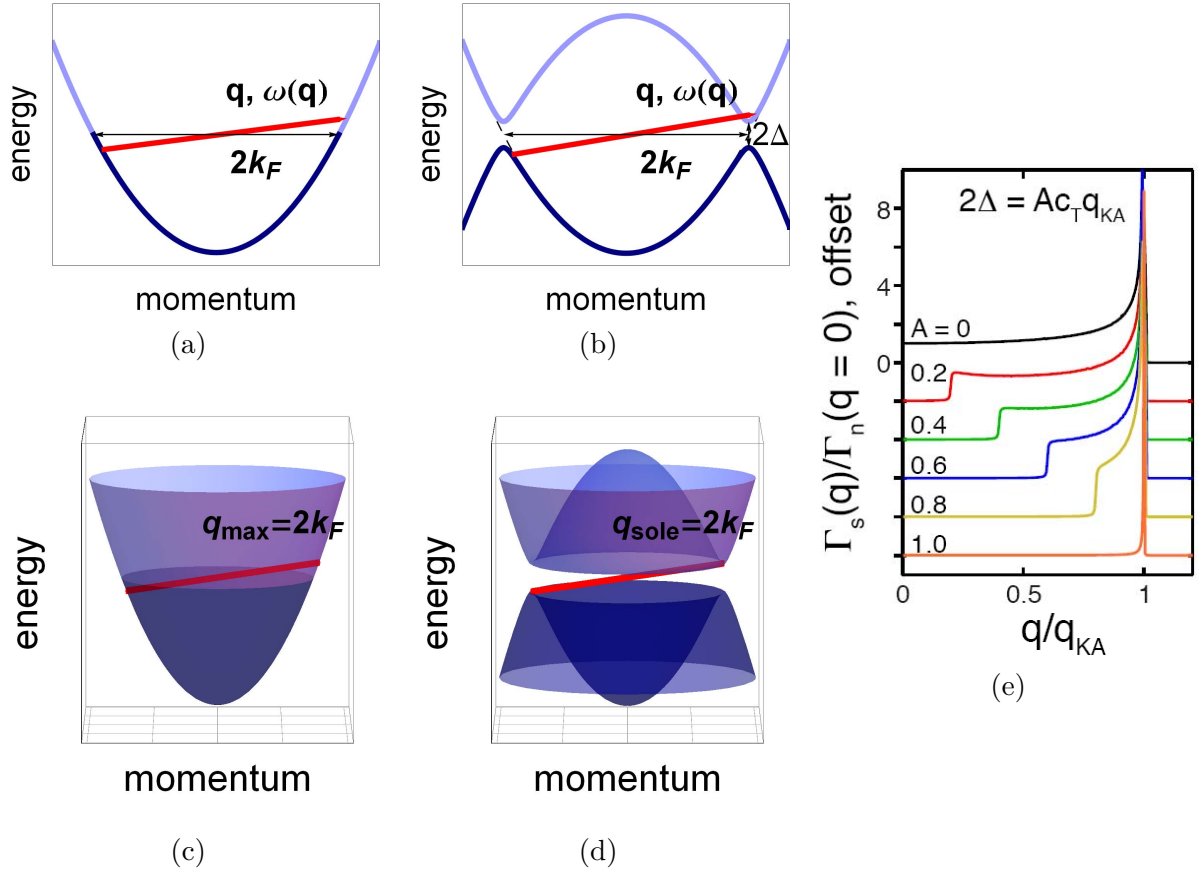
Figure 1.5.: *(a) Electron excitation through absorption of an acoustic phonon with $q = 2k_F$ (red line) in a nearly free electron model bandstructure (not true-to-scale). The angle with respect to the energy axis is in first approximation given by the slope c_T of the transverse acoustic phonon for $\omega \to 0$, i.e. $\omega_{\mathbf{q}} = c_T q$. In two dimensions (panel c) transitions with wavevectors $q < 2k_F$ are possible, too. (b) In the SC state, excitations are only possible if the gap is such that $\hbar\omega(\mathbf{2k_F}) \geq 2\Delta$. (d) In 2 dimensions, for $\hbar\omega(\mathbf{2k_F}) \equiv 2\Delta$, only the extremal transition is possible. (e) Calculations from Ref. 22 for a cylindrical Fermi surface, showing the normalized transverse acoustic phonon linewidth in the SC state at $T = 0\,K$ for various values of the superconducting gap $2\Delta = Ac_T q_{\mathrm{KA}}$. Curves $A = 0$ and $A = 1$ reflect the situations in panel (c) and (d), respectively.*
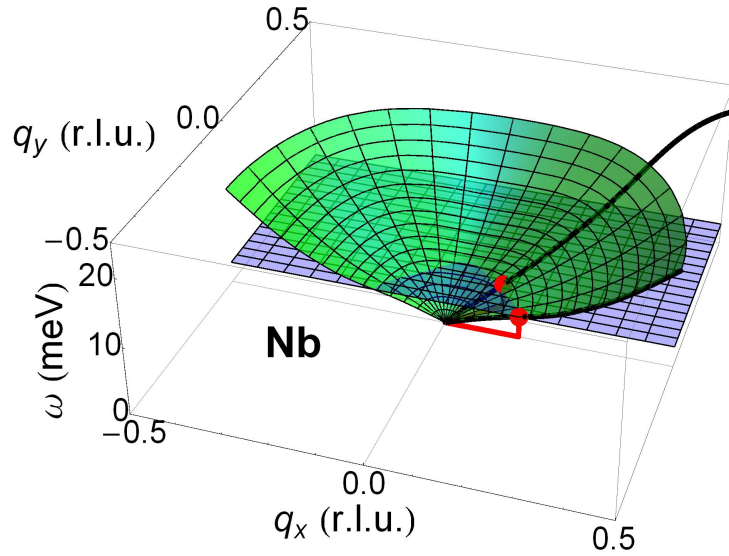
(a)
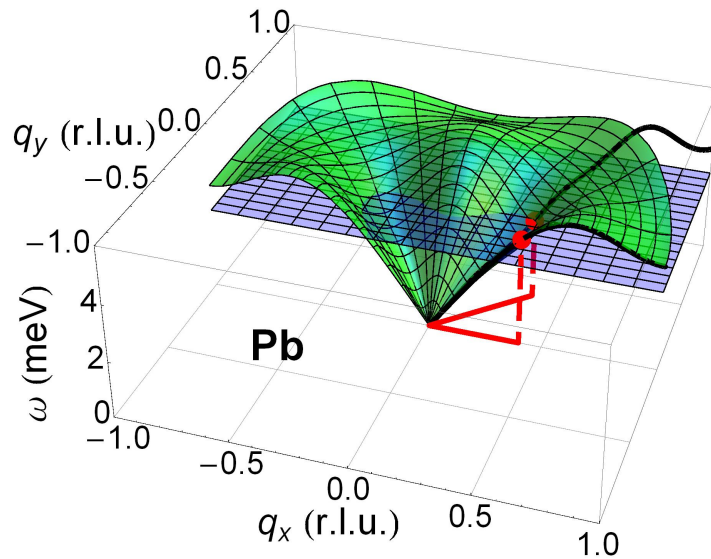
(b)

Figure 1.6.: *3D illustration of the coincidence of the saturated energy gap and Kohn anomalies in Nb (top) and Pb (bottom), as first reported in Ref. 20. The green surface is the lowest transverse acoustic phonon dispersion in the $(q_x, q_y, 0)$-plane, modeled using high symmetry neutron data and sporadic off-symmetry data. The blue flat surfaces depict the average reported saturated gap values, $2\Delta(\text{Pb}) = 2.8\,meV$ and $2\Delta(\text{Nb}) = 3.1\,meV$, resp. Kohn anomalies along the [100] and [110] directions are shown in red. The anisotropy of the energy gap (not shown) follows the energy at the Kohn anomalies.*

2. Neutron resonance spin-echo spectroscopy

Neutron scattering is a powerful method for probing condensed matter. Since neutrons are unstable outside the atomic nucleus and do not have an electric charge, intense beams of free neutrons can only be produced by nuclear fission within a research reactor or by the impact of GeV protons on a target in a spallation source. The initially fast neutrons are slowed down by collisions with atoms of similar mass, such as hydrogen or deuterium contained in (heavy) water, until they are in equilibrium with the surrounding medium and their velocity distribution approximately assumes the corresponding Maxwell-Boltzmann statistics. So-called thermal neutrons with a most probable velocity of $2200\,\mathrm{ms}^{-1}$ are acquired when the moderator has room temperature. This thermal velocity corresponds to a neutron energy of $25\,\mathrm{meV}$. Bearing in mind the wave-particle duality, the most probable De Broglie wavelength is $1.8\,\text{Å}$. Since this wavelength is in the range of the interatomic distance in solids and liquids, interference effects occur and thus thermal neutrons are ideal for studying coherent effects. Moreover, their energy is of the same order as those of typical excitations in condensed matter. This makes them ideal for studying coherent dynamics.

After the discovery of free neutrons by James Chadwick in 1932, the first nuclear reactor ("Chicago Pile-1") was built under the direction of Enrico Fermi in 1942. Fast-forward to 1956 and Bertram Brockhouse developed the first triple-axis spectrometer (TAS), an instrument that allows for a precisely controlled measurement of the energy and momentum transfer of neutrons to a sample. He therewith opened up a main topic of condensed-matter research, namely the study of the energy and lifetime of lattice vibrations (phonons) as a function of their propagation speed and direction. For this accomplishment he later received the Nobel prize together with Clifford Shull in 1994.

The spectral linewidth of a phonon is inversely proportional to its lifetime. Since phonons are generally long-lived, their linewidths can be as small as a couple of micro-electron-volt or less. To reach this resolution on a conventional triple-axis spectrometer, the energy of the ingoing and exiting neutrons would have to be determined this precisely. However, apart from technical difficulties to narrow down the monochromaticity of the neutron beam, the related loss in beam intensity is so large that measurements are impossible.

This intensity problem is avoided by exploiting the precession of the neutron spin in a magnetic field. Each individual flight path can thus be marked by a Larmor precession angle. If neutrons with different velocities undergo the same trajectory and scattering process, their final spin precession phase should be equal. If the energy transfer during the scattering process is not exactly the same for each neutron because of the linewidth of the excitation in question, the final spin phases are spread out. This neutron spin-echo (NSE) method was invented and developed by Ferenc Mezei [31]. The fan-out of the Larmor precession phases depends on the scattering process rather than the neutron velocity. This means that the energy transfer accuracy is disentangled from the neutron beam monochromaticity. To achieve the echo, the magnetic field after the scattering event and therefore the Larmor precession are reversed with respect to the field before the sample. The limit on the accuracy is set by the sharpness of the boundaries of the magnetic fields and their homogeneity.

Acoustic phonons, or in general dispersive excitations, impose an additional challenge. Even if their linewidth is infinitely small, the neutrons scattered from different parts of the phonon branch transmit different energies and thus there is no perfect "echo". An ingenious focusing technique suggested by Mezei [32, 31] and worked out by Roger Pynn [33] offers a solution: by tilting the magnetic field boundaries with respect to the main neutron direction, the spin precession for all scattered neutrons becomes equal. With this degree of freedom, the spin-echo can be tuned to the slope of the dispersion curve, as explained in more detail in paragraph 2.3.

Golub and Gähler made this acoustic phonon focusing method technically feasible in 1987 [16] by proposing that the solenoids to create a static magnetic field be replaced with a sequence of high frequency spin π-flipper coils, separated by a zero-field region. In this setup, there is no classic spin precession, but the interaction with the oscillating magnetic resonance fields gives the spins a phase angle that is proportional to their flight time in the zero-field region. This so-called neutron resonance spin-echo (NRSE) technique reduces field inhomogeneity and stray fields at the coil boundaries, which shifts the limit on the field boundary tilt angles up to approximately 50°.

The NRSE setup may be used for Larmor diffraction as well [34]. This is an elastic scattering technique that can be used on single crystals and powder in order to determine the mosaicity or the spread in lattice spacings. Since these data are important to know for the analysis of phonon linewidths, it is useful to carry out Larmor diffraction to characterize the samples.

Around the turn of the millennium the first NRSE data were produced. By now, the neutron resonance spin-echo method is well-established. Since 2004, the instrument TRISP at the neutron source Heinz Maier-Leibnitz (FRM II) offers NRSE on a triple-axis spectrometer at a thermal beam line. Its energy resolution is in the μeV range - typically two orders of magnitude better than for TAS alone.

In this chapter, after a short description of the triple-axis and NRSE spectroscopic technique, the use for Larmor diffraction is briefly explained and the actual instrument setup of TRISP is specified.

2.1. Neutron scattering in condensed matter

The zero electrical charge of the neutron means that there is no Coulomb barrier to be overcome when entering condensed matter: the bulk of the material is probed and not the surface. The scattering and absorption cross sections are purely dependent on the isotopes within the material. There are no systematic variations across the periodic table as there are for X-ray scattering - many heavy elements are quite neutron transparent. Isotopes with a large capture cross section for thermal neutrons, such as ^{10}B or ^{113}Cd, are commonly used for shielding.

Since nuclear scattering can be treated as a very weak perturbation, the nature of the states in a condensed matter system is not modified. As the momentum and energies of thermal neutrons are low, the scattering at the nucleus is isotropic (s-wave) and can be expressed using a single parameter, the scattering length b. In most cases, it can be assumed constant in the thermal energy range. The corresponding scattering cross section is $\sigma = 4\pi b^2$ and is traditionally measured in barn (1 barn= $100\,\mathrm{fm}^2$). To calculate the total scattering cross section from a sample, one can take the average over the scattering lengths of the individual atoms.

Neutrons have a magnetic dipole moment despite their zero net electrical charge due to the neutron's composition of one *up* and two *down* quarks. For interaction with nuclei with a nuclear spin, the scattering length may vary depending on whether the neutron and nuclear spins are parallel or antiparallel. The magnetic moment also gives rise to interaction with the unpaired electron spins in the atomic shell, with a strength comparable to the nuclear interaction. To select a spin polarization in a white or monochromatic neutron beam, supermirrors are used that contain layers of a ferromagnetic material (e.g. iron-cobalt). In triple-axis spectrometers, Heusler alloy crystals are widely used as spin-polarizing monochromators and analyzers. These are ferromagnetic metal alloys with a face-centered cubic crystal structure, whose constituents themselves are not ferromagnetic.

Due to interference effects, neutrons scatter not only from individual nuclei, but also from cooperative effects among periodically structured nuclei. The differential nuclear scattering cross section can thus be divided into a coherent and incoherent part, σ_{coh} and σ_{inc} (see e.g. Ref. [35, 36]). Elastic Bragg scattering and inelastic scattering by creation or absorption of one or more phonons or spin waves (magnons) in magnetic materials are coherent effects. Incoherent scattering on the other hand may provide information about individual particle motion (e.g. diffusion) or may otherwise violate the interference

condition. Incoherent one-phonon scattering in a cubic crystal for instance produces a signal that is directly proportional to the phonon density of states; though energy is conserved, the dependence on the reciprocal lattice vectors is lost. There are no systematic variations across the periodic table when it comes to the relative strengths of coherent and incoherent scattering. Prominent examples of materials for which the incoherent scattering is large are hydrogen and natural vanadium. As this creates an unwanted background in phonon measurements, materials containing hydrogen, e.g. many glues, are to be used sparsely in the sample environment and preparation. Apart from incoherent scattering that is isotope-specific, a randomly distributed mixture of isotopes gives rise to additional incoherent scattering.

2.2. Triple-axis spectrometry (TAS)

Inelastic scattering experiments can be carried out on a triple-axis spectrometer. It operates by defining the direction and magnitude of the neutron wavevectors $\mathbf{k_{i,f}}$ before and after the sample, respectively. $|\mathbf{k}| = 2\pi/\lambda$ is proportional to the square root of the neutron energy, $k = \sqrt{2m_n E/\hbar^2}$, with m_n the neutron mass and $\hbar$ Planck's constant and λ the wavelength. The incident neutron energy E_i is selected by Bragg diffraction at the monochromator crystal, as shown in Fig. 2.1. The nth order reflection from crystal lattice planes with spacing d is given by

$$\frac{n\pi}{k} = d\sin\theta \qquad \textit{Bragg's law} \qquad (2.1)$$

with θ the angle between the planes and the beam. The neutron energy can thus be altered continuously by a "$\theta/2\theta$" movement.

A coarse spectral selection needs to be performed in order to suppress higher harmonics, $n > 1$. This can be achieved by placing a filter material in the beam that has a sharp energy-dependent attenuation or absorption edge, or by using a velocity selector, which consists of a rotor with neutron-absorbing blades. The smaller the mosaicity of the monochromating crystal, the more defined the neutron energy is, but also the more the beam intensity suffers.

Soller collimators, consisting of parallel absorbing plates, may be used to restrict the divergence of the neutron paths. This further restricts the distribution of incident neutron wavevectors $\mathbf{k}_i$ around the most probable vector $\mathbf{k}_I$. Next, the neutrons are scattered by the sample over an angle $2\theta_S$. This determines the direction of $\mathbf{k}_F$, but not yet the magnitude. Since the neutron energy cannot be resolved by the detector, the monochromation process needs to be repeated at the analyzer in order to select the final neutron energy E_F. Now the difference between the neutron wavevectors before and after the sample is well-defined, giving the total transferred momentum vector $\mathbf{Q} = \mathbf{k}_I - \mathbf{k}_F$ and the energy transfer $\hbar\omega = E_I - E_F$. These three vectors form the scattering triangle. The sample orientation
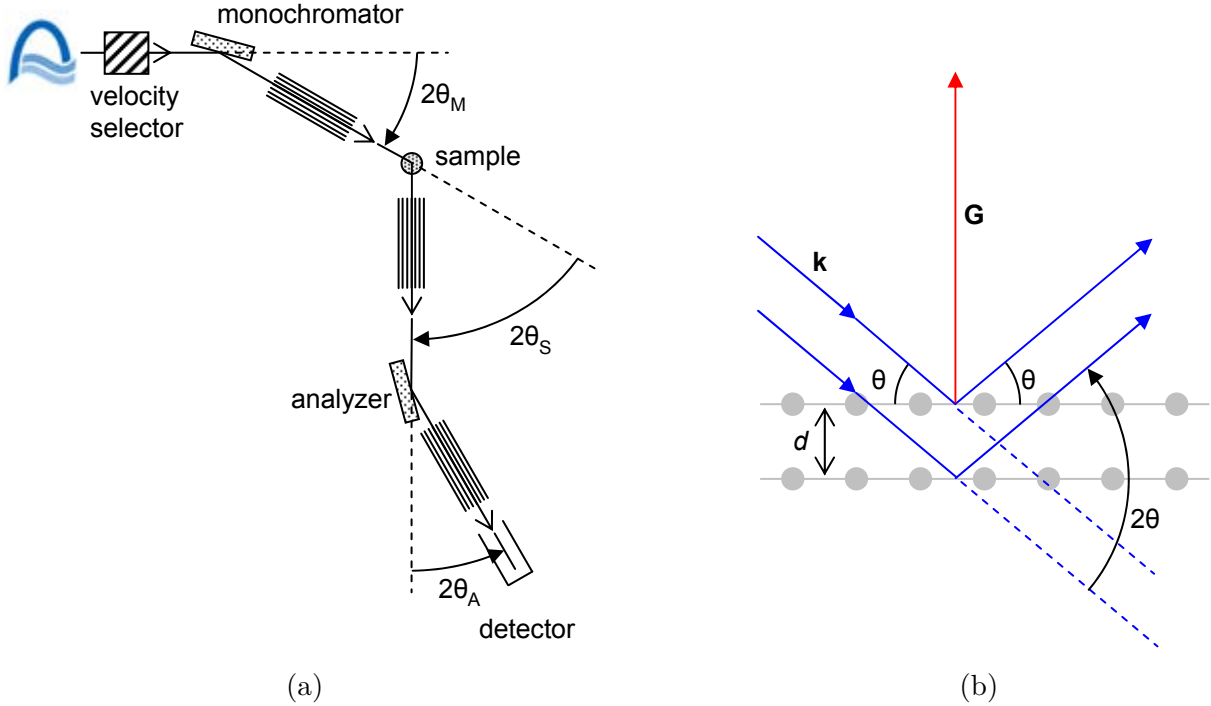
<div align="center">(a)   (b)</div>

Figure 2.1.: *(a) Schematic layout of a triple-axis spectrometer. Soller collimators in between the units restrict the neutron beam divergence. In the shown arrangement, the scattering angles are negative at the monochromator and sample and positive at the analyzer (right-handed configuration). (b) Bragg scattering from a crystal lattice, as utilized repeatedly in the triple-axis spectrometer. $\mathbf{G}$ is the reciprocal lattice vector normal to the planes with magnitude $2\pi/d$.*

with respect to this triangle is specified by the sample angle. It is the custom to label the monochromator incident angle, monochromator scattering angle, sample incident and scattering angle, analyzer incident and scattering angle in due order A1…A6.

Last, the scattered neutrons may be detected in a ^{3}He proportional counter through the nuclear reaction

$$\mathrm{n} + {}^3\mathrm{He} \quad \rightarrow \quad {}^3\mathrm{H} + {}^1\mathrm{H} + 764\,\mathrm{keV}. \tag{2.2}$$

If the sample is a single crystal from which a Bragg reflection is measured, then $\mathbf{Q}$ equals the reciprocal lattice vector $\mathbf{G}$. The momentum of phonons depends only on the relative wavevector $\mathbf{q} = \mathbf{Q} - \mathbf{G}$ within a Brillouin zone, referencing to the nearest reciprocal lattice point. One common way to measure a phonon energy is to work at a fixed wavevector $\mathbf{q}$, while varying the energy of the incoming neutrons. Convention dictates that the energy $\hbar\omega = E_I - E_F$ refers to the excitation in question, i.e. its sign is positive when the neutron loses energy. The wavevector $\mathbf{Q}$ is traditionally defined as $\mathbf{k}_I - \mathbf{k}_F$. Since generally positive and negative $\mathbf{Q}$'s are symmetrically equivalent, the sign can be neglected. We will carelessly
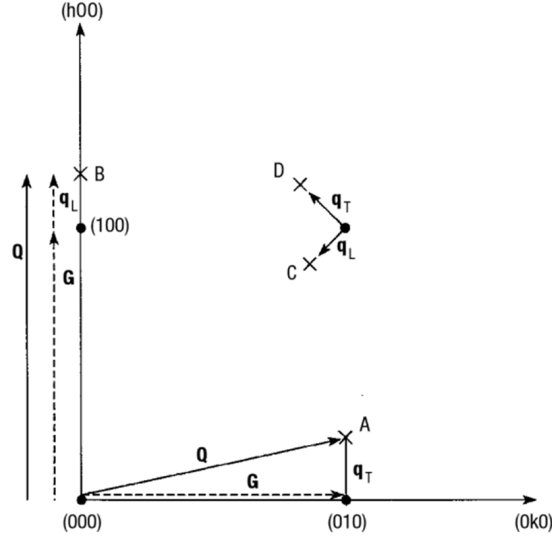
Figure 2.2.: *Selection of transverse or longitudinal modes on a* TAS. *An (001)-plane of a crystal in reciprocal space is shown. Vectors* **G** *denote crystal reciprocal-lattice vectors,* **Q** *the total momentum transferred by the neutron and* **q** *the phonon momentum. Purely transverse acoustic modes can be measured at points A and D, while purely longitudinal acoustic modes are obtained at B and C. Figure from Ref. [36].*

proceed to use the symbol ω for the energy instead of the frequency so that we may omit $\hbar$. Hence, the energy and momentum conservation read

$$\omega = E_I - E_F$$
$$\mathbf{Q} = \mathbf{k}_I - \mathbf{k}_F = \mathbf{G} + \mathbf{q}.$$

energy and momentum conservation (2.3)

The phonon intensity depends on the Bragg intensity at the nearest reciprocal lattice vector. The selection rules for the respective crystal structure hold the key as to which reflections are allowed. Fig. 2.2 shows how transverse versus longitudinal phonon modes are selected in different Brillouin zones. A longitudinal phonon mode involves atomic displacements parallel to the direction of propagation. In other words, the polarization $\hat{\epsilon}$ is parallel to **q**. Since the coherent one-phonon scattering cross section contains a factor $\mathbf{Q} \cdot \hat{\epsilon}$ (see e.g. Ref. [36] for the complete scattering formulae), a scan where the phonon momentum **q** and the total transfer **Q** are parallel is sensitive to a longitudinal acoustic mode. A scan where **q** is perpendicular to the reciprocal lattice vector **G** and small in comparison, so that **q** is approximately perpendicular to **Q**, would completely suppress any longitudinal acoustic mode, so that transverse modes are measured only.

As discussed previously, the monochromator and collimators select a bundle of neutrons with wavevectors $\mathbf{k}_i$ around the most probable wavevector $\mathbf{k}_I$. The probability to detect a scattered neutron with wavevector $\mathbf{k}_f$ is determined by the distribution around $\mathbf{k}_F$. Consequently the energy and momentum transfers of the neutrons are distributed about the average values $(\mathbf{Q}_0, \omega_0)$. The effective instrumental resolution R can be mapped

using Bragg peaks as δ-peak signals in this four-dimensional space. Though individual instrument components may have triangular or trapezoidal transmission functions, R is reasonably well-described by a $4D$ gaussian distribution

$$R = R_0 \exp\left(-\frac{1}{2}\mathbf{X}^T\mathbf{M}\mathbf{X}\right) \qquad \textit{triple-axis resolution function} \qquad (2.4)$$

with R_0 a constant and introducing the four-component vector $\mathbf{X} = (\mathbf{Q} - \mathbf{Q_0}, \omega - \omega_0)$. The wavevector coordinate system is given by $\Delta Q_\parallel$ parallel to $\mathbf{Q_0}$, $\Delta Q_\perp$ perpendicular to $\mathbf{Q_0}$ within the scattering plane and the out-of-plane component ΔQ_z. In general, the triple-axis resolution matrix $\mathbf{M}$ is not diagonal with respect to these principal axes. This means that the resolution ellipsoid, which describes the 50%-probability contour of R, is oblong and canted. Fig. 2.3 shows an example of a resolution ellipsoid for $\omega_0 = 0$ and $k \approx 2.664\,\text{Å}^{-1}$, which is obviously canted in the transverse direction $\Delta Q_\perp$. If the slope of the "Bragg tail" (the wing of the ellipsoid through a Bragg peak) is approximately equal to the slope of an acoustic phonon of interest, it will prohibit the accurate measurement of the dispersion at small $\mathbf{q}$. A practical rule of thumb exists for the slope of the long axis of the ellipse along the $Q_\perp$-axis, reading

$$\frac{\Delta\omega}{\Delta Q_\perp} \approx -(4\,\text{meV Å}^2)k \qquad (2.5)$$

for right-handed spectrometers (angle A4 negative). It is valid near elastic conditions, $k_I \approx k_F \equiv k$, whenever the monochromator and analyzer mosaics are more restrictive than the collimation.

Generally, when measuring other than point-like spectral functions, one measures a convolution of the scattering function with the resolution function. Phonon focusing in triple-axis spectrometry means that the inclination of the resolution ellipsoid is in approximate accordance with the inclination of the slope of the phonon dispersion. If this is the case, an energy scan provides an intense narrow peak. If the inclinations are opposed to each other, the peak is broadened. From the sign of Eq. 2.5, it follows that for transverse long-wavelength phonons, if $\mathbf{q}$ points $\sim 90°$ right-hand of $\mathbf{G}$, a created phonon ($\omega > 0$) is focused [36].

If all instrument parameters are known, the resolution matrix can be calculated according to the method by Cooper and Nathans [37] or with the more advanced Popovici method that includes spatial effects [38]. Rescal [39] and Reslib [40] are examples of programs using the numerical computing environment software MATLAB to inspect spectrometer settings and to simulate the resolution using these calculation methods.

2.3. Neutron resonance spin-echo (NRSE) spectroscopy

Using the spin-echo principle, the Fourier transform of a scattering function $S(\omega)$ can be measured by means of the neutron polarization. That way, linewidths can be determined
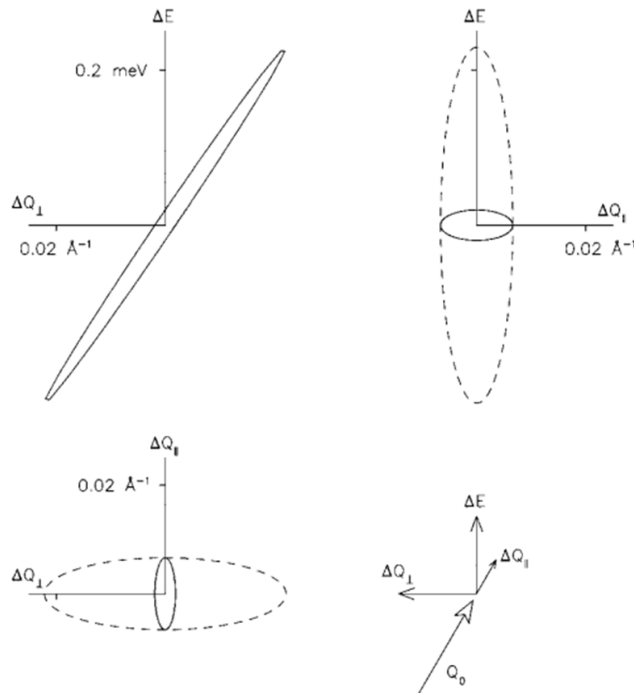
Figure 2.3.: *Example of the cross sections of a resolution ellipsoid with a given plane (solid lines) and projections onto the plane (dashed lines). Calculated using the Cooper-Nathans method for $\omega_0 = 0$, $Q_0 = 1.5\,\mathring{A}^{-1}$, $E_I = 14.7\,meV$, horizontal collimations of $20'$ each and $\mathrm{PG}(002)$ monochromator and analyzer crystals with mosaic widths of $24'$. From Ref. [36].*

with excellent energy resolution. The spin-echo setup must be combined with a triple-axis spectrometer to define the momentum resolution. One important feature is the spin-echo focusing technique for dispersive excitations. Rather than the classic spin-echo method, the more advanced resonance spin-echo method is described here. Instead of extended static magnetic fields, it employs a combination of static and oscillating magnetic fields to induce a spin precession. Though the experiment may be described quantum mechanically as a two-state interference [41], the classical treatment pursued here is complete and more insightful.

A neutron spin state can be described by a linear combination of the orthogonal spin-up and spin-down states in the two-dimensional Hilbert space. Like any two-state quantum system, this can be geometrically represented by a vector on the Bloch sphere, where a vector parallel to the z-axis is chosen to represent *up* while antiparallel represents *down*. The polarization of a neutron beam is the ensemble average over all the neutron spin states with respect to the quantization axis z. The polarization is $P = (N_\uparrow - N_\downarrow)/(N_\uparrow + N_\downarrow)$, where $N_\uparrow$ ($N_\downarrow$) is the number of neutrons with spin up (down).

A single spin state can be selected by a polarizing neutron guide. For example, the instrument TRISP is situated at the end of a $10\,\mathrm{m}$ polarizing supermirror guide at the

beam port SR5 of FRM II. The typical transmission for one spin component in the thermal range of interest is $\sim 70\%$ and the polarization of the transmitted neutrons is $> 95\%$.

Because of the magnetic moment associated with the neutron spin, a torque is exerted on any spin vector that is not aligned (anti)parallel to a magnetic field $\mathbf{B}$, so that it precesses with a fixed angular frequency $\omega_L = \gamma B$ in anticlockwise manner around the field direction. This Larmor frequency ω_L is independent of the inclination θ of the spin vector with respect to $\mathbf{B}$. Thus the precession angle in a given field is only a function of the time of flight and can be used as a kind of stopwatch to trace the velocities of individual neutrons. The gyromagnetic ratio of the neutron is $\gamma \approx 1.832 \cdot 10^8 \, \text{rad} \, \text{T}^{-1}\text{s}^{-1}$.

In a slowly rotating magnetic field (rotation speed $\ll \omega_L$), the spin follows the field direction. This may be used to change the polarization direction from the z-axis to the y-axis, perpendicular to the beam direction x. If now suddenly a static field region $\mathbf{B}_0$ in the z-direction is entered, the neutron spins cannot follow the non-adiabatic change in the field, but retain their original orientation. They then perform a Larmor precession in the scattering plane ($\theta = 90°$), as shown in Fig. 2.4(a). In a coordinate system $x'y'z$ rotating with the Larmor frequency ω_L, the spin vector is static. Consequently, the effective magnetic field in this system is completely annihilated [42]. Suppose a rotating magnetic field $\mathbf{B}_{\text{rf}}$ is added to case (a) that is in resonance with the Larmor frequency,

$$\overrightarrow{\omega}_{\text{rf}} \overset{!}{=} \gamma \mathbf{B}_0. \qquad \textit{resonance condition} \qquad (2.6)$$

In the rotating coordinate system, this would be a static field as shown in Fig. 2.4(b). The spin would then precess around $\mathbf{B}_{\text{rf}}$ as shown. After a time $t_\pi = \pi/\omega_{\text{rf}}$, the spin would be back in the scattering plane. This is the principle of the resonance spin-"π" flippers. Thus the second condition that must be fulfilled is

$$B_{\text{rf}} \overset{!}{=} \frac{\pi \hbar k}{\gamma d m_n} \qquad \textit{π-flip condition} \qquad (2.7)$$

with d the geometrical width of the resonance field. The performance of resonance spin flippers is thus limited by the acuteness of the field boundaries and by the velocity distribution of the neutrons, both of which lead to inaccurate π-flips [43]. The angle within the $x'y'$-plane that is bridged by the spin, $2\theta_{\text{rf}}$, depends solely on the relative angle between the spin and $\mathbf{B}_{\text{rf}}$ when the spin enters the resonance field. In the time that it takes to complete the π-flip, the complete system rotates in addition by $\omega_L t_\pi$. Thus the spin direction is altered by

$$\phi - \phi_0 = 2\theta_{\text{rf}} + \omega_L t_\pi. \qquad (2.8)$$

The full advantage of using static plus resonant fields instead of static fields alone will become evident later on.

Oscillating instead if rotating fields can be used when the alternating field is weak with respect to the constant field. An oscillating field is equivalent to two opposite rotating fields as illustrated in Fig. 2.5(a). Since the neutron spins primarily adhere to the rotation ω_L,
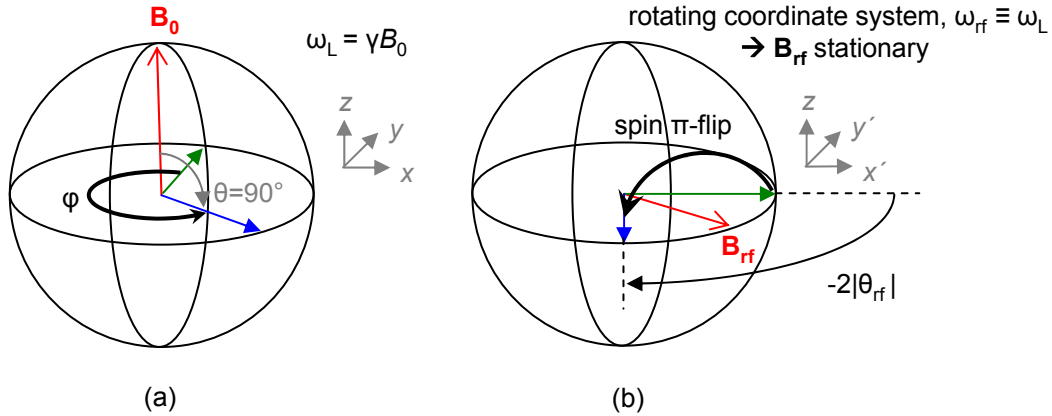
Figure 2.4.: *Larmor spin precession in a magnetic resonance field. (a) Precession of a spin vector in the xy-plane about a constant magnetic field $\mathbf{B}_0$. The angular frequency is ω_L. (b) In a coordinate system rotating with ω_L the spin vector is static, i.e. the effective magnetic field is zero. When a rotating magnetic field $\mathbf{B}_{\rm rf}$ that is in resonance with ω_L is switched on, the spin precesses around $\mathbf{B}_{\rm rf}$ with angular frequency $\omega_{\rm rf}$. If the time that the spin resides in this field is chosen correctly, a "π"-flip is performed, meaning the spin ends up in the xy-plane again.*

the time-averaged counter-rotating field is practically zero and the spins experience only the field component that resonates with the static-field Larmor precession [44]. When neutrons pass through consecutive radiofrequency (rf) coils with opposite but equally large $\mathbf{B}_0$ and equal oscillating fields $2\pi\nu = |\omega_{\rm rf}|$, the respective resonance fields alternate. This is the bootstrap setup shown in Fig. 2.5(b) [43]. The varying arrival times of the spin vectors at the bootstrap coils result in seemingly chaotic spin π-flips and thus an angle de-phasing in the xy-plane. If the field component $\mathbf{B}_{\rm rf}^-$ makes an angle $-\theta_{\rm rf}$ with the y-axis at the time a neutron enters the first coil, the field $\mathbf{B}_{\rm rf}^+$ makes an angle $+\theta_{\rm rf} + \omega_L t_\pi$ at arrival in the second coil. Thus, in case the neutrons are initially polarized in y-direction, their angle with respect to this axis is $4\theta_{\rm rf} + 4\omega_L t_\pi$ at the exit of the bootstrap. The main advantage of an even-numbered bootstrap over a single coil is that opposite static fields significantly reduce stray magnetic fields. Moreover they double the angle $\theta_{\rm rf}$ and therewith the efficiency of the field.

The neutron resonance spin-echo setups with four operating single coils and with four bootstrap coils are shown in Fig. 2.6 and 2.7, respectively. The incident neutrons are polarized perpendicular to the travel direction. During the zero-field travel time between coils A and B before the sample, the spin vector does not change, but the rotating fields do. If the incident neutrons have different velocities, they arrive at B at different times and thus end up with seemingly random spin phases at the sample. At this point, the phase does not depend explicitly on the initial arrival time t_A at point A anymore, but only on the time difference $t_B - t_A = L_1/(\hbar k_i/m_n)$, as can be easily verified [43]. This means that if the static field components and therewith $\omega_{\rm rf} \equiv \gamma\mathbf{B}_0$ in coils C and D after the sample are opposite to those in A and B, the de-phasing is reversed. In the most basic
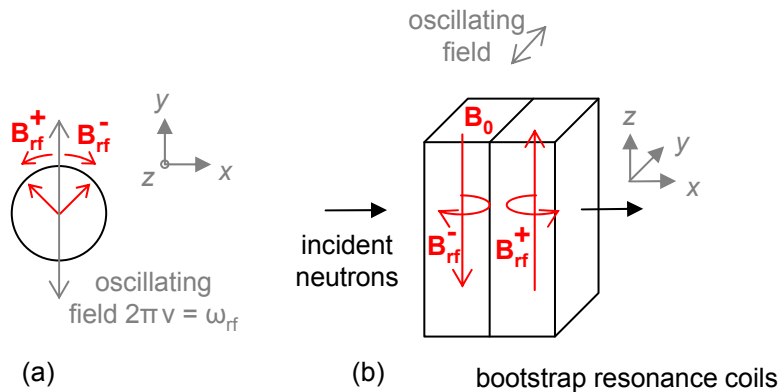
Figure 2.5.: *(a) The decomposition of an alternating magnetic field in counter-rotating fields. Only the rotating field component that complies with the Larmor motion in the additional static field is relevant. (b) Static field directions are alternated in a bootstrap setup with two radiofrequency coils.*

case, where the zero-field regions have equal lengths and the neutron velocities do not change at the sample site, the initial spin vector is resumed, regardless of how the velocities are distributed. The intensity of detected neutrons after crossing another polarizer is then as high as can be. If the velocities *do* change because the neutrons lose an energy ω_0 to the sample, the rf field frequency ν and strength $\mathbf{B}_{rf}$ can be reduced in the second arm to maintain the "echo".
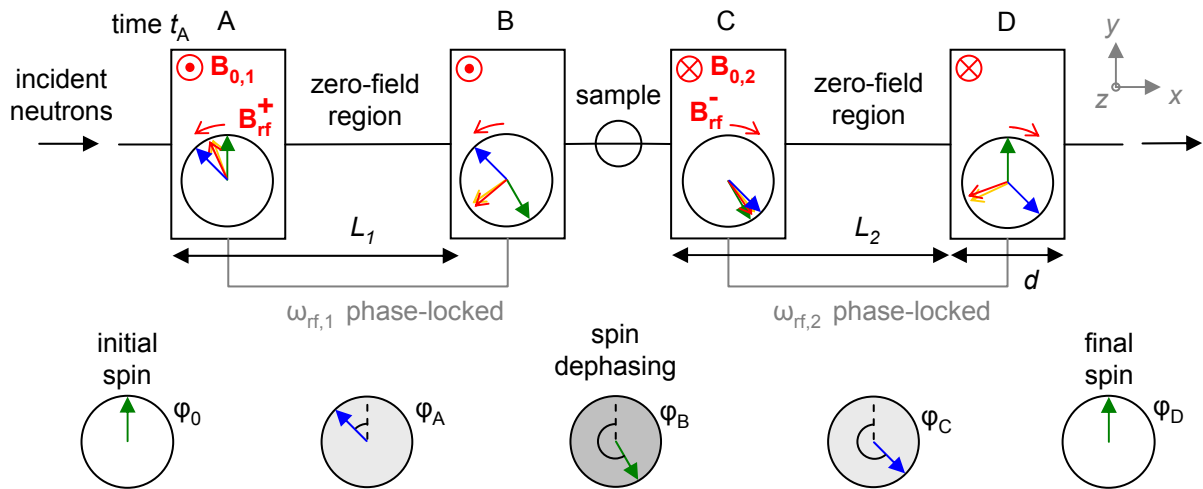
Figure 2.6.: *Neutron resonance spin-echo with four operating "π"-flipper coils (A-D). The motion of a spin vector (polarized perpendicular to the traveling direction) that arrives at an arbitrary time t_A is exemplified. The color of the spin vector at entrance and exit of the coils is alternated between green and blue. The resonance field direction at the entrance (exit) of each coil is orange (red), showing schematically the angle $\omega_L t_\pi$. During the zero-field travel time between the coils, the spin vector does not change, but the rotating fields do. This results in different arrival times at the following coils due to the velocity distribution of the beam, and thus de-focusing of the spin vector angles, as shown schematically by the shading in the bottom graphs. In the case shown, the initial spin vector is resumed in the end so that there is indeed a "spin-echo".*
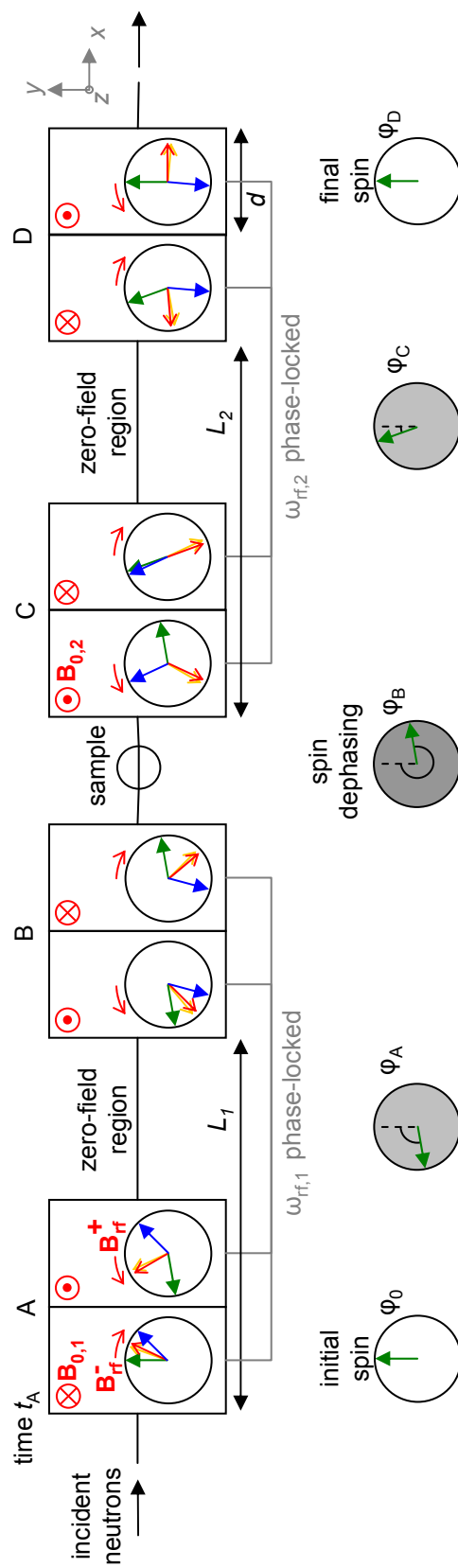
Figure 2.7.: *Same as Fig. 2.6 but for a bootstrap setup with 4×2 "π"-flipper coils.*

The objective of the spin-echo setup is to detect as small spreads in the neutron energy transfer as possible. If the linewidth of an excitation is zero, ideally, there is no spin de-phasing at the end and thus no loss of polarization, no matter how high the de-phasing in between. However, if there is a spread in the energy loss of the neutrons at the sample, the final Larmor phase angles ϕ become less focused with increasing field frequencies and zero-field region lengths in both arms. The measure for the de-phasing power is the spin-echo time τ. By identifying the polarization at several values of the spin-echo time (i.e. several field frequencies), the transferred energy spread can be determined. To detect small linewidths, high spin-echo times are needed. A straightforward calculation shows that an NRSE instrument that uses the static field B_0 in the resonance coils is $2N$ times as effective as a classic spin-echo instrument with B_0 over the entire lengths of L_1 and L_2, N being the number of operating coils at each of the four positions A, B, C and D. Moreover, operating the rf coils is technically easier than maintaining an extended homogeneous magnetic field.

2.3.1. Spin-echo conditions for phonon focusing

The more the energy loss ω of a neutron deviates from the main energy loss ω_0, the larger the spin de-phasing. The main requirement of spin-echo is for the final Larmor phase to be a linear function of the difference $\Delta\omega = \omega - \omega_0$:

$$\phi(\mathbf{k}_i, \mathbf{k}_f) - \phi_0 = -\frac{\tau \cdot \Delta\omega}{\hbar} \qquad (2.9)$$

with the phase at the center $\phi_0 = \phi(\mathbf{k}_I, \mathbf{k}_F)$. This condition can be satisfied to first order in $\Delta\mathbf{k}_{i,f} = \mathbf{k}_{i,f} - \mathbf{k}_{I,F}$ when the velocity distributions of the incident and exiting neutron beam are strongly peaked about their means. This is the case when a triple-axis spectrometer is equipped with the spin-echo device. In the basic setup with straight coil boundaries, the surfaces of constant spin-echo phase in $(\mathbf{q}, \omega)$-space can be assumed to be flat within the triple-axis resolution, as shown in Fig. 2.8(a).

In order to avoid a loss of polarization due to the $\mathbf{q}$-broadening for an excitation with a non-flat dispersion $\omega_0(\mathbf{q})$, like for an acoustic phonon, it is necessary to incline the spin-echo surfaces so that their slope $\mathbf{C}$ in the direction of $\mathbf{q_0}$ matches the slope of the dispersion,

$$\mathbf{C} \overset{!}{=} \nabla_{\mathbf{q}}\, \omega_0(\mathbf{q_0}), \qquad (2.10)$$

as shown in panel (b) of Fig. 2.8. This way, if the dispersion were sharp and linear, ideally, the same Larmor phase ϕ_0 would be retrieved for all scattered neutrons. This phonon focusing can be realized by tilting the boundaries of coils A and B by an angle θ_1 so that their normal vector $\mathbf{n}_I$ changes with respect to the main flight path along $\mathbf{k}_I$, as well as
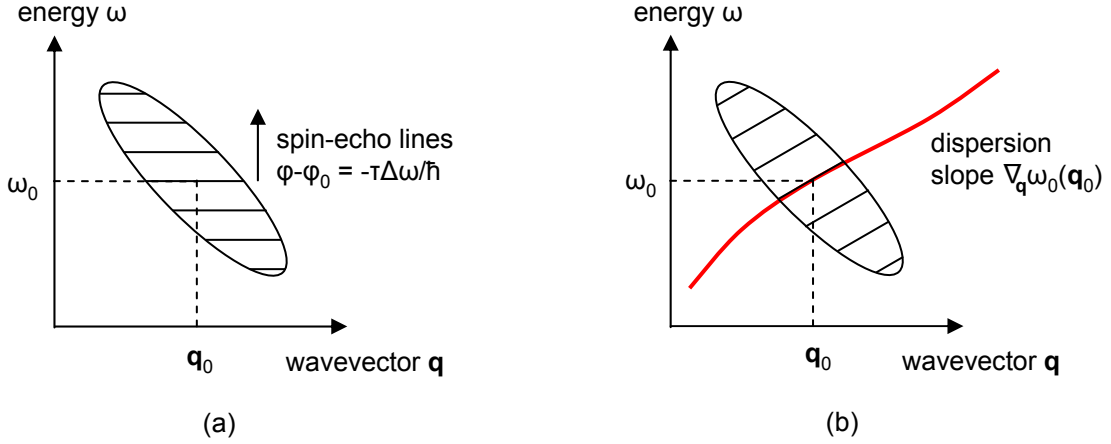
Figure 2.8.: *Focusing of the spin-echo lines onto the dispersion. (a) Schematic drawing of the spin-echo lines on a triple-axis instrument without tilted field boundaries. The TAS resolution ellipsoid outlines the FWHM of the illuminated volume. (b) Spin-echo with tilted field boundaries that are adjusted in such a way that the slope of the surfaces of constant spin-echo phase coincides with the slope of the dispersion at $(\mathbf{q}_0, \omega_0)$. A defocusing configuration of the TAS ellipsoid with respect to the dispersion is chosen to optimize the $\mathbf{q}$-resolution of the phonon linewidths.*

tilting coils C and D by θ_2 so that their normal vector $\mathbf{n}_F$ is altered (see Fig. 2.9(a)). The final Larmor phase is then

$$\phi(\mathbf{k}_i, \, \mathbf{k}_f) = 4\pi N \frac{m_n}{\hbar} \left(\frac{\nu_1 L_1 \cos\theta_1}{\mathbf{k}_i \cdot \mathbf{n}_I} - \frac{\nu_2 L_2 \cos\theta_2}{\mathbf{k}_f \cdot \mathbf{n}_F} \right). \tag{2.11}$$

If $\mathbf{k}_{i,f} \parallel \mathbf{k}_{I,F}$, the dependence on the tilt angles of the coils vanishes. When a neutron is transmitted that loses an additional momentum $\Delta\mathbf{q}$ and energy $\nabla_{\mathbf{q}}\omega_0(\mathbf{q}_0) \cdot \Delta\mathbf{q}$ with respect to the main transfer $(\mathbf{q}_0, \omega_0)$, the pair of $\mathbf{k}_i$ and $\mathbf{k}_f$ that meets these conditions are slightly tilted with respect to the main directions $\mathbf{k}_{I,F}$. Thus the requirement is for the lengths of the flight paths through the rhomboid zero-field regions to be in such a manner, that this neutron's net accumulated phase is the same as in the main case.

Using Eq. 2.11, the phase shift $\phi - \phi_0$ can be expanded to first order in $\Delta\mathbf{k}_{i,f} \cdot \mathbf{n}_{I,F}$. Using energy and momentum conservation and again making use of the fact that the neutron velocities are strongly peaked around their means, $\Delta\mathbf{k}_{i,f} \ll \mathbf{k}_{I,F}$, one can reformulate $\Delta\omega$ in terms of $\mathbf{C}$ and $\Delta\mathbf{k}_{i,f}$. As described in detail in Ref. [45], the following constraints for n_I and n_F in the spectrometer arms 1 and 2 thus result from the spin-echo condition, Eq. 2.9:

$$\cos\theta_{1,2} = \frac{\mathbf{k}_{I,F}}{|\mathbf{k}_{I,F}|} \cdot \frac{\mathbf{k}_{I,F} - \frac{m_n}{\hbar^2}\mathbf{C}}{\left|\mathbf{k}_{I,F} - \frac{m_n}{\hbar^2}\mathbf{C}\right|}. \qquad \textit{coil tilt angles} \tag{2.12}$$
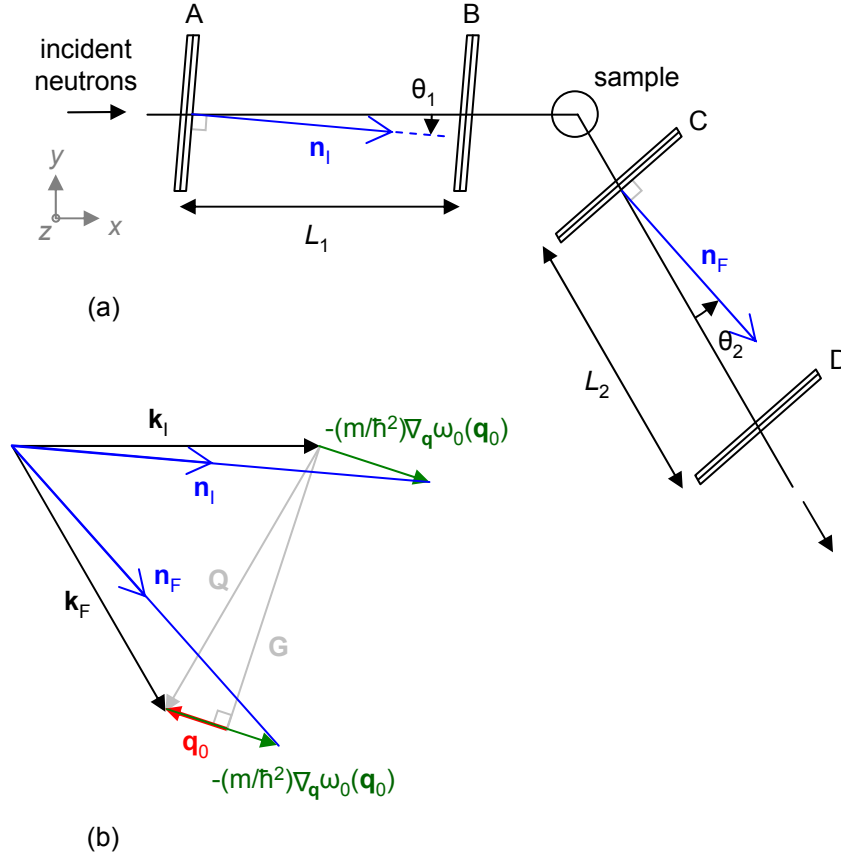
Figure 2.9.: *Inclination of the precession field boundaries for phonon focusing. (a) real space (b) reciprocal space. The normal vectors to the precession field boundaries point in the direction of $\mathbf{k}_{I,F} - (m/\hbar)\nabla_{\mathbf{q}}\omega_0(\mathbf{q}_0)$ as shown in (b) for the case of a transverse phonon $\mathbf{q} \perp \mathbf{G}$.*

Hence the normal vectors of the field boundaries can be geometrically constructed as shown in Fig. 2.9(b). The spin-echo condition for the frequency ratio reads

$$\frac{\nu_1 L_1}{\nu_2 L_2} = \frac{k_I^2}{k_F^2}\frac{\cos\theta_1}{\cos\theta_2}\frac{\left|\mathbf{k}_I - \frac{m_n}{\hbar^2}\mathbf{C}\right|}{\left|\mathbf{k}_F - \frac{m_n}{\hbar^2}\mathbf{C}\right|}. \qquad \text{frequency ratio} \qquad (2.13)$$

If the dispersion is flat, the frequency ratio is equal to the ratio of wavevectors cubed. Take notice that except for elastic scattering, the phase ϕ_0 at the center of the spin-echo group is thus not zero, as a cancelation of the accumulated phase in both arms was not the requirement. The spin-echo time can be equally expressed in terms of either the first or second spectrometer arm:

$$\tau = 4\pi N \left(\frac{m_n}{\hbar}\right)^2 \frac{\nu_{1,2}L_{1,2}}{k_{I,F}^2 \cos\theta_{1,2}\left|\mathbf{k}_{I,F} - \frac{m_n}{\hbar^2}\mathbf{C}\right|}. \qquad (2.14)$$

As mentioned before, the neutron beam polarization is measured at several values of the spin-echo time (i.e. several values of $\nu_{1,2}$) to identify the spectral lineshape of an excitation.

2.3.2. NRSE **for measuring spectral lineshapes**

The polarization measured in the y-direction is the ensemble-average over the Larmor phase

$$\langle \cos\phi \rangle = \frac{1}{2N} \iint S(\mathbf{q},\,\omega)\, T(\mathbf{k_i},\,\mathbf{k_f})\, \exp[i\phi(\mathbf{k_i},\,\mathbf{k_f})]\, \mathrm{d}^3 k_i\, \mathrm{d}^3 k_f + c.c. \qquad (2.15)$$

where $S(\mathbf{q},\,\omega)$ is the coherent scattering law, T the transmission probability and N is a normalization factor. The complex conjugate ensures that the polarization is at all times real.

If the spin-echo condition (Eq. 2.9) is satisfied, the spins are maximally focused, even though the phase ϕ_0 is not necessarily zero. By shifting the last rf coil progressively, the velocity distribution of the neutrons eventually takes its toll and the spin-focusing is lost. Near the center of the spin-echo group, however, this is not noticeable; changing L_2 means changing the traveling time of the neutrons during which the rf field oscillates and thus, after the neutrons cross a polarizer, the intensity that arrives at the detector varies like

$$I(L_2) = \frac{I_0}{2} \left[1 + P \cos\left(4\pi N \frac{m_n}{\hbar} \frac{\nu_2(L_2 - L_{2,0})}{k_F} \right) \right]. \qquad \textit{spin-echo scan} \qquad (2.16)$$

The full beam intensity I_0 is detected when the polarization is 100%. Examples of spin-echo scans made to identify the polarization amplitude P are shown in Fig. 2.10a. The value of I_0 can be obtained from shared fits of the scans for different values of τ. Since a negative polarization cannot be distinguished from a phase shift of π (change of $L_{2,0}$), the absolute value of the polarization is extracted from the fits and plotted against the spin-echo time (Eq. 2.14). This means that only the envelope of Eq. 2.15 is seen. Using Eq. 2.9, the factor $\exp(i\phi_0)$ thus drops out of Eq. 2.15, only a factor $\exp(-i\Delta\omega\tau)$ is left.

Using energy and momentum conservation, the integrals over the incident and scattered neutron energies can be recast into integrations over the respective momentum and energy loss [46]. The transmission function then can be expressed in terms of the triple-axis resolution matrix $\mathbf{M}$ according to Popovici [38]. The polarization as a function of the spin-echo time, extracted from several spin-echo scans, is equal to

$$P(\tau) = \frac{1}{N} \left| \iint S(\mathbf{Q_0} + \Delta\mathbf{Q} - \mathbf{G_0},\, \omega_0(\mathbf{Q_0} + \Delta\mathbf{Q} - \mathbf{G_0}) + \Delta\omega) \right.$$
$$\left. \times F(\Delta\mathbf{Q},\, \Delta\omega)\, \mathrm{d}\Delta\omega\, \mathrm{d}^3\Delta\mathbf{Q} \right| \qquad (2.17)$$

with $\Delta\mathbf{Q} = \mathbf{Q} - \mathbf{Q_0}$, $\mathbf{Q_0} = \mathbf{G_0} + \mathbf{q_0}$ and $\omega = \omega_0(\mathbf{q}) + \Delta\omega$. The NRSE resolution function is

$$F(\Delta\mathbf{Q},\, \Delta\omega) = \exp\left(-i\frac{\Delta\omega\tau}{\hbar} \right) \exp\left(-\frac{1}{2}\mathbf{X}^T\mathbf{M}\mathbf{X} \right). \qquad (2.18)$$

The four-component vector $\mathbf{X} = (\mathbf{Q} - \mathbf{Q}_0,\, \omega - \omega_0)$ was already introduced before in Eq. 2.4. If the $\mathbf{Q}$-resolution is disregarded, it becomes clear that the polarization is the
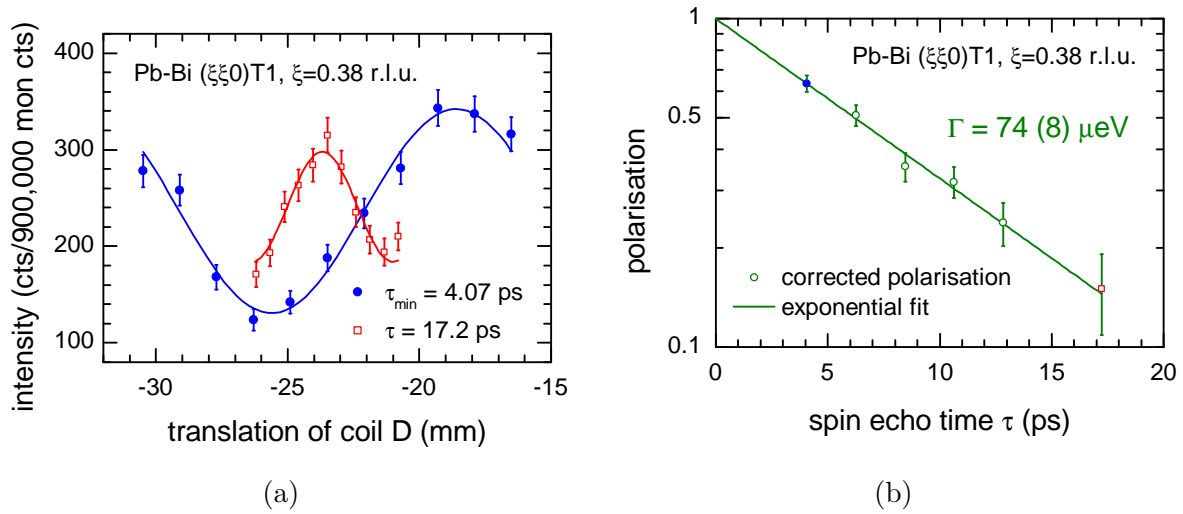
(a)

(b)

Figure 2.10.: *(a) Typical spin echo scans, recorded for the $(0.38, 0.38, 0)\, T1$ phonon in a lead alloy with dilute bismuth concentration. The wave amplitude is largest for the lowest possible value of the spin echo time (blue line), using the minimal frequency $\nu_{\min} = 50\, kHz$. Shown is the number of detected neutrons in a time frame in which $900{,}000$ monitor counts where recorded, which corresponds to half an hour at $k_i = 2.51\, Å^{-1}$. (b) Typical polarization profile for a Lorentzian phonon lineshape. The red and blue points are derived from the respective fits in panel (a). The values are corrected for the direct beam polarization (measured independently), instrumental effects, the mosaic spread in the sample and the dispersion curvature (all calculated using experimental values). An exponential fit gives the phonon linewidth Γ.*

Fourier transform of the spectral lineshape function, or in other words, the intermediate scattering function is measured.

If the scattering function is a simple Lorentzian with linewidth Γ for every energy within the TAS resolution, then

$$S(\mathbf{q}, \omega) = \frac{1}{\pi} \frac{\Gamma}{(\omega - \omega_0(\mathbf{q}))^2 + \Gamma^2}. \tag{2.19}$$

If in addition $\omega_0(\mathbf{q})$ is a linear dispersion with slope equal to $\mathbf{C}$ (Eq. 2.10) and if the linewidth is much smaller than the energy width of the triple-axis resolution function, then the polarization reduces to an exponential function

$$P(\tau) = P_0 \exp\left(-\frac{\Gamma \tau}{\hbar}\right), \tag{2.20}$$

as shown in Fig. 2.10b.

The polarization values are corrected for the experimental polarization limit that is measured independently. This limit is fairly constant, decreasing for the smallest and

largest possible coil frequencies, as specified in section 2.6. The slight sensitivity on the tilt angle of the coils and on the neutron velocity is considered as well in this correction factor. Since the polarization limit does not depend on the scattering angle at the sample, it may be determined in direct beam experiments.

The declines in polarization with increasing spin-echo time stemming from other individual effects can be calculated each with the Matlab-programm SeRescal [39] using given instrument settings and experimentally determined parameters. Specifically, the mosaic spread can be measured on the same instrument for the same illuminated volume of the sample, as explained in paragraph 2.4. The mosaic spread in the sample must typically be much less than one degree for spectral linewidth measurements to be viable, which sets stringent conditions for the sample quality. Further, the acoustic phonon dispersion tapers when nearing the Brillouin zone center. This means that the dispersion slope within the triple-axis resolution is generally not flat and can thus not be matched by the planes of constant spin-echo face. Since the spectral function S and the NRSE resolution function F can be written as a convolution of the instrumental effects, the mosaic spread of the sample, the dispersion curvature and the lineshape in momentum and energy space, their Fourier transform is simply a multiplication, and so is the polarization.

The improvement of the resolution of NRSE with respect to the triple-axis resolution is demonstrated in Fig. 2.11. The TAS resolution ellipsoid becomes visible when the instrument is moved through the point-like Bragg peak. To make the lines of constant spin-echo phase show up as sinusoidal variations in the intensity, a signal that is extended in energy would be more straightforward to use. Then the frequencies $\nu_1 = \nu_2$ could be held constant, and k_I fixed, so that the phase would vary with k_F. Instead a trick is implemented: ν_2 is adjusted to the scattered elastic neutrons for any inelastic setting of the instrument.

2.3.3. NRSE **for measuring relative dispersion energies**

When scans are carried out in the same instrument configuration but different sample environments A and B, the relative shift $\phi_0^A - \phi_0^B$ between the spin-echo scans points out a wandering of the most probable scattering energy. This is used to extract energy shifts as a function of e.g. temperature from the spin-echo scans. To first order, the energy difference is

$$\left(\omega_0^A - \omega_0^B\right)\tau = -4\pi N m_n \frac{\nu_2 \left(L_{2,0}^A - L_{2,0}^B\right)}{k_F}. \tag{2.21}$$

If $L_{2,0}^A$ is longer, it compensates for the fact that the neutrons are relatively faster in the second spectrometer arm in situation A, i.e. the energy ω_0^A is smaller than ω_0^B. Since phase shifts of a multiple of 2π cannot be recognized, only energy differences $\Delta\omega_0 \ll 2\pi\hbar/\tau$ can be detected.
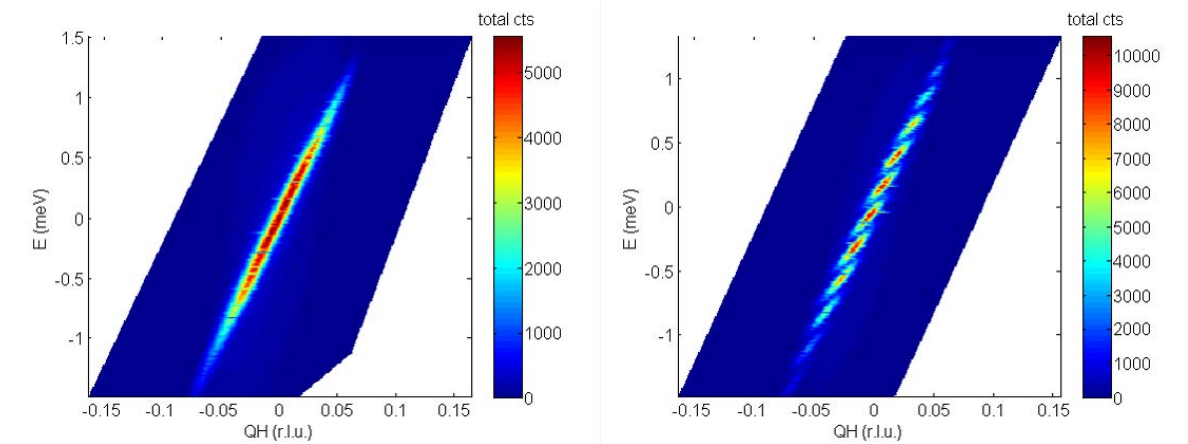
Figure 2.11.: *Demonstration of the* NRSE *energy resolution (right) compared to the* TAS *resolution (left) on* TRISP*. The* (220) *Bragg peak of a germanium crystal is used. The lines of constant spin-echo phase translate into sinusoidal variations in the intensity. The inclinations of the resonance coils are chosen so that* $\partial\omega/\partial q = 30\,meV\,\mathring{A}$.

In practice, the average value for the relative energy shift measured at various spin-echo times is taken.

2.4. Larmor diffraction for measuring the crystal mosaic spread

The mosaic spread of a single crystal can be measured using the Larmor diffraction setup shown in Fig. 2.12 [47]. The field boundaries are parallel to the lattice planes in this symmetric Bragg scattering configuration, which means that the tilt angles are $\theta_1 = \theta_B - 90°$ and $\theta_2 = -\theta_1$. The field directions in the second arm are inverted with respect to the first arm like in an ordinary spin-echo setup. The figure illustrates how the lengths of the field-free drift regions before and after the sample become unbalanced if Bragg scattering from crystallites tilted by an angle α passes through the configuration. The total Larmor precession phase is then

$$\phi(\nu) = 8\pi N \frac{m_n}{\hbar k} \nu L \alpha \cot(\theta_B) + O(\alpha^2), \qquad (2.22)$$

with N as before the number of operating coils in each bootstrap (two in the figure). The larger the mosaic spread of the sample, which is assumed to be gaussian with half width at half maximum α_{HH}, and the larger the transmission for neutron flight paths that are
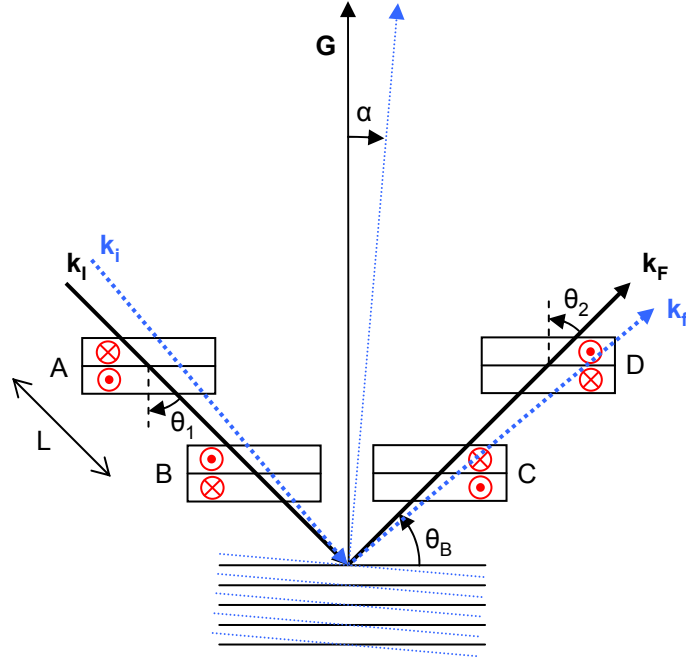
Figure 2.12.: *Larmor diffraction setup for measuring the mosaic spread α_{HH} in a crystal. The fields in the second arm are reversed with respect to the fields in the first arm. The solid black lines depict the optimal scattering orientation whereas the dotted blue lines depict the scattering from tilted crystallites. In the position shown, the angle α is negative.*

nonparallel to the instrument configuration, the sooner the final polarization will decrease with increasing ν [47]:

$$P(\nu) = P_0 \exp\left[-\left(8\pi N \frac{m_n}{\hbar k}\nu L\right)^2 \frac{\cot^2\theta_B}{4\ln 2}\left(\frac{1}{\mathrm{A3}_{\mathrm{HH}}^2} + \frac{1}{\alpha_{\mathrm{HH}}^2}\right)^{-1}\right] \qquad (2.23)$$

with the rocking scan half width at half maximum $\mathrm{A3}_{\mathrm{HH}}$, typically ca. 0.4° at standard settings of TRISP.

2.5. Measurement of the superconducting transition temperature

The superconducting transition temperature T_c is commonly determined using a physical property measurement system (PPMS) by means of the sudden change in resistivity or magnetization. The PPMS however does not accommodate the large single crystal samples used in this work, which is why the NRSE-TAS setup is used instead to determine T_c [20]. Since magnetic fields are acutely expelled from the sample below T_c because of the Meissner

effect, the Larmor precession phase of the neutrons makes a jump at this temperature when there is a weak field applied at the sample area. A magnetic field in the z-direction is created by winding a Helmholtz coil on the outside of the cryostat. If each of the two coils consists of $N = 10$ loops of copper wire with $\varnothing = 0.75\,\mathrm{mm}$ carrying a current of $I \approx 10\,\mathrm{A}$, the field is $B = (4/5)^{3/2}\mu_0 NI/R \approx 9\,\mathrm{G}$ where μ_0 is the permeability constant and R is the radius of the coils. The accumulated Larmor precession phase in this field is roughly $100°$ for $k = 2.51\,\text{Å}^{-1}$ neutrons. Since below T_c the field lines are only expelled from the sample itself and compressed around it, the relative phase change is a fraction of this value.

2.6. The spectrometer TRISP @ FRM II

Worldwide, there are only a couple of unique triple-axis NRSE spectrometers, e.g. the IN22 with ZETA at the Institut Laue-Langevin and the cold neutron spectrometer FLEXX at the Helmholtz Zentrum Berlin. The neutron source FRM II supplies a thermal beam line to the instrument TRISP (Fig. 2.13), which is located at the end of a 10 m long polarizing guide with a lower critical wavelength $\lambda_c = 0.8\,\text{Å}$, followed by a velocity selector. The pyrolytic graphite (PG) monochromator crystals, set for the (002) reflection, allow for variable vertical and horizontal focusing. Coupling coils guide the polarization to the first resonance coil and from the last coil to the analyzer. The sizes of the beam windows are $50 \times 120\,\mathrm{mm}^2$. The surfaces of the resonance coils (shown in Fig. 2.14) are flat within $10^{-2}\,\mathrm{mm}$ so that the length and shape of the precession regions are precisely defined. Relative accuracies of the Larmor precession angle of 10^{-6} are possible. Surrounding mu-metal shields reduce the residual field along the flight paths to less than $5\,\mathrm{mG}$ (ca. 100 times less than the earth magnetic field). Horizontal and vertical compensating coils are used to cancel the residual field around the sample for each spectrometer alignment. A closed cycle cryogen-free pulse tube cryostat with a sample stick is used to cool the sample to temperatures as low as $3\,\mathrm{K}$ [48]. While early measurements were made using a PG(002) analyzer and a polarizing bender, most measurements featured in this work are made with a polarizing Heusler alloy analyzer.

The range of spin-echo times at which the polarization can be measured is limited by the accessible range of coil frequencies $50\,\mathrm{kHz} \le \nu < 400\,\mathrm{kHz}$. Because this frequency must be in resonance with the static field, magnitudes for the latter range from ca. $170\,\mathrm{G}$ to $1.4\,\mathrm{kG}$. The rotating field strength that is needed to complete the spin π-flips for coil lengths $d = 5\,\mathrm{cm}$ and neutrons with wavevector $k = 2.51\,\text{Å}^{-1}$ can be estimated to be $B_{\mathrm{rf}} \approx 50\,\mathrm{G}$. Consequently, below the minimum frequency (minimum spin-echo time), the direct beam polarization starts to suffer due to random spin flips that come with a violation of the rotating-wave approximation for $B_{\mathrm{rf}} \ll B_0$.

Figure 2.13.: *The* NRSE-TAS *instrument* TRISP *at the neutron source* FRM II, *side view (with cryostat) and top view. The monochromator is enclosed in the cyan-colored concrete shielding. Photos from Ref. 20.*
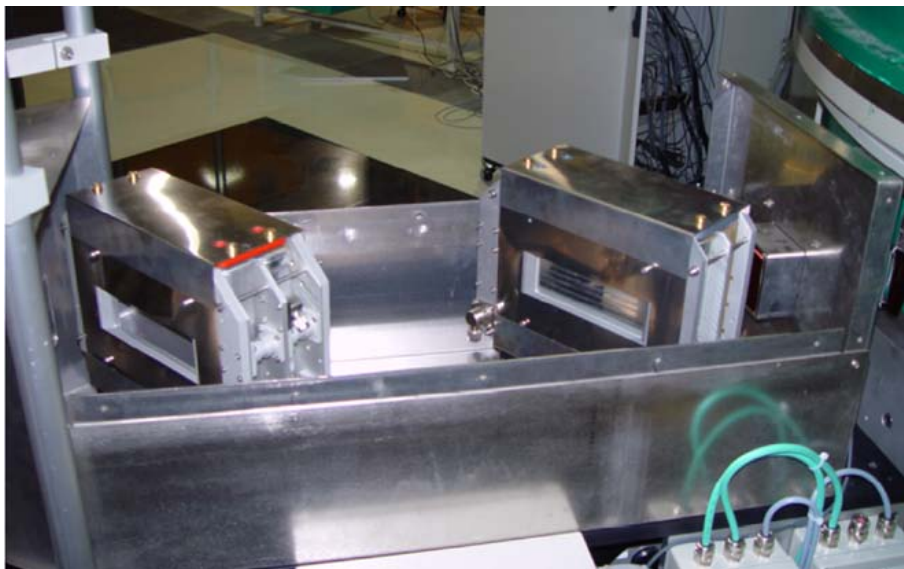
Figure 2.14.: *The mu-metal shielding here is removed to reveal the rf coils of the instrument* TRISP*. Photo from Ref. 20.*

3. Superconductivity-induced phonon lineshape asymmetry and the spin-echo polarization decay

3.1. Introduction

Spin-echo measurements give access to the cosine Fourier transform of the spectral lineshape of the excitation in question. Harmonic excitations have a Lorentzian lineshape, leading to an exponential polarization decay. The half-width at half-maximum (HWHM) of the Lorentzian, Γ, can then be extracted from the data. If there are two nearby modes, the polarization profile shows an oscillation. The oscillation gives information about the relative weight of the peaks and the distance between their centers. Habicht *et al.* [49] developed an analytic formalism to describe this and delivered experimental evidence by creating an artificial magnon line split-up using two misplaced grains of RbMnF$_3$. Lately, Nafradi *et al.* [50] observed an intrinsic magnon mode splitting in a spin$-1/2$ ladder compound.

Previously, linewidths in the transverse acoustic phonon branches in the conventional BCS-type superconductors Nb and Pb were measured in the normal and superconducting state, respectively. The latest work is covered in the PhD thesis of Aynajian [20]. The phonon linewidth broadening was assumed to be due solely to electron-phonon interaction. Deviations from exponential spin-echo decay profiles were not found within the experimental error. This means that single Lorentzian modes were apparently observed. The linewidths could thus be directly extracted for various points on the phonon branches. In the superconducting state, a discontinuity was observed in the linewidths at the phonon energy corresponding to the energy gap $2\Delta(T)$, as expected. In an effort to fit this "jump" with a simple function, the electronic excitation spectrum function given by the BCS theory was used [19]. The choice of this function can be understood in the following way: the phonon linewidth in the normal state is proportional to the electronic density of states at the Fermi energy, $N_n(0)$ [51]. This is true under the assumption that the electronic structure is constant for electron energies ε within the range of the phonon energy from

the Fermi edge. In the BCS theory, this is not the case anymore, instead the electronic density of states $N_{\text{sc}}(\varepsilon)$ is given by the excitation spectrum function

$$N_{\text{sc}}(\varepsilon) = N_{\text{n}}(0) \operatorname{Re} \left[\frac{|\varepsilon - i\Gamma_{\text{broad}}|}{\sqrt{(\varepsilon - i\Gamma_{\text{broad}})^2 - \Delta^2}} \right]. \tag{3.1}$$

The symbol Γ_{broad} introduces a temperature-dependent smearing of the gap edge due to the electron self-energy [52]. In a crude approach one could thus assume that a phonon with energy ω foremost exciteps quasiparticles with energy $-\omega/2$ to $+\omega/2$ and that thus the linewidth is proportional not to $N_{\text{n}}(0)$ as in the normal state but to the density of states $N_{\text{sc}}(\varepsilon/2)$, though this is technically incorrect.

This approach conceals the more fundamental underlying situation that the broadened acoustic phonon spectral function gradually moves through the abrupt change of state at the superconducting energy gap, which causes a lineshape distortion. This was first observed in the nickel borocarbides (see section 3.1.2) [24]. The effect was deemed not to be significant under anything other than extreme conditions. However, from recent neutron triple-axis scattering data on a transverse acoustic branch in Nb it transpired that the lineshape alteration may in fact be more generally prevalent [26]. Since the energy resolution of the spin-echo method is much better than that of conventional spectroscopy, the question arises why no deviations of the exponential polarization decay have been spotted.

Thus the aim of this chapter is to reconcile the neutron resonance spin-echo (NRSE) data with the given triple-axis data. For this purpose, spin-echo polarization decay profiles were measured anew with improved momentum resolution and over a broader range of spin-echo time. The simplified approximation previously used to fit the linewidths as a function of wavevector in the superconducting state is replaced by a refined treatment. Shifts of the energy expectation value of the spectral lineshape with respect to the normal state are extracted from the NRSE data for both Nb and Pb, making use of the fact that the previously disregarded Larmor phase shift is directly proportional to the neutron energy change. Together with the polarization decay profiles, the energy shifts give a full picture of the phonon renormalization. Within this framework, the role of the previously considered Kohn anomaly, which is situated exactly where phonons are most affected by the opening of the superconducting energy gap, is discussed. Since the Kohn anomaly in fact appeared less pronounced in the new measurements with improved accuracy, the linewidths were again measured over an extended range in the [001] transverse phonon branch to resolve the characteristics.

3.1.1. Electron-phonon coupling and normal state phonon spectra

A brief look at the mathematical framework to describe the normal state is required to understand the changes that occur upon entering the superconducting state.

At low temperatures, just above the superconducting transition temperature T_c, the "playground" of phonons is dominated by interaction with electrons, which screen out the field of the ions in their coupled motion. After all, the phonon occupation number is so low that phonons hardly interact with each other. Spontaneous decay of low energy phonons into two or more phonons is also kinetically difficult (see e.g. [53]). Further, it is assumed that lattice defects and disorder can be neglected for the single crystals of niobium, which consists of one isotope only, that are used in the experiment. Consequently, impurity scattering is assumed to be negligible. Thus only the electron-phonon (e-ph) interaction is of further interest.

In a neutron inelastic scattering experiment the one-phonon spectral function $S(\mathbf{q}, \omega)$ is measured. The phonon is labeled by its wavevector $\mathbf{q}$, the notation ν for the branch under consideration is omitted for clarity unless it deserves special attention. Though classically ω represents an angular frequency and Planck's constant $\hbar$ transforms it into energy, we shed $\hbar$ here and refer to ω directly as energy. The spectral function is linked to the phonon's bare Green's function D_0 and its self-energy (polarizability) Π due to the e-ph interactions by the Dyson equation:

$$S(\mathbf{q}, \omega) = -\operatorname{Im} D(\mathbf{q}, \omega) \tag{3.2}$$

with

$$D(\mathbf{q}, \omega)^{-1} = D_0(\mathbf{q}, \omega)^{-1} - \Pi(\mathbf{q}, \omega) \tag{3.3}$$

and

$$D_0(\mathbf{q}, \omega)^{-1} = \frac{\omega^2 - \Omega_\mathbf{q}^2}{2\Omega_\mathbf{q}}. \tag{3.4}$$

Thus, if interactions would be switched off, the phonon would have energy $\Omega_\mathbf{q}$ and infinite lifetime.

Now, the self-energy of a particle, in general, represents the contribution to its total energy due to all interactions with the system it is part of. While the probability of phonon decay is described by the imaginary part of the complex self-energy function $\Pi(\mathbf{q}, \omega)$, the real part of the self-energy is associated with a frequency shift. The two are interconnected by the Kramers-Kronig dispersion relations [54, 55]

$$\operatorname{Re} \Pi(\omega) = \frac{2}{\pi} P \int_0^\infty \mathrm{d}\omega' \frac{\omega' \operatorname{Im} \Pi(\omega')}{\omega'^2 - \omega^2} \tag{3.5}$$

$$\operatorname{Im} \Pi(\omega) = -\frac{2}{\pi} P \int_0^\infty \mathrm{d}\omega' \frac{\omega \operatorname{Re} \Pi(\omega')}{\omega'^2 - \omega^2} \tag{3.6}$$

with P the Cauchy principal value of the integral. The Kramers-Kronig relations are generally valid for all complex functions that are meromorph (=analytic with isolated poles) in the upper half-plane. Since response functions in physical systems are subject to causality, the analyticity condition is automatically satisfied [56].

The contributions of e-ph interaction that are to be considered in the calculation of the phonon self-energy are illustrated in the Feynman diagrams of Fig. 3.1. The lowest-order
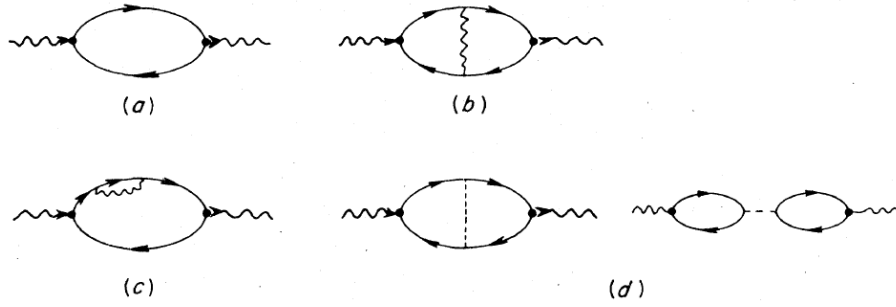
Figure 3.1.: *Feynman diagrams illustrating the contributions of e-ph interaction that are to be considered in the calculation of the phonon self-energy. (a) Creation and subsequent destruction of a bare electron-hole pair. (b) Second-order vertex correction. (c) Electronic self-energy term. (d) Higher order corrections due the Coulomb interaction. From Butler, Pinski and Allen [57].*

interaction is the creation and subsequent destruction of an electron-hole pair, as depicted in Fig. 3.1(a). Panel (b) depicts a second order vertex correction. Corrections of this type are negligible as long as the phonon momentum is larger than the ratio of phonon and electron velocities, $q[\text{r.l.u.}] \gg v_{ph}/v_F$ [57]. Usually this is the case, and one speaks of the "Migdal approximation". In essence, it means that the bare coupling constant is already a good approximation of the vertex function. This follows from the quickness of the electron motion compared to the phonon motion. For the transverse phonon branch in niobium, this is well satisfied: $v_{ph} < 1.8 \cdot 10^5$ cm/s, the shear sound velocity in [100] direction [58], is much smaller than the Fermi velocity $v_F = 0.57 \cdot 10^8$ cm/s [59]. Corrections of the type shown in panel (c) are due to the effect that the phonons in turn have on the electrons. They can be discarded at low T as there are few phonons the electrons can interact with. The effectiveness of the screening *does* depend on the electron-electron interaction though, which is why the Coulomb interactions of panel (d) do need to be included in the calculations.

Next, Fermi's golden rule for the lowest-order electron-hole pair creation and destruction (Fig. 3.1(a)) gives the phonon self-energy. It is obtained by integrating over all electron energies ε and over all electron momenta $\mathbf{k}$. The electron-phonon coupling constant for a transition from electron band n to n' and state $\mathbf{k}$ to $\mathbf{k}'$ is denoted by $g_{n,\mathbf{k};n',\mathbf{k}+\mathbf{q}}$. Herewith one can write the self-energy

$$\Pi(\mathbf{q},\omega) = -2i \sum_{n,n'} \int \frac{V_a}{(2\pi)^3} \mathrm{d}^3 k \int \mathrm{d}\varepsilon \, G^0(\mathbf{k},\varepsilon) G^0(\mathbf{k}+\mathbf{q},\varepsilon-\omega) |g_{n,\mathbf{k};n',\mathbf{k}+\mathbf{q}}|^2 \qquad (3.7)$$

where $(2\pi)^3/V_a$ is the Brillouin zone volume and G^0 is the electron propagator

$$G^0(\mathbf{k},\varepsilon) = \frac{1}{\varepsilon - \varepsilon_{\mathbf{k}}^0 + i\delta \mathrm{sign}(\mathbf{k}-\mathbf{k_F})} \qquad (3.8)$$

with $\varepsilon_{\mathbf{k}}^0$ the electron band dispersion. The standard definition of the electron-phonon matrix element is [60, 9]

$$g_{n,\mathbf{k};n',\mathbf{k'}}^{\mathbf{q},\nu} = \langle \psi_{n',\mathbf{k'}}^0 | \frac{\hat{\epsilon}_{\mathbf{q},\nu}}{\sqrt{M\omega_{\mathbf{q},\nu}}} \cdot \nabla V_{\text{eff}} | \psi_{n,\mathbf{k}}^0 \rangle \delta(\mathbf{k} - \mathbf{k'} - \mathbf{q}) \tag{3.9}$$

with M the (averaged) atomic mass and $\psi_{n\mathbf{k}}^0$ is the electron Bloch wave function for band n and state $\mathbf{k}$ for the undistorted crystal. The phonon polarization comes in at $\hat{\epsilon}_{\mathbf{q},\nu}$ (not to be confused with the electron energy ε); herewith, the coupling constant can be markedly different for transverse and longitudinal phonons. For transverse phonons, the coupling to direct processes is generally very small, so that processes from higher Brillouin zones may contribute disproportionately. The quantity ∇V_{eff} is the self-consistent change of the crystal potential caused by a phonon distortion. A fully screened potential is adopted to include the Coulomb interactions between the electrons, Fig. 3.1(d). Though calculating the coupling element $|g_{\mathbf{k},\mathbf{k}+\mathbf{q}}|^2$ is a difficult task, its behavior is generally "slower" than the structure-rich integral over the electron propagators. It may then in a first approximation be assumed that the coupling is constant for a phonon branch so that it can be removed from the integral. Then, the self-energy is directly proportional to the electron susceptibility. This static electron response is also called the nesting function. It is, put simply, the overlap with the original Fermi surface after a translation by the wavevector $\mathbf{q}$. It will come to use in section 3.2 to confirm the electronic nature of the normal state anomaly in the $(\xi 00)\mathrm{T}$ phonon branch in Nb.

Plugging Eq. 3.7 into Eq. 3.2 gives

$$S(\mathbf{q},\omega) = \frac{-\operatorname{Im}\Pi(\mathbf{q},\omega)}{\left(\frac{\omega^2-\Omega_{\mathbf{q}}^2}{2\Omega_{\mathbf{q}}} - \operatorname{Re}\Pi(\mathbf{q},\omega)\right)^2 + \left(\operatorname{Im}\Pi(\mathbf{q},\omega)\right)^2}. \tag{3.10}$$

Now it is apparent that indeed the real part of the self-energy renormalizes the phonon energy whereas the imaginary part causes the linewidth broadening. For well-defined phonons, the linewidth is much smaller than the phonon energy and the lineshape is nearly Lorentzian. Note that the anti-Stokes term is included in the equation above, whereas a simple Lorentzian would violate the positive/negative energy balance. Since the bare phonon frequency $\Omega_{\mathbf{q}}$ cannot be measured, the real part of the self-energy is usually incorporated so that one gets the real normal state "nominal" phonon energy $\omega_{\mathbf{q}}$. Unlike the self-energy, the linewidth is defined only on the dispersion surface in $(\mathbf{q},\omega)-$space. After all, the linewidth can only be measured there where the scattering function is non-zero and thus has no meaning elsewhere in the momentum-energy continuum. The self-energy and the linewidth are interconnected by [25]

$$-\operatorname{Im}\Pi(\mathbf{q},\omega) = \frac{\omega}{\omega_{\mathbf{q}}}\Gamma(\omega_{\mathbf{q}}), \tag{3.11}$$

which means the imaginary part of the self-energy has the same value as the linewidth at the dispersion energy, but goes to zero when ω does.

3.1.2. Phonons near the superconducting gap edge

Before we turn to the phonon renormalization in the superconducting state, the historical background of experimental and theoretical research of $\mathbf{q} \neq 0$ phonons with energy near that of the superconducting gap $2\Delta(T)$ is recapitulated.

If the system undergoes a transition from normal to superconducting state, in a quasiparticle description, the entire interaction is captured in the superconducting gap $2\Delta(T)$ that appears around the Fermi energy ε_F. This means that the electronic decay channel is closed for phonons with energy smaller than $2\Delta(T)$. They have no means to interact and thus have zero linewidth. Phonons with higher energies can excite electrons from the occupied states below $\varepsilon_F - \Delta(T)$ to empty states above $\varepsilon_F + \Delta(T)$ (and in the Cooper pair picture, break up pairs). The phonon linewidth is directly proportional to the densities of the involved electronic states. Due to the pile-up of electronic states around the edges, the linewidth is increased compared to the normal state for phonons just above $2\Delta(T)$.

Phonons with energy $\sim 2\Delta(T)$ require special attention whenever their linewidth broadening due to e-ph coupling is substantial in the normal state. Because of the large linewidth of these phonons, they split into two parts; one just below the gap, which is narrow due to the reduced e-ph coupling, and a broader remainder above the gap. This was first observed in the intermetallic nickel borocarbide superconductor $YNi_2^{11}B_2C$ in 1996 [24] (see Fig. 3.2). With a superconducting gap width of $\sim 4.3\,\mathrm{meV}$, a phonon peak energy of $\sim 7\,\mathrm{meV}$ and HWHM $\sim 2.5\,\mathrm{meV}$, the extra mode could be distinguished relatively easily. Fig. 3.2 also displays that the phonon is marked by anomalous behavior in the normal state: it softens when the sample is cooled. This is typical of strong electron-phonon coupling. The resonance at first eluded correct interpretation: though the authors note that it had "phonon character" and that it absorbed the spectral weight of the above-lying soft phonon mode, the fact that the peak energy of the phonon itself lies above 2Δ caused confusion. The discontinuity at 2Δ later allowed for the superconducting energy gap to be determined directly from triple-axis data on a single phonon in this material [61]. Before, energy gaps had only been determined from neutron data by measuring multiple points along the phonon branch with steadily increasing energy and observing a sudden change in linewidth.

From such phonon scans in niobium in the superconducting state below $T_c = 9.25\,\mathrm{K}$, Shapiro *et al.* [14] had determined the saturated gap width in this material to be $2\Delta_{[100]} = 3.20 \pm 0.05$ meV. In niobium, the phonon half widths in the normal state are more than an order of magnitude smaller than in the nickel borocarbides and therewith comparable to the neutron instrumental resolution. Recently, Weber and Pintschovius collected more precise triple-axis data of acoustic phonons near the gap edge using cold neutrons [26]. They observed an increased asymmetry in the superconducting state at several $\mathbf{q}$-points in the (001) transverse phonon branch. The results are shown in Fig. 3.3. The normal state data (red lines) are already asymmetric due to the instrumental resolution ellipsoid
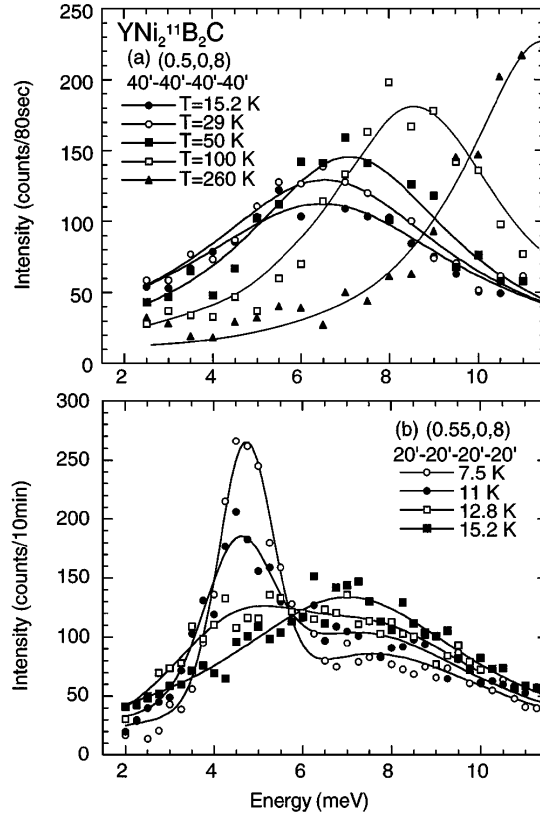
Figure 3.2.: *Triple-axis scans from Kawano et al., Ref. [24], showing the emergence of a "resonance peak" upon entering the superconducting state for a phonon with energy near $2\Delta_0 \sim 4.3\,meV$ in $YNi_2^{11}B_2C$. The phonon at $\mathbf{Q} = (0.5, 0, 8)$ softens with decreasing temperature as the strong e-ph coupling takes hold for $T > T_c$ (top). For $T \lesssim T_c$ and the nearby wavevector $\mathbf{Q} = (0.55, 0, 8)$, a resonance was discovered (bottom panel), the resolution of which was limited by the instrument.*

traversing the cone-shaped dispersion during the energy scan. The theoretical fit to the superconducting state data (blue symbols) consists of a convolution of a distorted lineshape with the instrumental resolution (shown extra on the right-hand side). Though the split-up of the phonon into a part above the gap and a resonance below the gap is largely obscured, the increased asymmetry of the data supports an altered lineshape. In the paper, the best agreement between calculation and experiment is found for $2\Delta_0 = 3.20 \pm 0.02$ meV.

The lineshape effect was in fact qualitatively correctly predicted by Schuster in 1973 [62]. In subsequent years, numerical work on the superconducting state self-energy for $q \neq 0$ phonons was carried out by Zeyher [63] and Marsiglio [64]. After the experimental work on the nickel borocarbide superconductor, Kee and Varma focused on the distorted lineshape again, stressing the requirement for nesting [65]: they criticized the dimension and momentum independence of the singularity directly at the gap edge in Schuster's work. Sure enough, kinematic constraints must be taken into account in addition to the energy constraints in the superconducting state that we have regarded so far. If the normal state
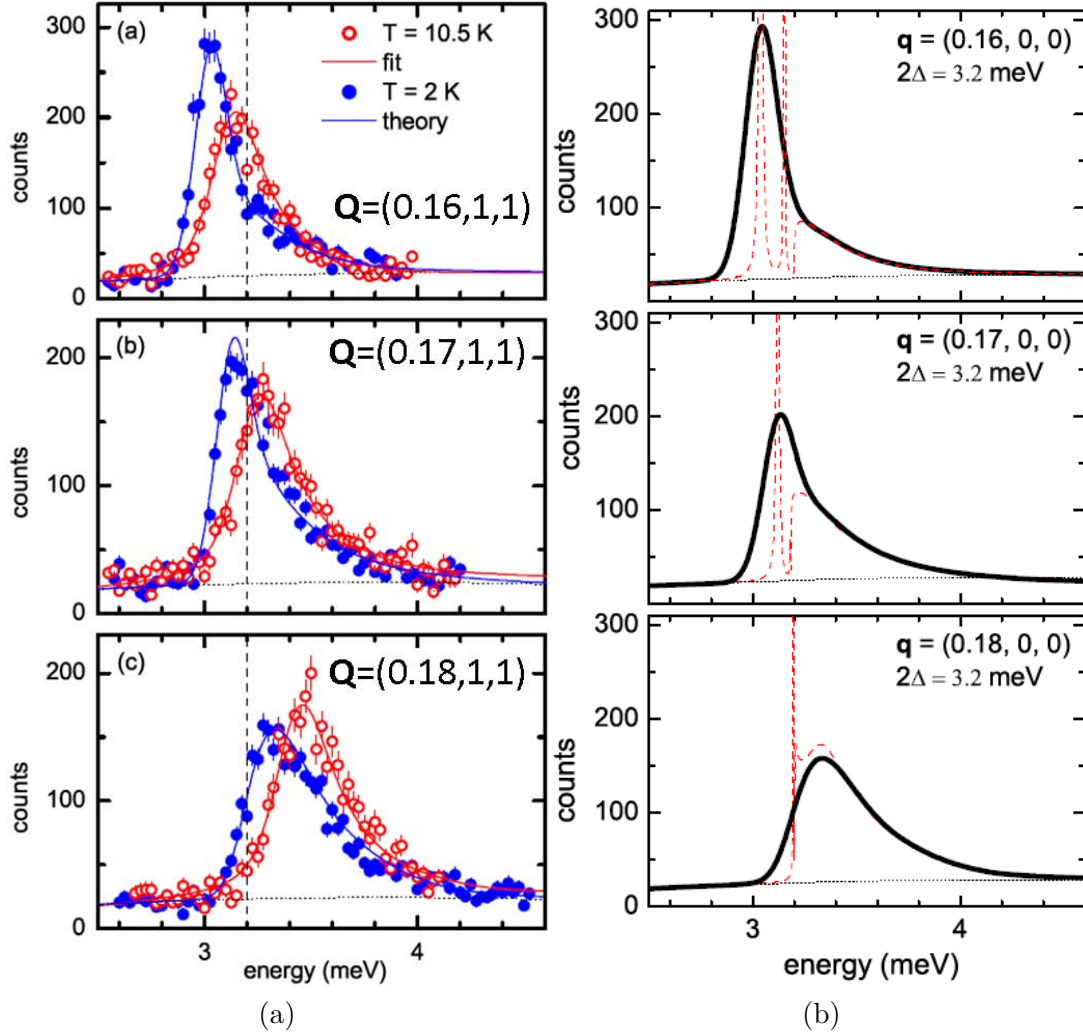
Figure 3.3.: *Figures from Weber and Pintschovius, Ref. [26]. (a) Triple-axis scans showing the change in lineshape upon entering the superconducting state at $T = 1.8\,K$ for phonons with energy near and above $2\Delta_0$ in Nb $(00\xi)\,T$. The normal state data (red open circles) are asymmetric due to instrumental resolution, specifically because of the cone-shaped dispersion. While the maximum of the normal state phonon at $\xi = 0.16\,r.l.u.$ is still below the gap (dashed vertical line), the phonons at $\xi = 0.17$ and $0.18\,r.l.u.$ lie above the gap. The theoretical fit to the superconducting state data (blue closed circles) consists of a convolution of the lineshape distortion by Allen's theory (see paragraph 3.1.3), shown as dashed lines in (b), with the instrumental resolution.*

self-energy from Eq. 3.7 is low, because the electron susceptibility is small, there will be hardly any change in the superconducting state.

While Kee and Varma perceived the resonance as an extra mode, set apart from the phonon narrowing as the energy goes below 2Δ, Allen, Kostur, Takesue and Shirane [25] specifically link the two in a conventional BCS approach more in the line of Schuster's work. They explain that if the initial phonon energy is far below the gap, the sharp peak contains the majority of the spectral weight and represents a phonon which cannot decay. Counter-intuitively, this phonon softens, even though its lifetime increases, as was noticed also by others. When the normal state phonon has a mean energy above 2Δ and a tail stretching below, there is a sharp feature in the superconducting state pinned just below the gap that can be regarded as a "mixed vibrational/superelectronic collective excitation" [25].

Allen *et al.* deploy a quasi-isotropic model, whereas the calculations of Marsiglio, amongst others, are suitable for systems ranging from quasi-isotropic to ideally nested. The quasi-isotropic model makes use of the fact that for intricate Fermi surfaces in three dimensions, the static transition possibilities are, other than in the one-dimensional case, not confined to a single wavevector that equals the Fermi diameter $2k_F$. Thus, if the Fermi surface topology is both convex and concave at places, the self-energy as a function of wavevector is smoothed. In this case, the effects of the combination of simultaneous energy and momentum constraints disappear. The advantage of this model is that the renormalization in the superconducting state is described by few normal-state parameters instead of a complete electronic bandstructure.

Karakozov and Maksimov revisit the problem in Ref. [66] and show that at a nesting vector, the real part of the self-energy possesses a square-root singularity at $2\Delta(T)$, exactly of the same type as at $q = 0$. This directly contradicts the paper by Kee and Varma who also assumed nesting conditions, and neither does it agree with the result of Allen *et al.*, as both these groups find a logarithmic singularity. Notwithstanding, the predictions bear an overall resemblance to one another.

The following analysis of the transverse acoustic phonons near the gap edge in the [001] direction in niobium is based on the theory of Allen, which has the advantage of simplicity. More than that, it allows for a direct comparison with the experimental findings of Weber and Pintschovius, as they also used this theory as a guideline for the analysis.

3.1.3. The spectral function in the superconducting state after Allen *et al.*

From this short overview of the experimental and theoretical publications regarding the phonon lineshape distortion at $\sim 2\Delta(T)$, we introduce without further ado the explicit formula for the spectral function in the superconducting state as used in Ref. [25]:

$$S_{\mathrm{sc}}(\mathbf{q}, \omega) = \frac{4\omega r_{\mathbf{q}}\omega_{\mathbf{q}}^2 \frac{\Gamma_{\mathrm{s}}}{\Gamma_{\mathrm{n}}}(\omega)}{\left[\omega^2 - \omega_{\mathbf{q}}^2 - 2\omega_{\mathbf{q}}^2 r_{\mathbf{q}} \frac{\mathrm{Re}\,\delta\Pi}{\Gamma_{\mathrm{n}}}(\omega_{\mathbf{q}}, \omega)\right]^2 + \left[2\omega r_{\mathbf{q}}\omega_{\mathbf{q}}\frac{\Gamma_{\mathrm{s}}}{\Gamma_{\mathrm{n}}}(\omega)\right]^2} \tag{3.12}$$

where $\omega_{\mathbf{q}}$, as mentioned before, is the nominal energy of the phonon with wavevector $\mathbf{q}$ in the normal state just above T_c. The normal state linewidth enters via the parameter

$$r_{\mathbf{q}} = \Gamma_{\mathrm{n}}(\omega_{\mathbf{q}})/\omega_{\mathbf{q}}, \tag{3.13}$$

and is multiplied with the ratio of the linewidths in the superconducting and the normal state $\Gamma_{\mathrm{s}}/\Gamma_{\mathrm{n}}$. The latter is equal to the ratio of the imaginary parts of the self-energy $\mathrm{Im}\,(\Pi_{\mathrm{s}}/\Pi_{\mathrm{n}})$, because for both states Eq. 3.11 is valid. The real part of the self-energy difference between normal and superconducting state, $\mathrm{Re}\,\delta\Pi = \mathrm{Re}\,(\Pi_{\mathrm{s}} - \Pi_{\mathrm{n}})$, describes the energy shift with respect to the normal state. If the linewidth ratio goes to one and $\mathrm{Re}\,\delta\Pi$ approaches zero, the normal state spectral function (Eq. 3.10) is retrieved. From the similarity between these equations, it is clear that Eq. 3.12 on itself does not contain any new information: one still needs a separate expression for the self-energy change.

As mentioned in the last section, a quasi-isotropic BCS approach is used, so that the ratio of linewidths in the superconducting and normal state can be described by an integral over the initial and final electron energies only. In the end, the linewidth ratio is re-written entirely in terms of normalized energy $\omega/2\Delta_0$ and temperature T/T_c, irrespectively of $\omega_{\mathbf{q}}$. The lengthy but straightforward formula for the linewidth ratio reads

$$\Gamma_{\mathrm{s}}/\Gamma_{\mathrm{n}} = r_1 + r_2 \tag{3.14}$$

with

$$\begin{aligned} r_1 &= \frac{2}{\nu} \int_0^{\pi/2} \frac{\mathrm{d}\theta}{\sin^2\theta} \frac{1 + \nu\sin\theta - \sin^2\theta}{\sqrt{(1 + \nu\sin\theta)^2 - \sin^2\theta}} \\ &\quad \times \left[f\left(\frac{\Delta(T)}{\sin\theta}\right) - f\left(\omega + \frac{\Delta(T)}{\sin\theta}\right) \right] \end{aligned} \tag{3.15}$$

and

$$\begin{aligned} r_2 &= \int_0^{\pi/2} \mathrm{d}\theta \frac{(1-\mathrm{a}) + \mathrm{a}^2/2\cos^2\theta}{\sqrt{(1-\mathrm{a}) + \mathrm{a}^2/4\cos^2\theta}} \Theta\left(\omega - 2\Delta(\mathrm{T})\right) \\ &\quad \times \left[1 - f\left(\frac{\omega}{2}(1 + a\sin\theta)\right) - f\left(\frac{\omega}{2}(1 - a\sin\theta)\right) \right], \end{aligned} \tag{3.16}$$

where ν is $\omega/\Delta(T)$, a is $1 - 2\Delta(T)/\omega$ and

$$f(E) = \frac{1}{\exp(E/k_B T) + 1}. \tag{3.17}$$

Θ is the Heaviside step function. Mind a few minor errors in the paper [67][1]. Within this formula, the Clem description for the BCS gap $\Delta(T/T_c)/\Delta_0$ [68] is adopted:

$$\begin{aligned}
\Delta(t) &= \left[1 - (0.4095 - 1.362a_2)(1 - t) - (0.0626 + 0.318a_2)(1 - t)^2\right] \\
&\quad \times 1.7367\Delta_0(1 - a_2)\sqrt{1 - t},
\end{aligned} \tag{3.18}$$

with $t = T/T_c$ and a_2 a factor to include anisotropy. The Clem formula is valid above $t = 0.2$, below this temperature $\Delta(t) = \Delta_0$. The coupling limit $k_B T_c/(2\Delta_0)$ is the only material-specific parameter that enters the linewidth ratio. It is worth noting that the ratio goes to one as $T \to T_c$ as anticipated.

The real part of the self-energy difference between normal and superconducting state, $\mathrm{Re}\,\delta\Pi = \mathrm{Re}\,(\Pi_\mathrm{s} - \Pi_\mathrm{n})$, is derived by the Kramers-Kronig transformation (see Eq. 3.5)

$$\frac{\mathrm{Re}\,\delta\Pi}{\Gamma_\mathrm{n}}(\mathbf{q}, \omega) = \frac{1}{\omega_\mathbf{q}} \cdot \frac{2}{\pi} \int_0^\infty \mathrm{d}\omega' \frac{\omega'^2 \left(1 - \frac{\Gamma_\mathrm{s}}{\Gamma_\mathrm{n}}(\omega')\right)}{\omega'^2 - \omega^2}. \tag{3.19}$$

Note that the integration itself is independent of $\mathbf{q}$ and thus only needs to be executed once.

The theory of Allen *et al.* is worked out and illustrated for the case of Nb (100)T phonons in section 3.3. The normal state dispersion and linewidths are used as input information to describe the superconducting state.

3.2. Nb (100)T: normal state phonon dispersion and linewidths

Nakagawa and Woods realized early on that the dispersion of phonons for the high symmetry directions in Nb displays many striking features [69]. Born-Von Kármán (BvK) fits to the data require many parameters, meaning there are long-range forces in the ionic displacement model. One striking feature can be found in the $(\xi 00)$ transverse phonon branch, which has an unusual curvature, falling below the sound velocity for $\xi \gtrsim 0.1$

---

[1]In Equation (3) and (4) of the paper, the factors β need to be removed, so that the explicit temperature dependence is not immediately canceled from the Fermi-Dirac functions. A factor $2/\nu = 2\Delta(T)/\omega$ is missing in r_1. The integration limit used for Fig. 2 must have been ca. 15 instead of $1000 \cdot 2\Delta_0$, which is why the real part of the self-energy does not go to zero for $\omega \to 0$. The resonances below the gap are in fact sharper than in the figures of the unbroadened lineshapes of the paper.

and increasing above it later on. In 1975, Shapiro, Shirane and Axe [14] performed TAS measurements at low temperatures. They found an anomalous decrease in energy of 15% near $\xi \sim 0.2$ when the temperature is lowered from $300\,\mathrm{K}$ to T_c. Purely phononic interactions would give an opposite temperature dependence. The phonon softening is another indicator for the presence of a Kohn anomaly: at low temperatures, the Kohn anomaly is fully developed, while at high temperatures the phonon frequency might be stabilized by anharmonic interactions between the electrons.

Even though the dip in the dispersion is thus experimentally well-established, Aynajian *et al.* measured a concomitant peak in the intrinsic linewidths only recently [20, 19]. During the present work, incertitude over the distinctiveness of the normal state linewidth anomaly arose. Thus, we measured a whole new set of linewidths. Experimental details and a rigorous comparison between present and prior data is provided in the next section. The comparison of different "runs" using the same sample may serve as a general indication of the accuracy of TRISP results irrespective of instrumental updates and individual-related data analysis.

Since only the self-energy that is due to interaction with electrons is changed in the superconducting state, it is important to corroborate the electronic nature of the normal state linewidth anomaly. This is done in the subsequent section.

3.2.1. Compilation of present and prior linewidth data

Aynajian *et al.* measured intrinsic linewidths of the $(\xi 00)\mathrm{T}$ phonon branch at TRISP [20, 23]. The dispersion as measured at $T = 3.5\,\mathrm{K}$ and phonon linewidths at both 3.5 and $12\,\mathrm{K}$, respectively, are shown in Fig. 3.4. Though the dispersion data are recorded in the superconducting state and are thus renormalized, the energy shifts are only of the order of $0.1\,\mathrm{meV}$, as will be shown later on in this chapter, and thus the observable features in this picture are in fact normal state effects. The dip near $\xi \sim 0.2$ that was pointed out by Nakagawa and Woods is obvious. First-principles calculations for the dispersion using the density functional theory (DFT) framework in the local density approximation (LDA) are also shown. As can be seen, they are not viable at small wave vectors, because in the calculation, the numerical values of the phonon frequencies are unstable due to higher-order effects.

Though the 4-parameter Born-Von Kármán fit that is also shown in the graph gives a decent approximation over the entire wavevector range, it does not capture the shoulder at $\xi = 0.17\,\mathrm{r.l.u.}$ ideally; using up to eight parameters does not improve the goodness of fit. This is a consequence of the restricted applicability of the ionic displacement model: Kohn anomalies theoretically require an infinitely long-range force. A 4-parameter Born-Von Kármán fit over a shorter range $\xi < 0.40$ is therefore used to determine the normal state phonon energy $\omega_{\mathbf{q}}$ (see Fig. 3.5). Furthermore, energy differences between the normal
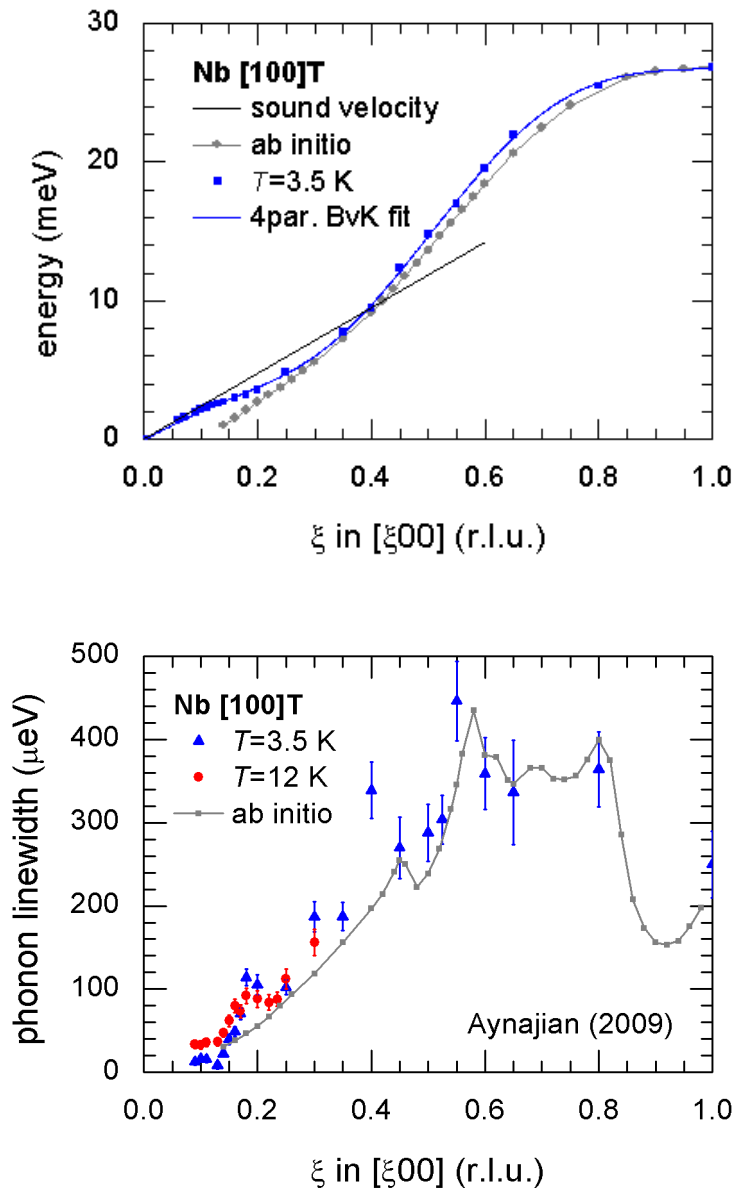
Figure 3.4.: *Dispersion at $T = 3.5\,K$ (top) and phonon linewidths (bottom) of the $(\xi 00)\,T$ branch in Nb, measured at* TRISP *and published by Aynajian et al. [19, 20]. The dispersion merges with the velocity of sound that is derived from the elastic constants in Ref. [70] (straight black line in top graph) in the long wavelength limit. Also shown are ab initio density functional perturbation calculations (grey lines plus symbols). The linewidths at $T = 3.5\,K$ (blue triangles) and at $T = 12\,K$ (red circles) were remeasured, leading to the final values displayed in Fig. 3.8.*

and the superconducting state measured by NRSE (see paragraph 3.5) were added to the dispersion data at $T = 3.5\,$K, so that dispersion values for $T = 12\,$K are obtained. As mentioned before, this does not change the values by more than $0.1\,$meV.

Aynajian et al. observed that the dip in the normal state dispersion is accompanied by a peak in the linewidth at $\xi = 0.17 \pm 0.01$ r.l.u., which corresponds to a normal state phonon energy of 3.21 ± 0.15 meV. Though the dip in the dispersion is stretched, the position where the slope is minimal is in fact right there, namely at $\xi = 0.165$ r.l.u. (see Fig. 3.5b). It is immediately apparent from Fig. 3.4b that the DFT calculations for the linewidths do not capture the Kohn anomaly. DFT calculations in general do capture Kohn anomalies, and similar calculations for the longitudinal phonons in Pb proved that the absence of the anomaly is not due to poor Fermi surface sampling.

The polarization decay profiles that were measured with the purpose of detecting a lineshape distortion (to be presented in section 3.4.1) brought to light a smaller normal state linewidth value for $\xi = 0.18$. Since the existence of the anomaly was called into question by this, the linewidths from 0.09 up to 0.21 r.l.u. were remeasured in a single run. The new set of phonon linewidths at $T = 12\,$K and $T = 4\,$K is shown in Fig. 3.6. The same [110]-oriented sample with mosaicity $\eta = 4.8'$ was used as previously. The sample was denoted "Nb-I" in Aynajian's PhD thesis [20], where details can be found. The transition temperature was checked before the new measurements and found to be the same. The new measurements were performed using a horizontally flat Heusler analyzer instead of the PG(002) analyzer and bender that were previously used. The same incident neutron wavevector $k_I = 2.51\,$Å^{-1} was adopted. The linewidths of Fig. 3.4b were measured in several individual experiments, the most comprehensive of which was carried out in April 2006. This run was re-evaluated using the same dispersion curvature correction as for the new data to allow for direct comparison. In both cases, the linewidths were determined by fitting the exponential polarization decay profiles in the superconducting and normal state with shared initial polarization P_0. The values obtained this way for the previous experiment (Fig. 3.6, left-hand side) are within the error bars of the analysis of Aynajian shown in Fig. 3.4, as is to be expected.

The differences between the $T = 12\,$K and $T = 4\,$K data agree well between the runs. However, there is a smaller rise in linewidths for larger wavevectors in the new run. In particular, the value at 0.18 r.l.u. is lower than previously reported, just as in the experiment with the purpose of detecting a lineshape distortion. When looking for a potential cause of differences between runs, a possible rotation of the sample in the scattering plane over a multiple of 90° could be considered. Since the cylindrical sample is tilted by ca. 21.3° with respect to the vertical plane, it is not rotationally invariant. However, the Popovici method of instrumental resolution calculation does not predict a large influence, and neither does the second-order NRSE theory by Habicht and Keller [45].

Fig. 3.7 provides a closer look at the normal state polarization decay profiles at $\xi = 0.17$ r.l.u. and at 0.18 r.l.u. The top graph shows previous data while the bottom graph shows new
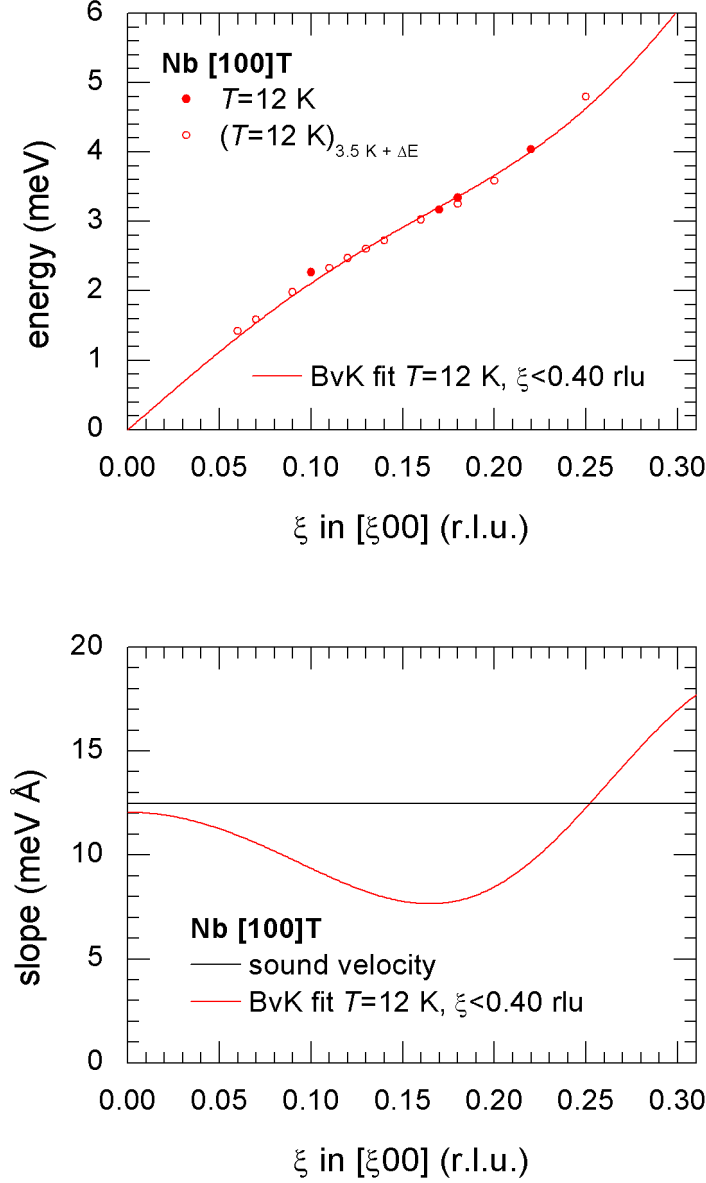
Figure 3.5.: *(top) Dispersion data of Nb $(00\xi)T$ at $T = 12\,K$ in the range of interest (solid symbols). The open symbols are values determined from triple-axis scans at $T = 3.5\,K$ to which the energy difference between the expectation values at $T = 3.5\,K$ and $T = 12\,K$ measured by* NRSE *were added (see paragraph 3.5). The Born-Von Kármán fit (solid line) to the data up to $0.40\,r.l.u.$ leaves residuals of less than $0.1\,meV$, which is of the same order as the uncertainty of the data. (bottom) Slope of the Born-Von Kármán fit. The slope is minimal at $\xi = 0.165$. In the long wavelength limit, the slope of the BvK fit converges with the velocity of sound that is derived from the elastic constants in Ref. [70] (constant line).*
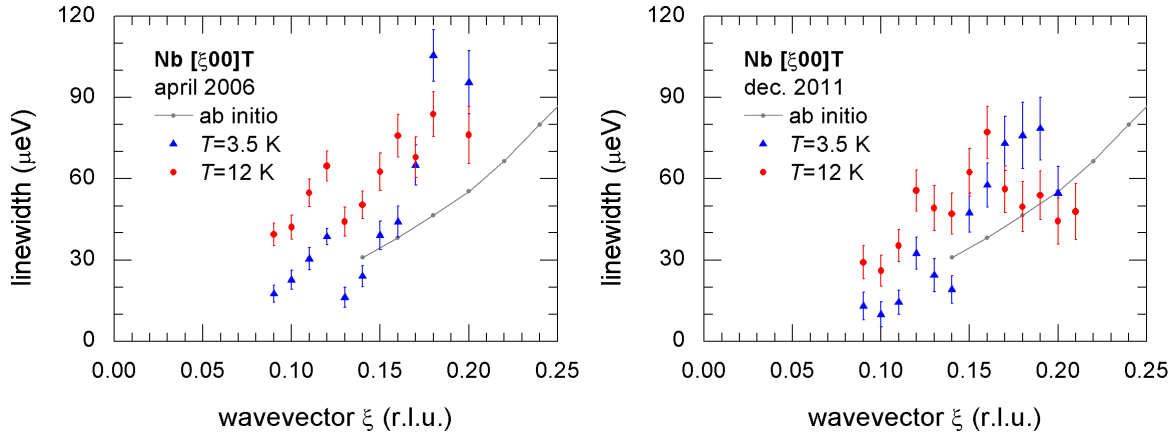
Figure 3.6.: *Comparison of linewidths measured at* TRISP *within single "runs" each, to perform a rigorous check of continuity. (left) Phonon linewidths from the most extensive of all previous experiments regarding the $(\xi 00)\,T$ branch in Nb, carried out in April 2006, evaluated in the exact same manner as the new data on the same sample (right).*

measurements. All polarizations are corrected for the respective instrumental effects, the respective direct beam polarization and the effects due to dispersion curvature and sample imperfections. Thus, ideally, the data should represent the same exponential curve with initial polarization $P_0 = 1$ and decay rate $\Gamma_n(\xi)$. One can see how especially the measurements with scan numbers $69**$ taken apart would lead to a larger linewidth than the other data. These correspond to the April 2006 experiment. However, other than an unverified variance when the sample is rotated by a multiple of 90°, there is no reason to assume that the linewidths were indeed inherently larger during this experiment. Any time-related change of the sample can be excluded, given the other previous experiments with scan numbers $58**$ and $125**$. It can thus be reasoned that the discrepancy is due to statistics. The exponential decay fit of the entire data batch together would give $\Gamma_n = 60.0(30)\,\mu\text{eV}$ for $\xi = 0.17$ and $\Gamma_n = 61.7(38)\,\mu\text{eV}$ for $\xi = 0.18$. It is preferable though to unite the results at a less basic level, as there might be differences in the effective polarization that are not accounted for that would become lost in a shared fit, e.g. a direct beam polarization which differs somewhat from the reference value. Hence the statistical average of the two experiments shown in Fig. 3.6 is taken. Solitary data from other experiments are not used in this union to avoid systematic errors sneaking in.

In Fig. 3.8, the combined set of phonon linewidths is shown. For wavevectors where no combined data are available, either data from one of the two experiments or solitary data from other experiments are shown (open symbols). While the linewidths at 0.18 and 0.20 r.l.u. are revised to lower values, the high value at $\xi = 0.16$ is affirmed. Hence the Kohn anomaly is less distinct than before and its position amended to the slightly lower value of 0.16 r.l.u. Moreover, a new trend can be discovered: at 0.12 r.l.u., there is a peak in the normal state data that does not disappear in the superconducting state. The
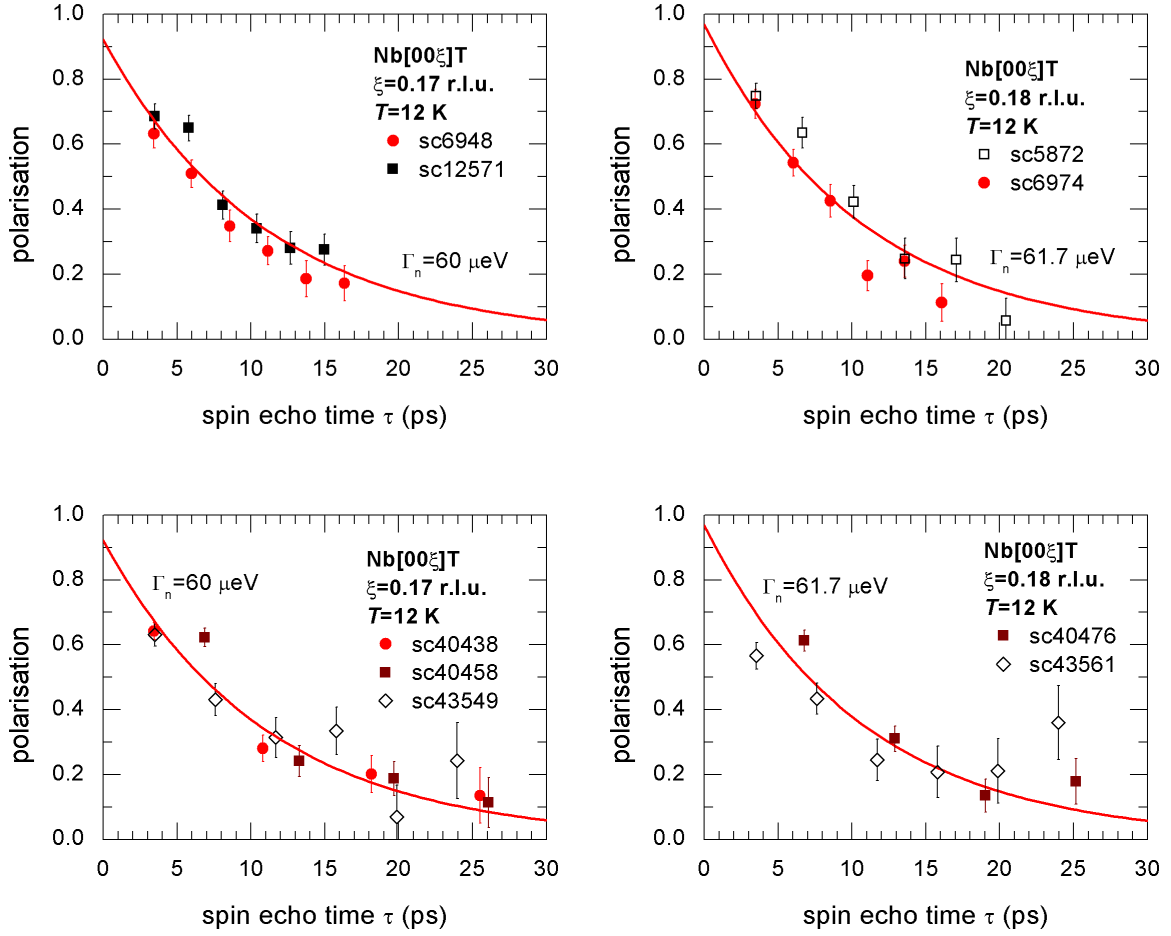
Figure 3.7.: *Comparison of all normal state* NRSE *data of Nb* [0,0,0.17] *T (left hand side) and* [0,0,0.18] *T (right hand side), taken at T = 12 K. The top graphs show previous data while the bottom graphs show new measurements. All polarizations were corrected for the respective instrumental effects, dispersion curvature effects and sample imperfections. For ξ = 0.17, the simultaneous exponential decay fit of both previous and recent runs gives* $\Gamma_n = 60.0(30)$ *μeV, and for ξ = 0.18* $\Gamma_n = 61.7(38)$ *μeV was obtained.*

phonon energy 2.45 meV is well below the superconducting gap $2\Delta(T = 3.5\,\text{K})$ and thus zero linewidth would be expected. The values at the two temperatures each stem from two individual data sets which are consistent with each other. Thus it is unlikely to be a statistical spike. Scattering from the sample holder can be excluded since the scattering angle is not close to the Bragg angle of aluminum. Spurious scattering from the cryostat would be a possibility if it were not for the consistent average count rate for progressive positions on the phonon branch. Interestingly, despite the structure in the absolute data, the difference between the normal and superconducting state linewidths is quite monotone (Fig. 3.8b). A possibility for spontaneous phonon decay as found in Pb can be excluded

too. There, the phonon velocity exceeds the velocity of sound before it falls below. This makes spontaneous 3-phonon decay possible, where a phonon decays into two phonons with the same direction into reciprocal space. This is clearly not the case though in Nb, as is explicitly demonstrated in Fig. 3.5b.

Summarizing, the *ab initio* calculations do not capture the peak in the linewidth data. The shrinking of the observed peak after subsequent measurements were taken into account may raise doubt if there is a Kohn anomaly at all. That is to say: is there a topological disposition to Fermi surface nesting at this wavevector, and is it coupled to the transverse branch? Or is the dip in the phonon dispersion a consequence of Born-Von Kàrmàn oscillations, due to general (quasi-isotropic) electron excitations? Since the phonon lineshape distortion to be studied in the superconducting state is in the same wavevector region as the anomaly, it is important to ascertain that the anomaly is indeed of electronic origin as anticipated.

3.2.2. The nature of the normal state anomaly at the superconducting gap edge

Recent *ab initio* electronic structure calculations on the group-V transition metals do provide strong indications that the anomaly is indeed of Kohn nature [71, 72]. They were carried out to answer the longer standing question of the anomalous T_c and sound velocity measurements in Nb, Ta and V under pressure [73]. The transition temperature decreases suddenly at a pressure of ~ 60 GPa in Nb, which falls together with a softening in the shear elastic constant c_{44}. The elastic modulus is connected to the initial velocity of the transverse phonons in [100] direction via the material density, $c_{44} = \rho v_T^2$. Albeit rather indirectly, the softening of the elastic constant is thus a witness to the anomalous curvature of Nb moving closer to the origin.

The effect can be explained by the fact that the Fermi sea rises under pressure, so that nesting vectors change accordingly. If the dip in the dispersion is due to a Fermi surface nesting vector which spans a hole-filled area and thus gets smaller with pressure, the shear elastic constant would get smaller, too. This is indeed found to be the case, not only for Nb, but also for V and Ta, which are in the same group of the periodic system of elements. The latter materials also show dips in the [001]T phonon dispersion. Similarly in V at ~ 200 GPa there is an instability. In Fig. 3.9a, the partial $(3^{rd} - 3^{rd}$ intraband transition) electron susceptibility χ of V, Nb, and Ta, calculated along $\Gamma - H$, which corresponds to the crystallographic direction [001], are shown at ambient pressure. The loci of the indicated maxima correspond to the observed anomalies in the respective materials, which on itself already means there is a clear-cut link between nesting vectors and dispersion. The maxima in χ indeed move towards Γ with increasing pressure, until they cause a martensic transition as the nesting vector gets zero and the Fermi surface parts touch the Brillouin zone boundary.
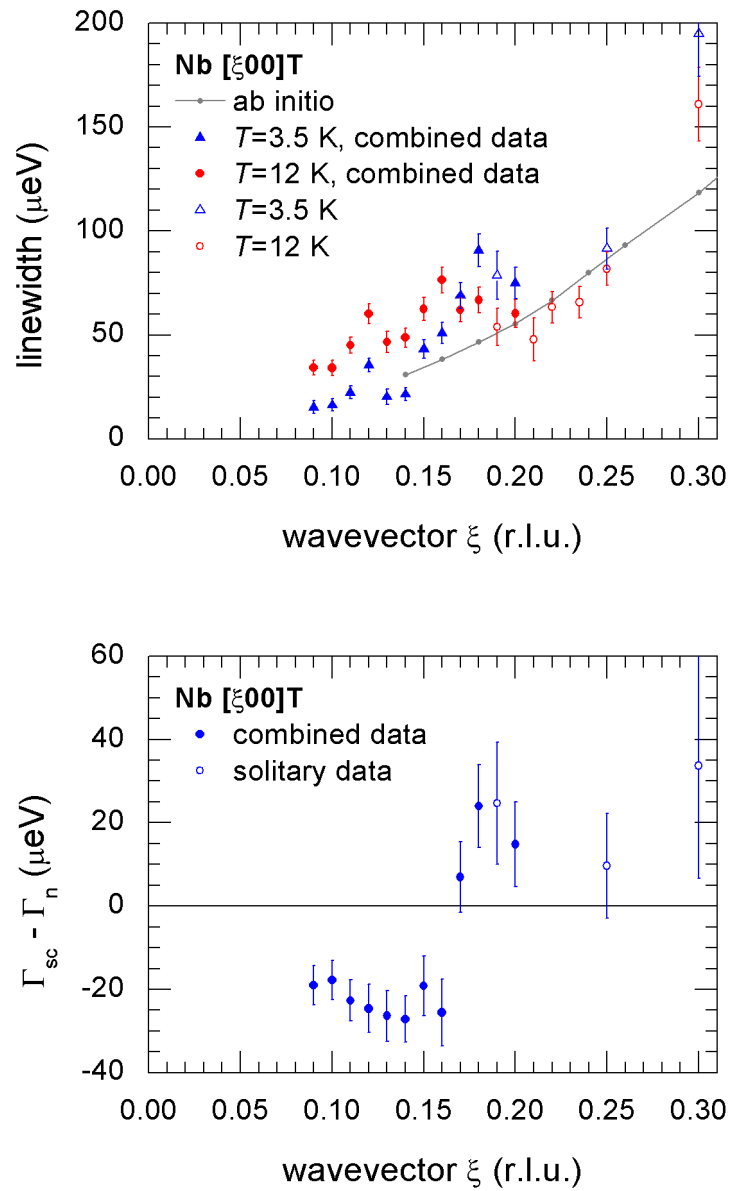
Figure 3.8.: *(top) Final linewidths at $T = 4$ and $12\,K$ for Nb $[001]\,T$, combining the data shown in Fig. 3.6 in a statistical average (closed symbols) and adding solitary data wherever combined data is unavailable (open symbols). (bottom) Difference between the normal and superconducting state linewidths.*
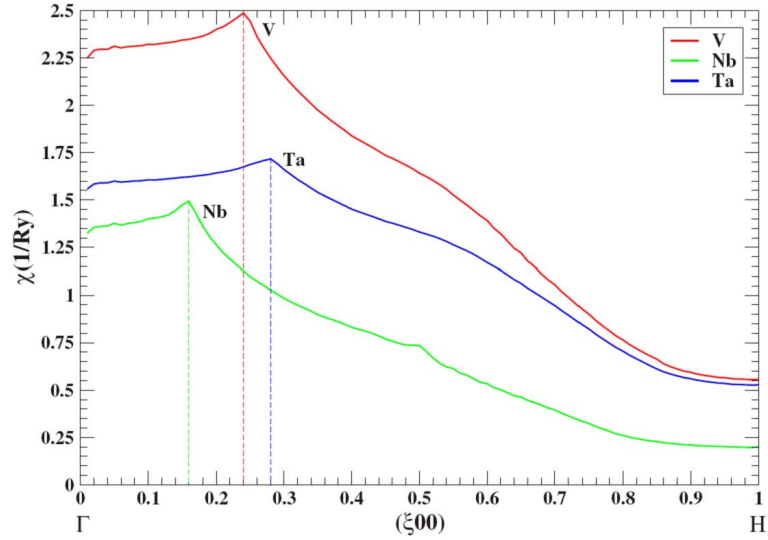
(a)
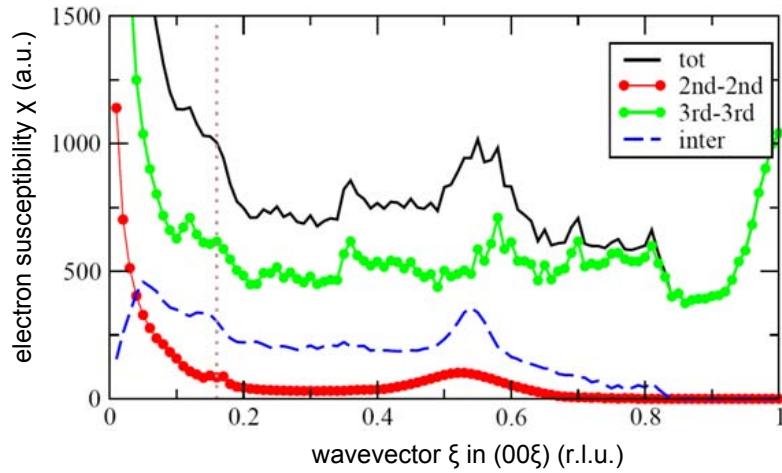
(b)

Figure 3.9.: *(a) Partial (third→third intraband transition) electron susceptibility of V, Nb, and Ta calculated along the $\Gamma - H$ direction. The indicated maxima correspond to observed anomalies in the $[100]\,T$ phonon branches of the respective materials. From Landa et al. [72]. (b) Partial and total electron susceptibilities of Nb calculated along the $\Gamma - H$ direction by L. Boeri [74]. Note that the rise at small wavevectors is markedly different from the behavior in (a). The increase of nesting phase space at $\xi = 0.16$ is again there, though not that pronounced.*
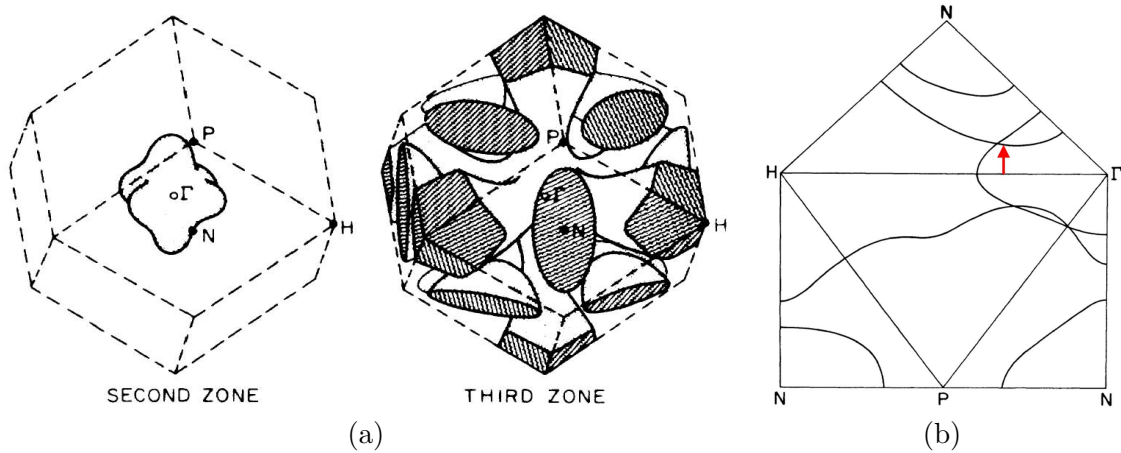
Figure 3.10.: *Three-dimensional Fermi surface sheets (left) in the bcc Brillouin zone in Nb and contours (right) in the symmetry planes. The arrow corresponds to half of the nesting vector responsible for the Kohn anomaly under consideration, $\mathbf{q_{KA}}/2$. From Ref. [75] after Ref. [59].*

The arrow in the Fermi surface diagram of Fig. 3.10b gives the nesting vector position. The Fermi surface in Nb consists of a $\Gamma-$centered hole octahedron in the second zone, as drawn in Fig. 3.10, far left. In the third zone, there are hole-filled $N-$centered distorted ellipsoids and there is an open hole surface along the [100] directions called "jungle gym". The arrow in Fig. 3.10b corresponds to half of the nesting vector. It spans the arms of the jungle gym surface, approximately at one third of the $\Gamma - H$ distance, rectangular to it. The plane formed by $\Gamma - H - N$ is the [001] plane. The three-dimensional shape of the Fermi surface around the nesting vector resembles an hourglass figure with a nearly square cross-section at its smallest point, and a diamond cross-section at the broader parts [59, 75]. The Kohn anomaly associated with this nesting vector is indeed negative: the nesting vector spans a hole-filled area.

From diagnosing the Fermi surface, one can see that the nesting function for the intraband transitions should in fact diverge at small wavevectors, and not go to a finite number as in Fig. 3.9a. The partial and total electron susceptibilities along $\Gamma - H$ calculated by L. Boeri describe this behavior correctly [74]. Moreover the verifiable partial nesting of the second Brillouin zone band increases confidence in these results. As the data are a bit "spiky", the identification of a peak at 0.16 in both bands, as well as a smaller shoulder at 0.12 r.l.u. in the $3^{rd} - 3^{rd}$ channel, are somewhat less conclusive.

In both nesting function figures, the position of the maximum in χ is at 0.16 r.l.u. The maximum of the phonon linewidth in Fig. 3.8a and the minimum of the dispersion slope agree precisely with this value. In contrast to these results, Johnston *et al.* [22], who identified the same nesting opportunity in their theoretical work, determined the vector to be 0.196 r.l.u. long. This is more in line with the value 0.21 r.l.u. obtained by early Hall measurements [76, 77] (see the comprehensive work of Mattheiss [59]).

When comparing Fig. 3.9b with the linewidth data, the coincidence between the peaks at 0.12 r.l.u. is eye-catching as well. It raises questions that are yet to be answered, especially if this is a Kohn anomaly as well. But if so, why does the linewidth not completely vanish in the superconducting state, as this phonon lies well below the energy gap?

3.3. Theoretical change upon entering the superconducting state

In paragraph 3.1.3, Allen's formulas for the self-energy renormalization in the superconducting state with respect to the normal state were introduced. Using the experimental data of the previous section, these formulas can be adopted for the case of Nb [001]T. The variables that are relevant for the calculation are:

- Temperature: the experiments were conducted at $T = 3.5\,\text{K}$, well below $T_c = 9.25\,\text{K}$.

- Dispersion: the Born-Von Kármán fit in Fig. 3.5 gives the normal state dispersion $\omega_{\mathbf{q}}$ at $T = 12\,\text{K}$, which will serve as the reference from which the renormalization is calculated. The residuals of the BvK-fit and the uncertainty of the data are of the order of $0.1\,\text{meV}$.

- The superconducting gap: the Clem formula gives a gap width at the experimental temperature of $3.5\,\text{K}$ that is as large as 98.8% of the saturated gap width. Judging from the dispersion energy at the sudden change in the linewidth difference in Fig. 3.8b, $2\Delta_{[100]} = 3.15\,\text{meV}$ is chosen, so that $2\Delta(T = 3.5\,\text{K}) = 3.11\,\text{meV}$. The phonon wavevector at this energy is $\xi_{2\Delta} = 0.163\,\text{r.l.u.}$ This will prove to be a good estimate once the detailed analysis is continued for the linewidths in the superconducting state around $\xi_{2\Delta}$. Though the *relative* determination of the values in the following will be rather precise, the *absolute* gap width can be pinpointed with no more accuracy than the triple-axis phonon energy data.

- The e-ph coupling strength: The electron-phonon interaction strength is contained in the normal-state parameter $r_{\mathbf{q}}$, which is defined as the ratio between the normal state linewidths and the phonon energy. As shown in Fig. 3.11, the shared experimental values of $\Gamma_{\text{n}}(\omega_{\mathbf{q}})$ at $T = 12\,\text{K}$ (Fig. 3.8a) are divided by the BvK-fit to the dispersion data at $T = 12\,\text{K}$. At 0.12 and at the position of the identified Kohn anomaly, $0.16\,\text{r.l.u.}$, narrow peaks can be distinguished, which were discussed in the previous section. Since the absolute values of the linewidth and therewith the structured variation in $r_{\mathbf{q}}$ dependent somewhat on the experimental run (compare Fig. 3.6), though, it makes little sense to follow this curve down to the last detail. Hence, a mean $r = 0.02$ is chosen. Disregarding the Kohn anomaly at the wavevector that
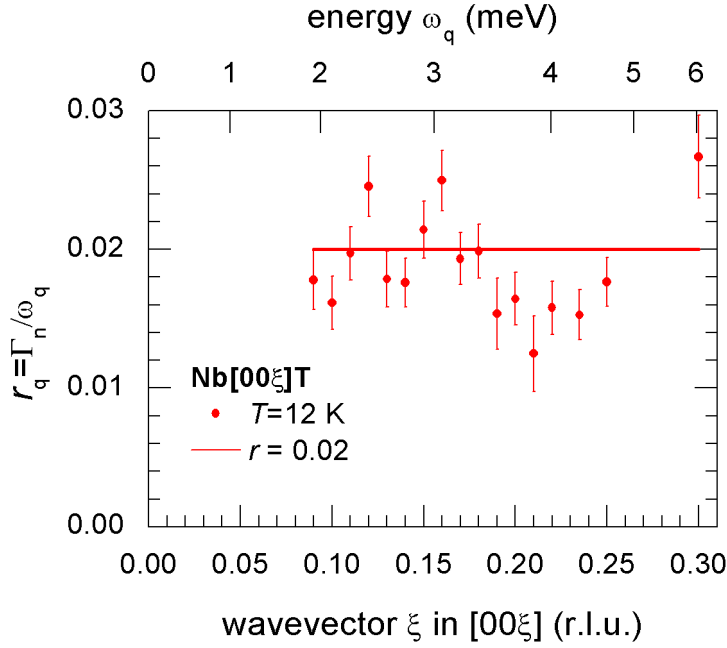
Figure 3.11.: *Parameter $r_{\mathbf{q}} = \Gamma_{\mathrm{n}}(\omega_{\mathbf{q}})/\omega_{\mathbf{q}}$ reflecting the strength of the electron-phonon coupling in the case of Nb[001] T. The combined linewidth data of all NRSE experiments and the BvK-fit to the dispersion data at $T = 12\,K$ are used to create the scattering data. The constant line represents the value $r = 0.02$ that is used for the calculations.*

corresponds to the gap edge $2\Delta_0$ means that the lineshape effect at the gap edge will in reality tend to be more pronounced than predicted in the following.

The difference in self-energy between the superconducting and the normal state is expressed in $\Gamma_{\mathrm{s}}/\Gamma_{\mathrm{n}}$ and in $\mathrm{Re}\,\delta\Pi/r_{\mathbf{q}}$, which are both functions of energy only, as given by Eq. 3.14 and 3.19, respectively. The linewidth ratio (shown in the top panel of Fig. 3.12) is virtually zero below the gap energy, which means there are hardly any thermally excited electrons at $T = 3.5\,\mathrm{K}$ that facilitate e-ph interaction. Above 2Δ, the e-ph coupling is increased due to the pile-up of density of electronic states around the gap edges. The curve looks slightly different from the figure in Allen's paper - not so much because of the temperature, but rather because the actual value of $2\Delta_0 = 3.952\,k_B T_c$ is used instead of the weak-coupling limit. Further, the dimensionless ratio $\mathrm{Re}\,\delta\Pi/\Gamma_{\mathrm{n}}$ is shown in Allen's paper for $\omega_{\mathbf{q}} = 2\Delta_0$, whereas here $\mathrm{Re}\,\delta\Pi/r$ is shown in units of $2\Delta_0$ (bottom panel), which means the two curves are essentially the same. Since the integrand of Eq. 3.19 converges slowly, an integration limit of $\omega/(2\Delta_0) = 1000$ is chosen. Negative values of the real part of the self-energy mean that the scattering function in the superconducting state is shifted towards lower energies compared to the normal state.

A colored map of the scattering function $S_{\mathrm{sc}}(\mathbf{q}, \omega)$ (according to Eq. 3.12) is depicted in Fig. 3.13, next to a map of the normal state function. Since the experimental $\mathbf{q}$-
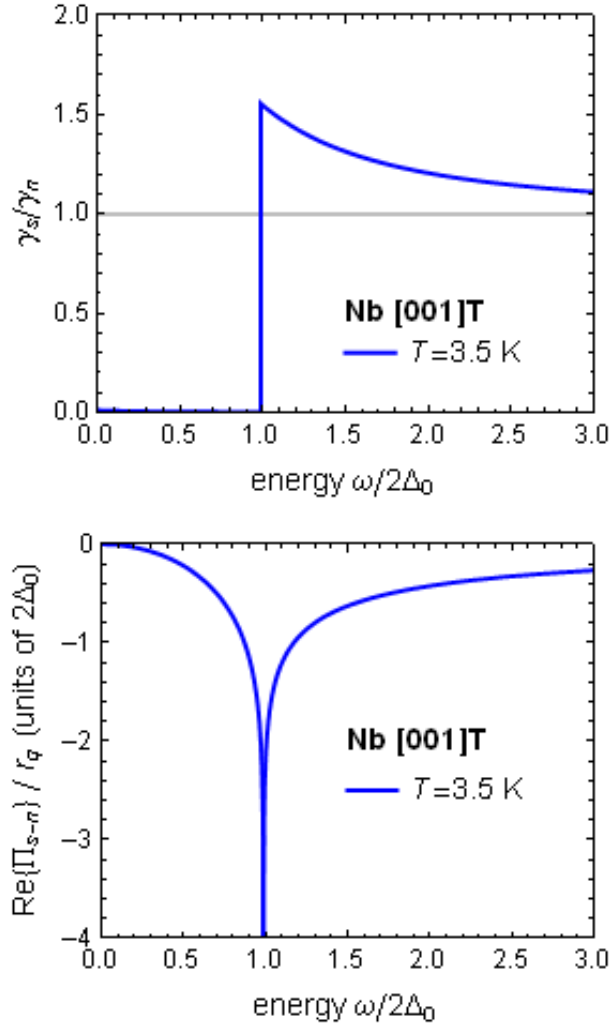
Figure 3.12.: *(a) Ratio of superconducting to normal values of the imaginary part of the self-energy for Nb[001]T at T = 3.5 K. (b) Difference between superconducting and normal values of the real part of the self-energy divided by the normal state parameter r. Negative values mean that the scattering function in the superconducting state is shifted to lower energies compared to the normal state.*

dependence of the parameter r is forsaken in favor of a clear depiction of the general trend, the normal state scattering function shown in the graph has the slowly varying energy width $\Gamma_n(\mathbf{q}) = r \cdot \omega_\mathbf{q}$ with $r = 0.02$. In the superconducting state, a clear border at $3.15\,\mathrm{meV}$ is created. The scattering function above this border is not as intense as in the normal state because of the linewidth broadening.

Fig. 3.14 shows several energy cuts through the scattering function maps. The resonance peak clearly withdraws weight from the remaining phonon, which is broken off abruptly at $2\Delta(T)$. Though the distances between the resonance and the remaining phonon diminish

(a)

(b)
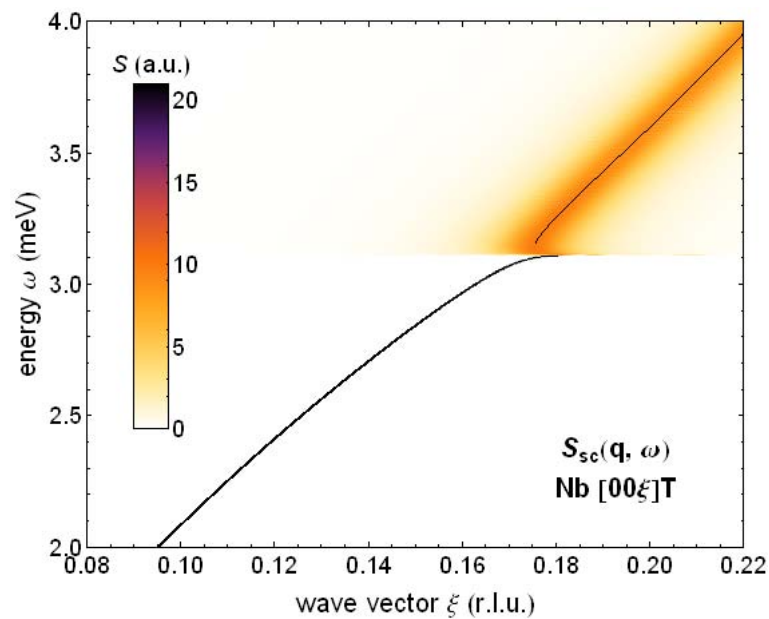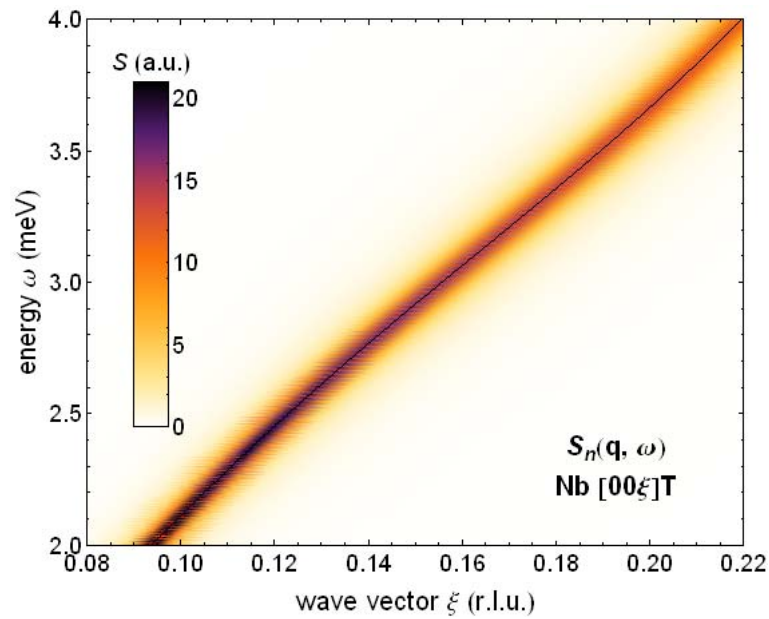
Figure 3.13.: *Map of the scattering function $S(\mathbf{q}, \omega)$ of the $Nb[00\xi]T$ phonon branch in the normal state at $T = 12\,K$ (top) and at $T = 3.5\,K$ (bottom). Thin black lines depict the nominal dispersion energy $\omega_{\mathbf{q}}$ (top panel) and the renormalized value in the superconducting state (bottom panel). The noise is an artifact of the graphic rendering.*

near the gap edge, the relative weight becomes comparable, so that the wavevector 0.17, just above $\xi_{2\Delta}$, displays the largest deviation from a single Lorentzian.

In Fig. 3.15, a few **characteristics of the resonance peak** below $2\Delta(T)$ are plotted. The energy position of the resonance peak, $\omega_{\mathrm{peak}}(\mathbf{q})$ (black line in Fig. 3.13b), is given by solving

$$\omega_{\mathrm{peak}}^2 - \omega_{\mathbf{q}}^2 - 2\omega_{\mathbf{q}}^2 r_{\mathbf{q}} \frac{\mathrm{Re}(\delta\Pi)}{\Gamma_{\mathrm{n}}}(\omega_{\mathbf{q}}, \omega_{\mathrm{peak}}) = 0 \tag{3.20}$$

numerically. The height of the resonance peak (Fig. 3.15a) is

$$S_{\mathrm{peak}} \equiv S(\omega_{\mathbf{q}}, \omega_{\mathrm{peak}}(\omega_{\mathbf{q}})) = \left[\omega_{\mathrm{peak}}(\omega_{\mathbf{q}}) \cdot r_{\mathbf{q}} \cdot \frac{\Gamma_{\mathrm{s}}}{\Gamma_{\mathrm{n}}}(\omega_{\mathrm{peak}}(\omega_{\mathbf{q}})) \right]^{-1}. \tag{3.21}$$

Though the height of the resonance peak below the energy gap edge is large even as ξ exceeds the wavevector that corresponds to the energy gap, $\xi_{2\Delta} = 0.163\,\mathrm{r.l.u.}$, its weight diminishes. This becomes apparent in panel (b), where the relative weight of the part of the spectral function below $2\Delta(T)$ is plotted. The total spectral weight is conserved when entering the superconducting state [25]. Since all spectral weight is downshifted, the transition of the phonon through the gap edge takes place at higher wavevectors than $\xi_{2\Delta}$, which is where the *normal state* dispersion $\omega_{\mathbf{q}}$ would be equal to the gap energy. This explains why the phonon splitting is in fact most obvious at $\xi = 0.171\,\mathrm{r.l.u.}$ ($\omega_{\mathbf{q}} = 3.23\,\mathrm{meV}$), where the relative areas of the resonance and the residual phonon part are exactly equal to each other.

3.4. Triple-axis resolution and polarization decay profiles

In the beginning of the chapter, it was stated that NRSE *measurements give access to the cosine Fourier transform of the spectral lineshape. In practice, the finite momentum resolution gives rise to second-order effects. These cannot be treated apart from the wavevector-dependent phonon lineshape distortion that is induced by superconductivity.*

Here, some basics of NRSE from chapter 2 are repeated and elaborated. Generally, the polarization measured by spin-echo is (Eq. 2.15)

$$< \sigma_x > = \frac{1}{2N} \int S(\mathbf{q}, \omega)\, T(\mathbf{k_i}, \mathbf{k_f})\, \exp[i\phi(\mathbf{k_i}, \mathbf{k_f})]\, \mathrm{d}^3 k_i\, \mathrm{d}^3 k_f + c.c.$$

where $S(\mathbf{q}, \omega)$ is the scattering function, T the transmission probability, and ϕ is the sum of Larmor precession angles before and after the sample. To be precise, the scattering function actually depends on the total momentum transfer $\mathbf{Q} = \mathbf{G_0} + \mathbf{q}$. For transverse phonons, the lattice vector $\mathbf{G_0}$ is chosen perpendicular to the phonon momentum $\mathbf{q}$. Specifically, for the measurements of the (001)T branch in Nb at low wavevectors, $\mathbf{G_0} = (110)$ is used. N is a normalization factor. The integration involves all incident neutron momenta $\mathbf{k_i}$
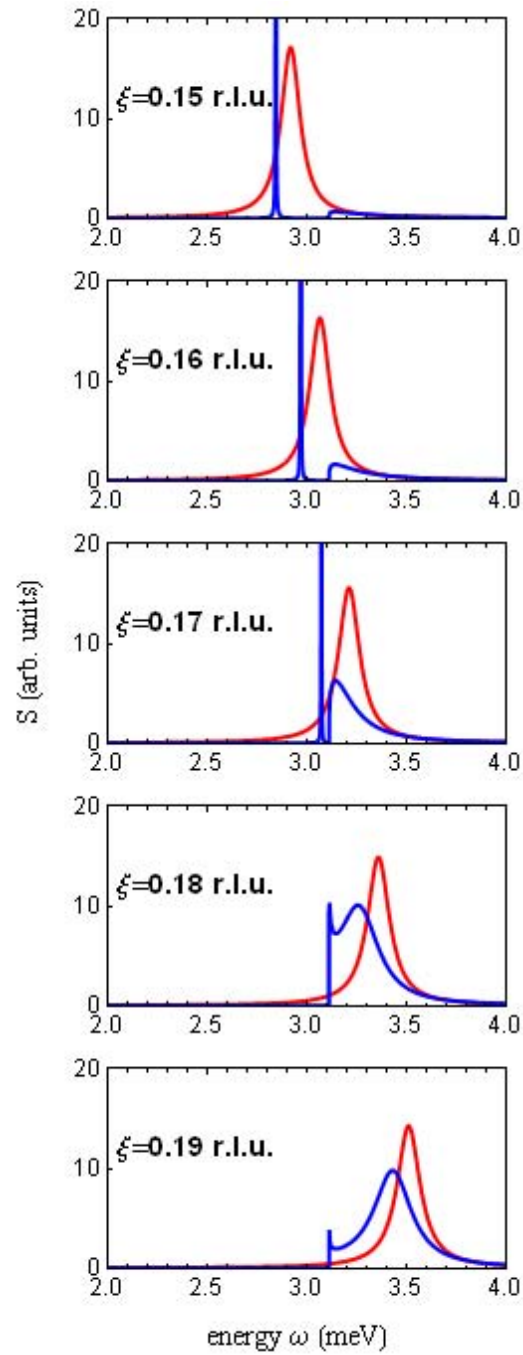
Figure 3.14.: *Spectral lineshapes in the normal state (red lines) and in the superconducting (blue lines) in $Nb[00\xi]\,T$ for $\xi = 0.15$ to 0.19.*
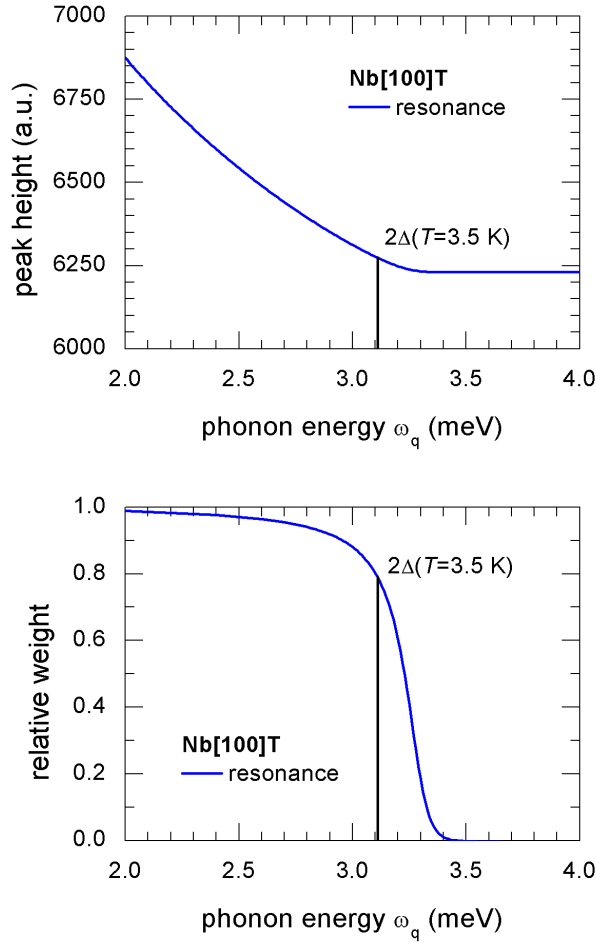
Figure 3.15.: *Height (a) and integrated area (b) of the resonance peak below $\omega = 2\Delta(T)$ at $T = 3.5$ K in the Nb $[00\xi]T$ phonon branch. The characteristics are plotted as a function of the normal state dispersion energy $\omega_{\mathbf{q}}$, which is an invertible function of ξ. The position where $\omega_{\mathbf{q}}$ equals 2Δ is indicated by black vertical lines.*

and scattered neutron momenta $\mathbf{k_f}$ around the pair of most probable wavevectors $(\mathbf{k_I}, \mathbf{k_F})$. By adding the complex conjugate, the polarization becomes real and proportional to the cosine of the Larmor precession angle.

The wavevectors are chosen in a way that the dispersion $\omega_0(\mathbf{q}) \equiv \omega_{\mathbf{q}}$ is illuminated around the central point $\omega_0(\mathbf{q_0})$. In the experiment, the tilt angles and the frequency ratio of the *rf*-coils are adjusted so that the spin-echo conditions are fulfilled (see chapter 2). In this case, the net Larmor precession phase is the same for neutrons that scatter from the center of the dispersion as well as neutrons that scatter from $(\mathbf{q}, \omega_0(\mathbf{q_0}) + \mathbf{C} \cdot (\mathbf{q} - \mathbf{q_0}))$, where $\mathbf{C}$ is the slope of the spin-echo surface in the direction of $\mathbf{q_0}$. The phase varies linearly with increasing distance $\Delta\omega$ from this surface. That is to say, the manifold of surfaces of constant net Larmor phase are in a good approximation planar and parallel to each other within the triple-axis instrumental resolution. Thus, for a single excitation mode
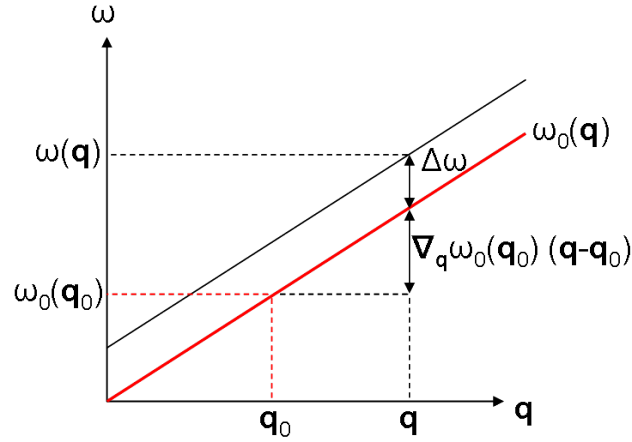
Figure 3.16.: *Schematic drawing clarifying the notations used to describe the phonon focusing effect: the scattering function at any point in $(\mathbf{q}, \omega)$ space can be described by the momentum relative to the central momentum $\mathbf{q_0}$ and the energy difference $\Delta\omega$ to the dispersion surface $\omega_0(\mathbf{q})$ (red line). The black line represents a surface of constant Larmor precession phase.*

with a plane dispersion, the spin-echo conditions are perfectly fulfilled if the slope of the surface matches the slope of the dispersion, $\mathbf{C} \stackrel{!}{=} \nabla_{\mathbf{q}}\,\omega_0(\mathbf{q_0})$ ("phonon focusing"). This case is visualized in Fig. 3.16.

The driving force behind the neutron spin precessions in the spectrometer arms is conveyed by the spin echo time τ. For neutrons that are scattered from the center $\omega_0(\mathbf{q})$ of the dispersion, the spin echo time does not have any influence. These neutrons arrive with the phase ϕ_0. Yet, the higher the spin echo time is, the more the final phase changes when a neutron loses an additional energy $\Delta\omega$ in the sample. Thus one can substitute ϕ in Eq. 2.15 for

$$\phi(\mathbf{k_i},\ \mathbf{k_f}) = \phi_0(\mathbf{k_I}, \mathbf{k_F}) - \tau \cdot \Delta\omega. \tag{3.22}$$

In the experiment, the spin echo time in the second spectrometer arm is varied, which leads to a cosine variation of the detected neutron intensity. While Eq. 2.15 gives the general polarization at any point of this scan, taking the "spin echo" means that the absolute value of the maximal polarization P is extracted from the scans. Thus instead of the real part of the complex function in Eq. 2.15, usually only the absolute value of the envelope is recorded. The factor $\exp(i\phi_0)$ drops out from the equation.

Using energy and momentum conservation, the integrals over the incident and scattered neutron energies can be recast into integrations over the respective momentum and energy loss [31, 46]. The transmission function then can be simply expressed in terms of the triple-axis resolution matrix $\mathbf{M}$ according to Popovici [38]. In this matrix notation, the four-component vector $\mathbf{X} = (\Delta\mathbf{Q},\ \Delta\omega + \mathbf{C} \cdot \Delta\mathbf{Q})$ is used with $\Delta\mathbf{Q} = \mathbf{Q} - \mathbf{Q_0}$. $\mathbf{Q_0}$ is the most probable total momentum transfer equivalently to $\mathbf{q_0}$. The basis of $\mathbf{Q_0}/|\mathbf{Q_0}|$ is

often used to express $\mathbf{M}$, with the second coordinate axis perpendicular to $\mathbf{Q_0}$ within the scattering plane. The polarization can then be written as (Eq. 2.17)

$$P = \frac{1}{N} | \iint S(\mathbf{Q_0} + \Delta\mathbf{Q} - \mathbf{G_0}, \omega_0(\mathbf{Q_0} + \Delta\mathbf{Q} - \mathbf{G_0}) + \Delta\omega) \, F(\Delta\mathbf{Q}, \Delta\omega) \, \mathrm{d}\Delta\omega \, \mathrm{d}^3\Delta\mathbf{Q}|$$

with the NRSE resolution function

$$F(\Delta\mathbf{Q}, \Delta\omega) = \exp(-i\Delta\omega\tau) \exp\left(-\frac{1}{2}\mathbf{X}^T\mathbf{M}\mathbf{X}\right). \tag{3.23}$$

We define the effective spectral function

$$\begin{aligned}
S_{\text{TAS}}\left(\omega_0(\mathbf{q_0}) + \Delta\omega\right) &= \sqrt{\frac{\det \mathbf{M_{RL}}}{(2\pi)^4}} \\
&\times \int \mathrm{d}^3\Delta\mathbf{q} \, \{S\left(\mathbf{q}, \omega_0(\mathbf{q_0}) + \mathbf{C}\Delta\mathbf{q} + \Delta\omega\right) \\
&\times \exp\left[-\frac{1}{2}\begin{pmatrix} \Delta\mathbf{q} \\ \Delta\omega + \mathbf{C}\Delta\mathbf{q} \end{pmatrix}^{\mathrm{T}} \cdot \mathbf{M_{RL}} \cdot \begin{pmatrix} \Delta\mathbf{q} \\ \Delta\omega + \mathbf{C}\Delta\mathbf{q} \end{pmatrix}\right]\}
\end{aligned} \tag{3.24}$$

so that the polarization is given by

$$P(\tau) = P_0 \, | \int S_{\text{TAS}}\left(\omega_0(\mathbf{q_0}) + \Delta\omega\right) \exp(-i\tau\Delta\omega) \, \mathrm{d}\Delta\omega|. \tag{3.25}$$

Care must be taken that the resolution matrix is rotated from the basis of $\mathbf{Q_0}$ into the basis of the reciprocal lattice, in which $\mathbf{q}$ is expressed,

$$\mathbf{M_{RL}} = \mathbf{R_{Q\to RL}}^{\mathrm{T}} \cdot \mathbf{M} \cdot \mathbf{R_{Q\to RL}}. \tag{3.26}$$

The effective spectral function is thus built up by integrating the triple-axis resolution times S along the spin echo surfaces, as illustrated in Fig. 3.17. Note that dispersion characteristics beyond the first order, such as curvature, are contained within this equation. Normally, one would go on to assume that the shape of the spectral function is independent of $\mathbf{q}$ within the triple-axis resolution. Further, the energy resolution would be taken to be much larger than the linewidth. Then S_{TAS} would reduce to S for a planar dispersion. However, since the spectral function changes shape swiftly at the superconducting gap edge, no such shortcut can be used.

3.4.1. Experiment

We continue to discuss the case for the experiment on niobium that is carried out with the aim of detecting the phonon lineshape distortion as described by the theory of Allen. In this experiment at TRISP, again the same sample of Nb is used as introduced in section 3.2. The final neutron momentum is fixed to $\mathbf{k}_F = 1.7\,\text{Å}$. A horizontally focusing
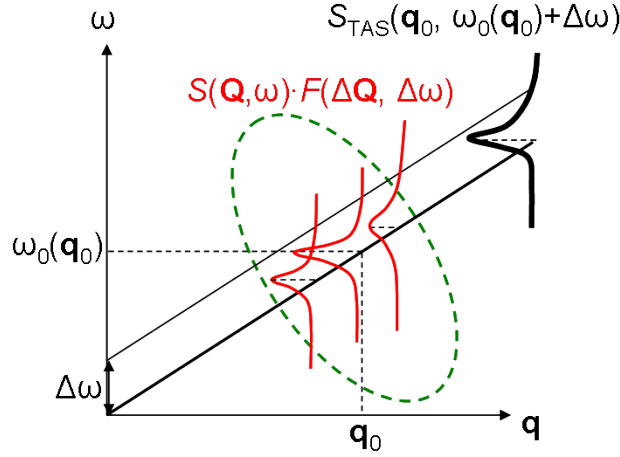
Figure 3.17.: *Schematic drawing illustrating the construction of the effective spectral function measured by NRSE, S_{TAS} (bold black curve). The absolute value of the NRSE resolution function F gives the triple-axis resolution (green dashed oval) around the central point $\omega_0(\mathbf{q}_0)$. $S_{\mathrm{TAS}}(\omega_0(\mathbf{q}_0) + \Delta\omega)$ is constructed by integrating $S(\mathbf{q}, \omega_0(\mathbf{q}))$ times the resolution (red curves) along the surface of constant spin-echo phase belonging to $\Delta\omega$) (black lines).*

Heusler analyzer with reciprocal radius $r_a = 0.3\,\mathrm{m}^{-1}$ is used. The TAS transmission probability distribution for this instrumental configuration at one exemplary position $\mathbf{Q_0} = (1,1,0.17)$, $\omega_0 = 3.21\,\mathrm{meV}$ is shown in Fig. 3.18. The ellipsoid describes the FWHM of the Gaussian resolution. As usual in spin-echo experiments, an anti-focusing configuration is chosen for the TAS resolution with respect to the phonon slope in order to minimize the effective $\mathbf{q}$-resolution. The red surface gives the normal state dispersion $\omega_{\mathbf{q}}$. The axis q_x points in the main phonon direction (001), q_y points in the reciprocal lattice direction (100) perpendicular to it. The smooth transition to other directions in reciprocal space is chosen so that it is consistent with off-symmetric dispersion data [20] and gradually crosses over to the dispersion in the {110} and {111} transverse branches. It must be noted that the curvature is less strong than the one used by Weber and Pintschovius in Ref. [26].

In the previous section it was demonstrated how, in the superconducting state, the phonon is split into a sharp resonance peak at the energy ω_{peak} and a residual phonon part above $2\Delta(T = 3.5\,\mathrm{K}) = 3.11\,\mathrm{meV}$. The position of the resonance peak is indicated by the blue surface in Fig. 3.18. As the phonon moves to higher energies, the peak becomes bound to the gap edge while losing weight quickly (*cf.* Fig. 3.15b).

More practicable are the cutouts of the resolution ellipsoid shown in Fig. 3.19. Apart from the cut-away view along the high symmetry axis of the phonon dispersion, one intersection crosses the scattering plane and the other lies perpendicular to it, which means these graphs are rotated by 45° with respect to the three-dimensional plot. Red lines again indicate the normal state dispersion, blue lines the resonance position ω_{peak} in the superconducting state. The lines of constant spin echo phase are shown for the
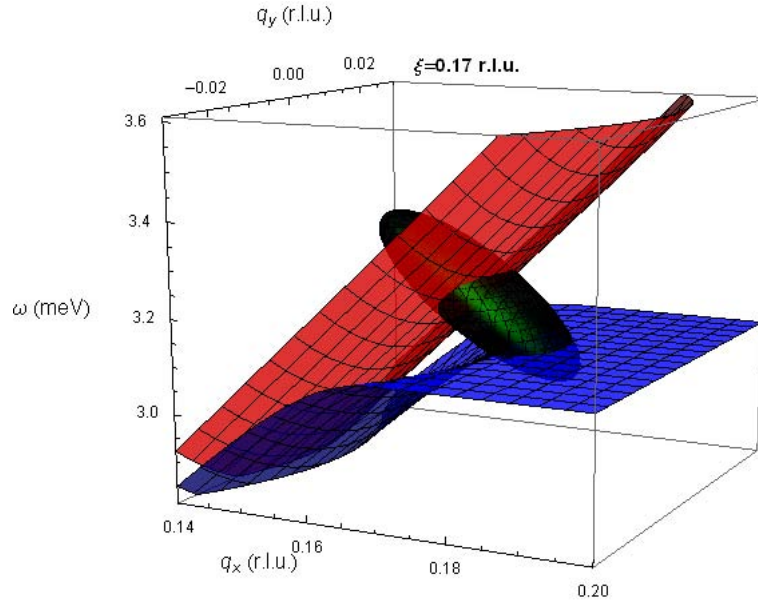
Figure 3.18.: *Visualization of the resolution at $\mathbf{Q_0} = (1,1,0.17)$, $\omega_0 = 3.21\,meV$ in Nb at TRISP, $\mathbf{k_F} = 1.7\,\AA$. The ellipsoid describes the FWHM of the gaussian resolution calculated using the Popovici method [38]. The red surface is the normal state dispersion while the blue surface gives the resonance peak position ω_{peak}. The axis q_x is in the main phonon direction (001), $q_y \parallel (100)$ perpendicular to it.*

arbitrary value of $\tau = 21\,$ps. The slope $\mathbf{C}$ of the spin echo surfaces is adapted to the normal state dispersion $\nabla_\mathbf{q}\,\omega_0(\mathbf{q_0})$. This means that the spin-echo is not ideally focussed in the superconducting state, neither for the resonance nor the residual phonon part above the gap. If the spin-echo conditions would be strongly violated for one of these two modes, then this would tend to create a constant background that would decrease the overall polarization. A mild violation of the spin-echo conditions for one of the two modes leads to a gaussian damping of the modulation [49]. The influence of the choice of spin-echo focusing is discussed later.

The shown curvature of ω_{peak} demonstrates that the sharpness of the resonance in the effective spectral function will be significantly affected by the finite $\mathbf{q}$-resolution. Though perpendicular to the main phonon direction, the curvature of the sharp peak is flattened compared to the normal state curvature, it folds strongly at the gap edge. Armed with this expectation, the effective spectral function and the resulting polarization for $\xi = 0.17$ and 0.18 are calculated according to Eq. 3.24 and 3.25, respectively. In the normal state just above T_c, the $\xi = 0.17$ and 0.18 correspond to nominal phonon energies of $3.24\,$meV and $3.44\,$meV, respectively. On the one hand, the dispersion curves upward away from the high-symmetry axis, so that the average illuminated phonon energy is slightly higher than the nominal energy. On the other hand, in the superconducting state, the energies are softened, so that these phonons cut the superconducting gap edge. The results are plotted in Fig. 3.20 and Fig. 3.21. In the top left panels, the pure scattering functions for
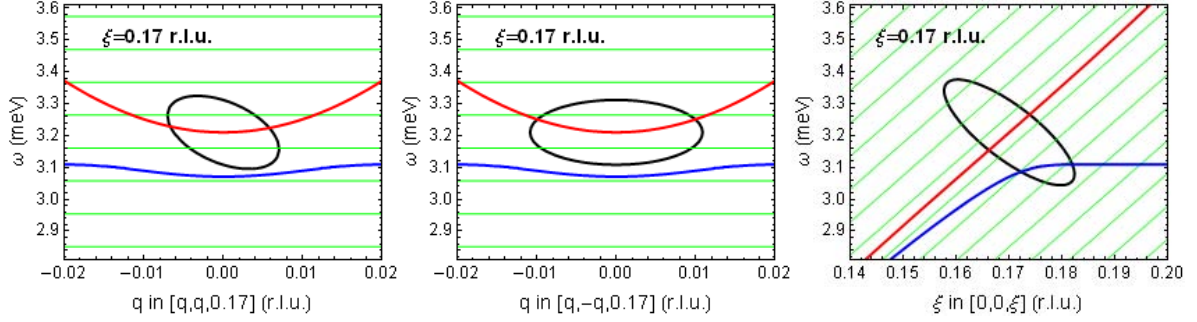
Figure 3.19.: *Cutouts of the resolution at $\xi = 0.17$ r.l.u. perpendicular to the phonon direction in the scattering plane (left), out-of-plane (middle) and parallel to the phonon direction (right). Red lines indicate the normal state dispersion, blue lines the resonance position ω_{peak} in the superconducting state. The lines of constant spin echo phase for $\tau = 21$ ps are shown in green.*

the normal and superconducting state shown in Fig. 3.14 are recapped. Next, the Fourier transforms of these pure functions,

$$P(\tau) = |\frac{\int_0^{10 \cdot 2\Delta} \mathrm{d}\omega S(\mathbf{q}, \omega) \mathrm{e}^{i(\omega - \mathrm{E}[S])\tau}}{\int_0^{10 \cdot 2\Delta} \mathrm{d}\omega S(\mathbf{q}, \omega)}|, \qquad (3.27)$$

are shown (top right panels). Though the expectation value of the spectral function $\mathrm{E}[S]$ technically must be included in the equation to form the spin-echo energy $\Delta\omega$, taking the absolute value in the end makes it redundant. The "real" spectral functions and polarization profiles, with the effect of the $\mathbf{q}$-resolution included, are shown in the bottom panels. The three-dimensional integration of Eq. 3.24 was in practice limited to the region $\pm 9\sigma_i$ with σ_i the gaussian width of the resolution intersection in each direction $i = q_{x,y,z}$. Mind that the depolarization decay caused by sample mosaicity is *not* included in the equation, but is still non-negligible. Under the assumption that the effects of the mosaicity can be described by a convolution with the effective scattering function, the Fourier transformations can be separated and the the decay due to mosaicity $P_M(\tau)$ is multiplied to the profiles seen here.

Conversely, the theoretical profiles may be divided by the calculated polarization decay caused by the normal state dispersion curvature in case of an infinitely small linewidth, $P_C(\tau)$, to compare them with the fully corrected polarization data. This gives the curves shown on the left-hand side of Fig. 3.22. The normal state polarization decay is almost exponential. The only difference is that $P_C(\tau)$ does not correct for the cut-off of the mode by the energy resolution - for that, one would have to have prior knowledge of the mode. Since the phonon spectral function is multiplied with a relatively broad gaussian energy resolution, the Fourier transform is a convolution with a small gaussian. Thus an initial "hovering" of the polarization value before its descent is a tell-tale sign that the mode width is in the range of the energy resolution. The normal state data (red circles) agree with the predicted decay within the error marge. It should be kept in mind though that
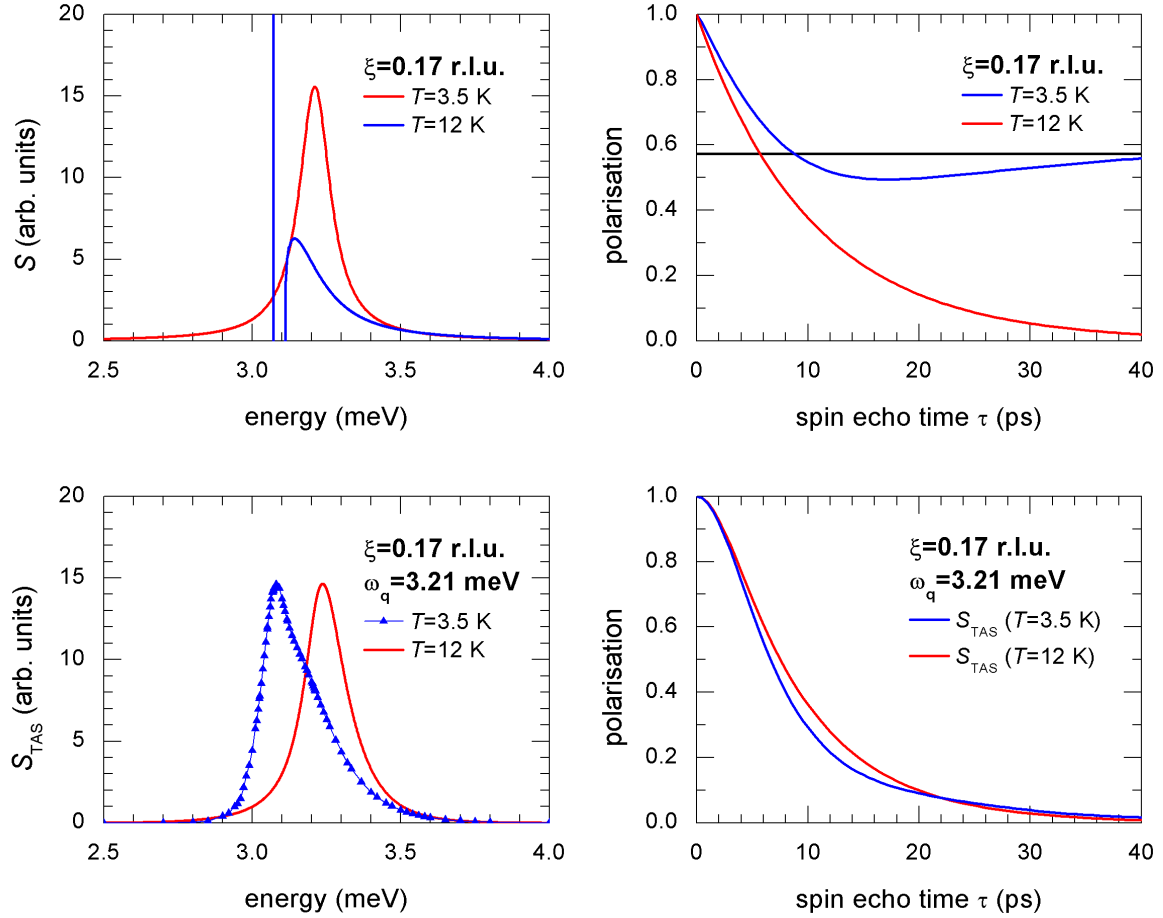
Figure 3.20.: *Top left: calculated scattering function $S(\mathbf{q}, \omega)$ in the normal state (red) and at $T = 3.5\,K$ (blue) in the $Nb[00\xi]T$ phonon branch at $\xi = 0.17$ r.l.u. Top right: absolute values of the Fourier transforms of the respe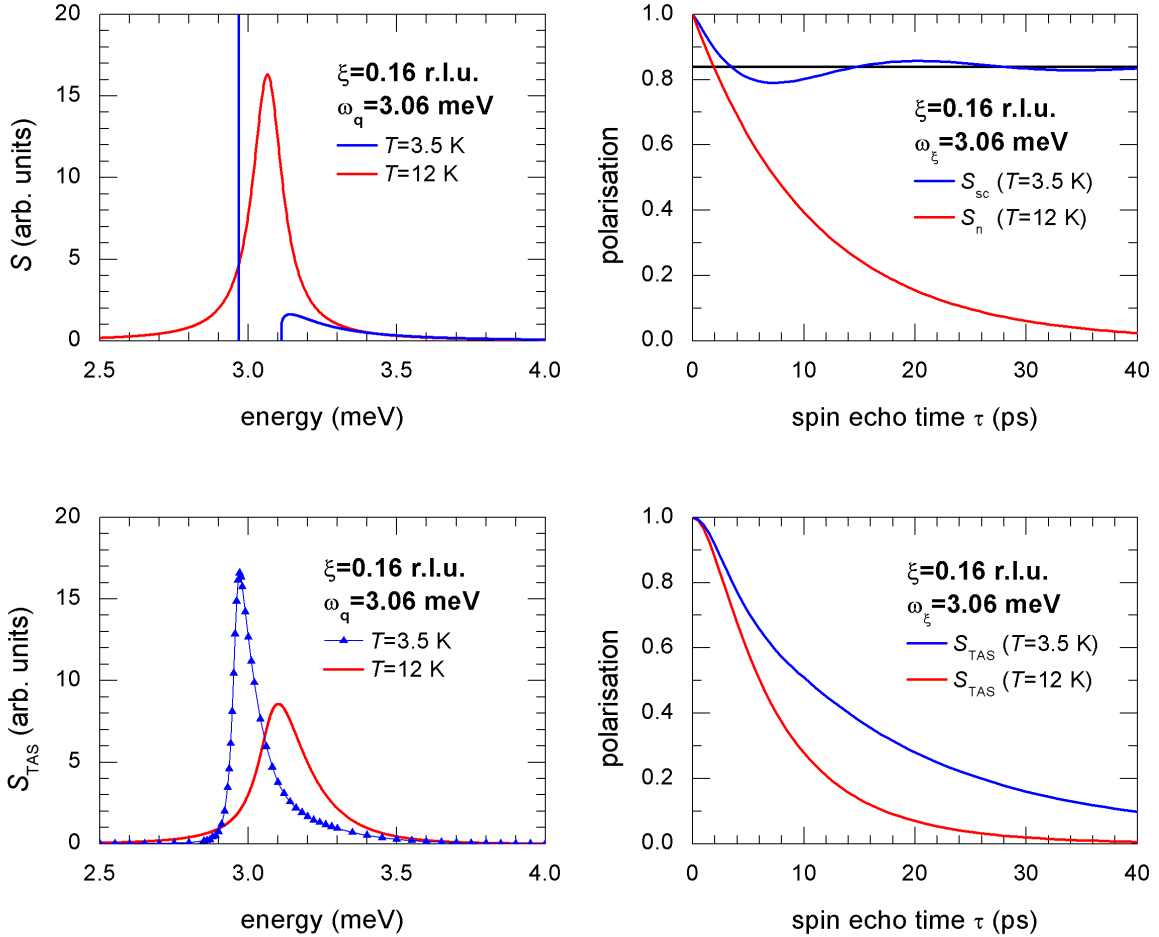ctive scattering functions. The polarization in the superconducting state converges to the value of the relative spectral weight below the gap (black line). Bottom left: effective spectral function in the normal state (red) and at $T = 3.5\,K$ (blue line plus symbols) after a convolution with the instrumental resolution of the $\mathbf{k}_F = 1.7\,\AA$-experiment. Bottom right: Fourier transform of the effective spectral functions.*

for the normal state linewidth, $\Gamma_n = r_\mathbf{q} \cdot \omega_\mathbf{q} = 0.02\,\omega_\mathbf{q}$ instead of the exact experimental value. Thus only the general trend is to be paid regard to, not the exact match of the decays even in the normal state. The data are however not refined enough to allow for a recognition of the lineshape distortion in the superconducting state.

Since the data shown in Fig. 3.22 depend strongly on the correction, the correction-independent ratios of the polarizations in the normal and superconducting state are shown on the right hand side. The influence of the choice of $r_\mathbf{q}$ is demonstrated in Fig. 3.23.
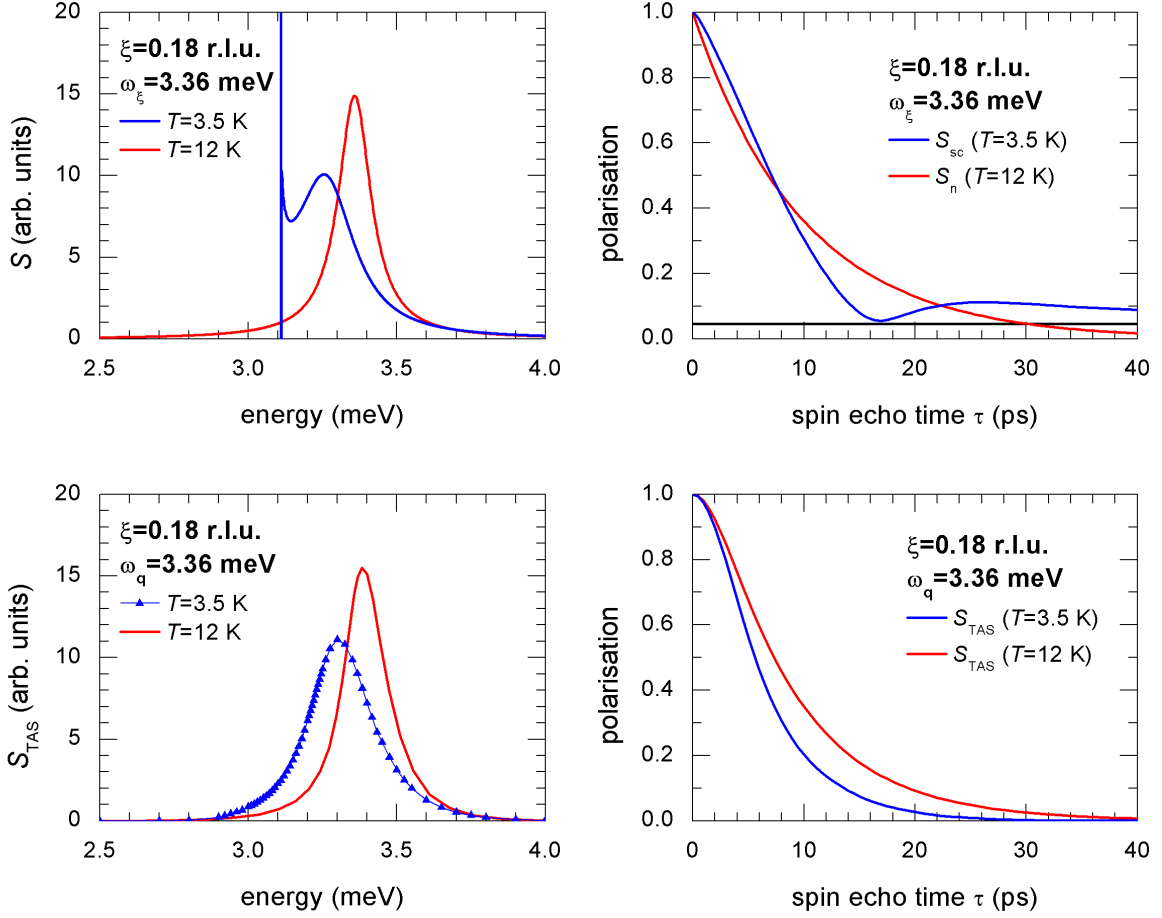
Figure 3.21.: *Same as in Fig. 3.20 for $\xi = 0.18$ r.l.u.*

Increasing r leads to more pronounced non-exponential decay of the polarization. In the figure both the exponential polarization and a non-exponential fit of this curve are shown.

Finally, we discuss why the non-Lorentzian lineshapes were not visible in previous spin-echo measurements. The reason is that a finite momentum resolution and a finite linewidth in the superconducting state smear out the differences. The influence of the finite **q**-resolution is illustrated in Figs. 3.24, 3.25 and 3.26. Fig. 3.24 shows the instrumental resolution ellipsoid for $\xi = 0.16$, slightly below $2\Delta_0$ in three **q**-directions together with the lines of constant spin-echo phase. It is obvious that the phase varies across the resolution ellipsoid due to the curved dispersion. This effect is shown in Fig. 3.25. The upper left panel shows the phonon in the normal conducting and the superconducting state assuming perfect momentum resolution (no resolution broadening), and the upper right panel shows the corresponding spin-echo curve. There is a clear difference between the decay profiles in the two states. The sharp excitation is dominant and leads to a nearly constant polarization. the broad part above 2Δ adds a small oscillation. The relative weights of these two
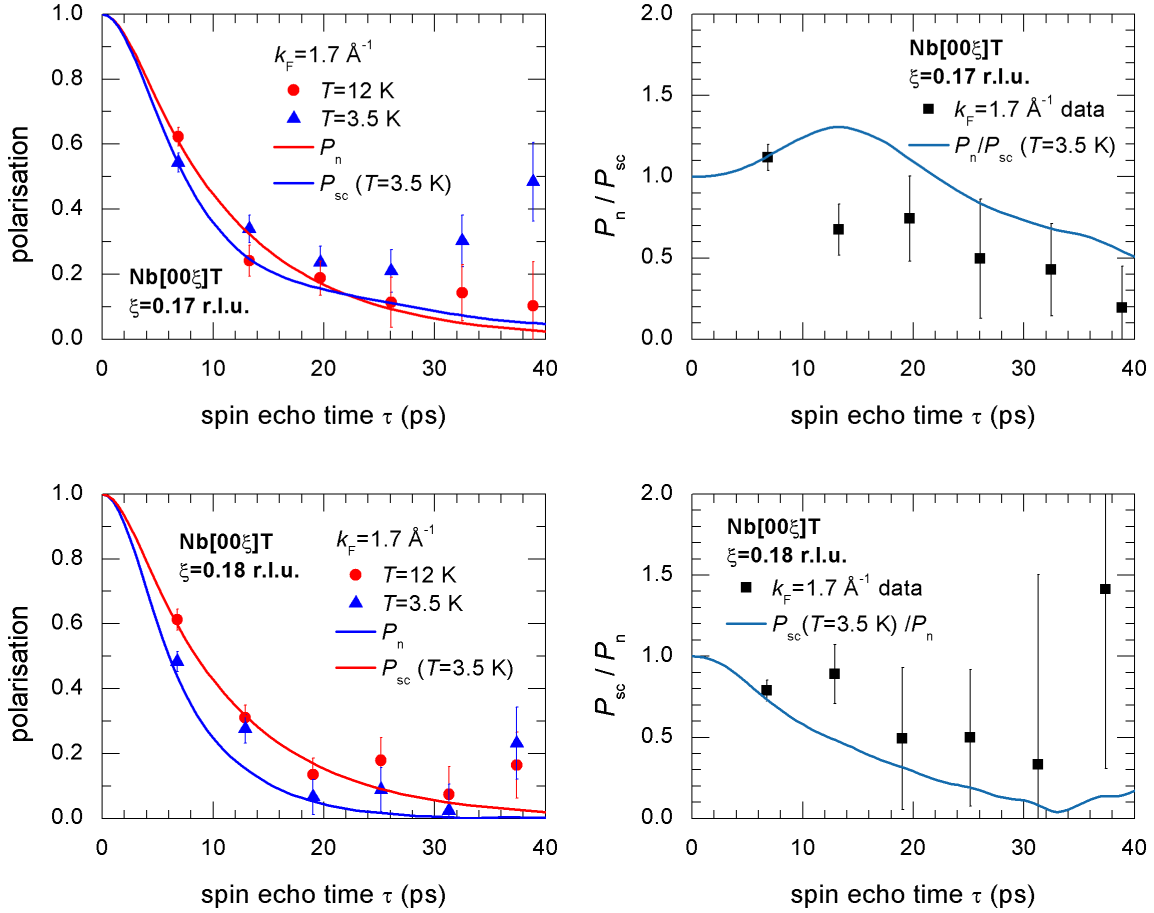
Figure 3.22.: *Experimental polarization decay data $P(\tau)$ corrected for instrumental resolution, normal state dispersion curvature and sample mosaicity in the $Nb[00\xi]T$ phonon branch at $\xi = 0.17$ (top) and 0.18 r.l.u. (bottom). The decay profiles at $T = 3.5\,K$ are compared to normal state profiles at $12\,K$. The data belong to the $\mathbf{k}_F = 1.7\,Å$ experiment. The theoretical polarization profiles from Figs. 3.20 and 3.21 are divided by the normal state dispersion curvature term $P_C(\tau)$ to give the curves above. The respective ratios between the normal and superconducting state polarizations (top panel) and the inverse value (bottom panel) are shown on the right hand side.*

contributions lower the polarization at higher τ to about 0.8. The situation changes dramatically when the finite momentum resolution is taken into account, as shown in the lower two panels of the figure. On the left side, the normal conducting state is broadened. In the superconducting state, the sharp excitation is also broadened and connected to the remainder above 2Δ. Although this line is also clearly non-Lorentzian, the difference to the Lorentzian line in the normal-conducting state in the spin-echo curve is not very pronounced (lower left panel) and only visible at higher τ-values, where the polarization is already quite low. Not included in these plots is the fact that the experimental linewidth in the superconducting state is not zero, even if the mentioned finite $\mathbf{q}$-resolution is corrected
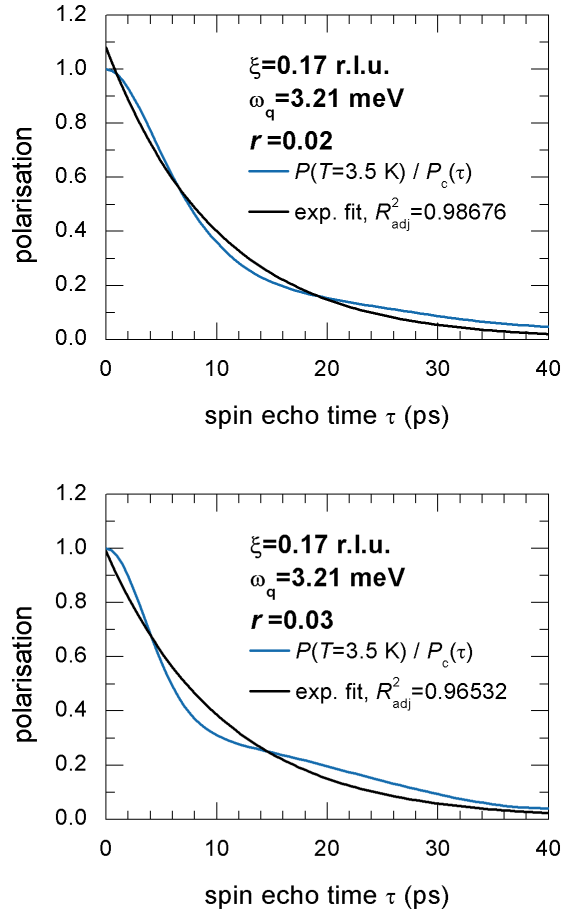
Figure 3.23.: *Polarization profiles at $\xi = 0.17 \, r.l.u.$ in the superconducting state for $r_{\mathbf{q}} = 0.02$ and 0.03, resp.*

for. This leads to an additional washing-out of the differences between the spin-echo curves. The experimental spin-echo data are compared with the spin-echo curves for $\xi = 0.16$, 0.17 and 0.18 r.l.u. in Fig. 3.26. On the left side, the experimental data and the calculated curves as shown in the previous figure are shown together. At the lowest $\xi = 0.16$, a large difference between superconducting and normal state is expected but not visible in the experimental data. The superconducting linewidth is much broader than predicted by the calculation. The reason is presently unknown, but might be related to lattice distortions or impurities. For higher ξ values the difference is expected to be small and can hardly be resolved with the given statistical error. On the right side, the ratio between normal and superconducting polarization is plotted. This ratio agrees well with the calculation (line). The small oscillations for the high τ-values are due to numerical noise in the calculations.

In Fig. 3.27 we discuss an alternative measurement mode. As in the superconducting state the resonance stays dispersionless at 2Δ, the idea is to focus on the resonance instead of the sloping normal state phonon. The left panels show N and sc state under these
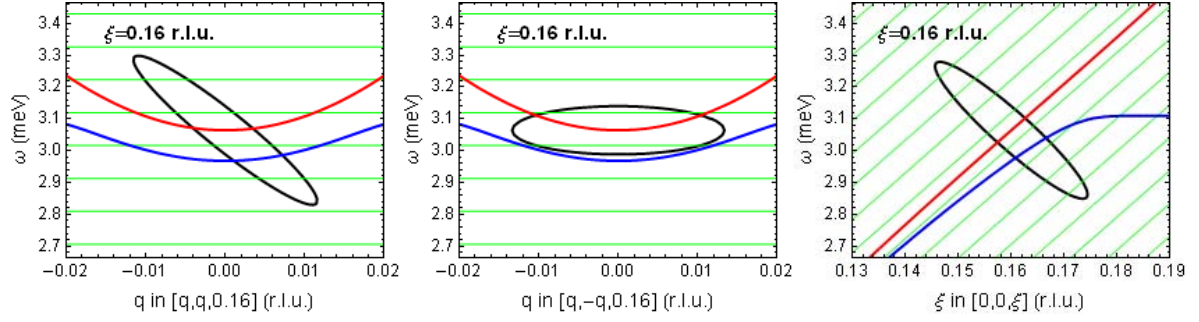
Figure 3.24.: *Cutouts of the resolution at $\xi = 0.16$ r.l.u. perpendicular to the phonon direction and in the scattering plane (left), out-of-plane (middle) and parallel to the phonon direction (right) as in the experiment carried out in April 2006. Red lines indicate the normal state dispersion, blue lines the resonance position in the superconducting state. The lines of constant spin echo phase for $\tau = 21$ ps are shown in green.*

conditions, the right panels show the corresponding spin-echo curves. This could be a useful measurement mode as the split mode effects are more pronounced.

Figure 3.25.: *Top left: calculated scattering function $S(\mathbf{q}, \omega)$ in the normal state (red) and at $T = 3.5\,K$ (blue) in the $Nb[00\xi]T$ phonon branch at $\xi = 0.16$ r.l.u. Top right: absolute values of the Fourier transforms of the respective scattering functions. The polarization in the superconducting state converges to the value of the relative spectral weight below the gap (black line). Bottom left: effective spectral function in the normal state (red) and at $T = 3.5\,K$ (blue line plus symbols) after a convolution with the instrumental resolution of the April 2006-experiment ($\mathbf{k}_I = 2.51\,\mathring{A}$). Bottom right: Fourier transform of the effective spectral functions.*
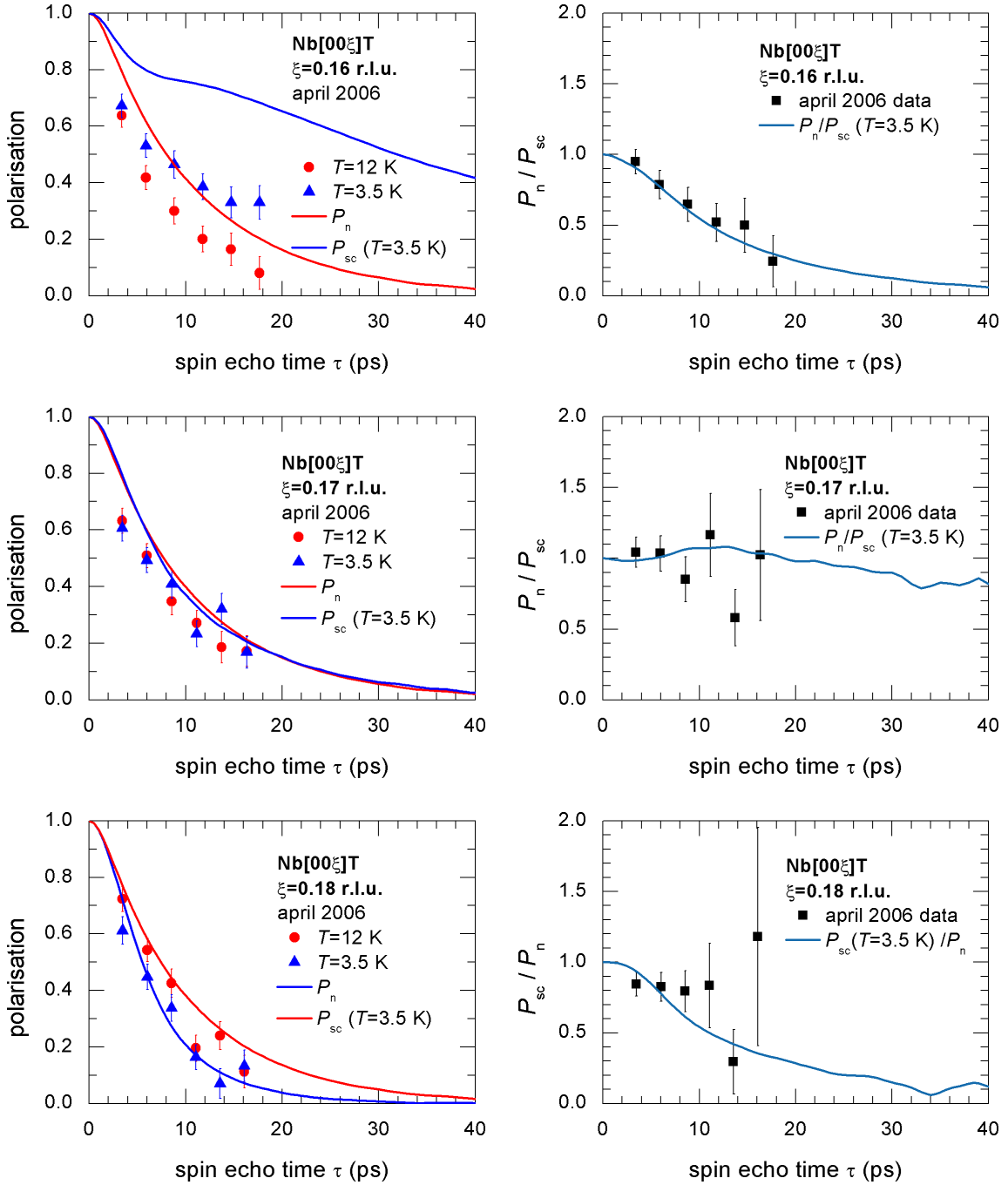
Figure 3.26.: *(left) Polarization decay $P(\tau)$ in the Nb $[00\xi]\,T$ phonon branch at $\xi = 0.16$ (top), $\xi = 0.17$ (middle) and $0.18\,r.l.u.$ (bottom). The data (symbols) belong to the April 2006 experiment, where $\mathbf{k}_I = 2.51\,\text{Å}$ and the $\text{PG}(002)$ analyzer were used. The theoretical profiles (curves) are divided by the normal state dispersion curvature term $P_C(\tau)$. (right) Ratio between the normal and SC state polarization for $\xi = 0.16$, $\xi = 0.17$ (top and middle) and inverse ratio for $\xi = 0.18$ (bottom).*
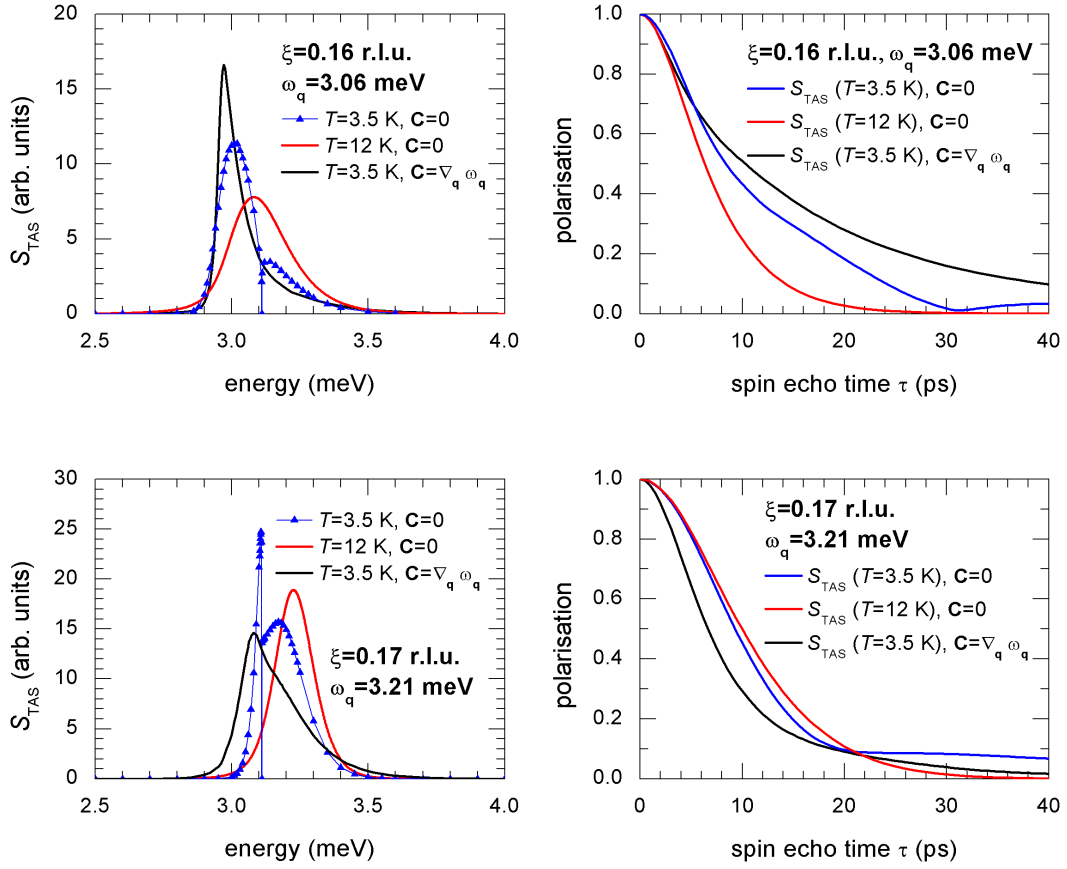
Figure 3.27.: *Effective spectral function (left) and polarization decay (right) at $\xi = 0.16$ and for a resolution that corresponds to the April 2006 experiment (top) and at $\xi = 0.17$ for a resolution that corresponds to the $\mathbf{k}_F = 1.7\,\mathring{A}^{-1}$ experiment (bottom) in case of a flat spin-echo surface.*

3.5. Linewidth ratios and energy shifts

In this section, we show in detail the measured linewidths and energy shifts and the related data analysis based on Allen's theory. In Fig. 3.28, the linewidths and energy shifts for Nb (001)T are shown. The linewidth renormalization is less pronounced than expected. The energy shift deviates from the simulated curve. The simulated curve does not converge with the non-resolution broadened curve for small ξ values, which is an artefact due to resolution effects and dispersion curvature.

The relative energy shift between two temperatures is directly proportional to the translation of the last rf-coil, ΔL, that is necessary to match the phases of the spin-echo signal:

$$\mathrm{E}[S_1(\omega)] - \mathrm{E}[S_2(\omega)] = -\frac{2\pi\hbar f_{\mathrm{eff},2}\Delta L}{\tau|\mathbf{v}_F|}. \tag{3.28}$$

If the last coil moves closer to the previous one ($\Delta L < 0$), it means that the neutrons got slower: they can perform the same number of Larmor precessions as before within a shorter flight path. Thus the energy loss is larger ($\Delta E > 0$). In the experiment, the condition is fulfilled that the phase shift is smaller than 2π and thus uniquely distinguishable. The spin echo time is determined by the same approximation of a planar dispersion for both temperatures. The energy shift that is measured in the case of a simple Lorentzian excitation which changes into a split excitation is to be understood as the energy difference between the respective center of gravity of each spectral function. This is evident since the beam average is measured; since the energy resolution of the transmission function is so large (and constant, since no instrumental changes are made between the measurements) the most probable neutron energy transfer is completely determined by the expected value of the energy for the particular spectral function.

In the next figure, we address the question of how the finite number of τ-points and the limited τ-range of the experiment affect the results. The upper panel simulates an experiment by taking spin-echo data over the range of typical $\tau_{min} \approx 3.7$ ps up to $\tau_{max} = 18$ ps and fitting these simulated data. The fitted value of P_0 shows a clear difference between sc and N states. The middle and the lower panel show these values for two experimental runs. In the experimental data no clear trend is visible due to the statistical error.

The next figure shows χ^2 values, again for a simulated experiment (top panel) and two corresponding experimental runs (lower panels). The top panel shows that close to the gap, χ^2 becomes large because the decay deviates from an exponential. This is again not really visible in the experimental data.

The next figures (Fig. 3.31, 3.32, 3.33 and 3.34) show the situation for $T = 0.8\,T_c = 7.4\,\mathrm{K}$, where the energy gap is $2\Delta = 2.24\,\mathrm{meV}$. The normal state phonon dispersion is equal to this value at $\xi_{2\Delta} = 0.107$ r.l.u. The elevated temperature broadens the resonance below
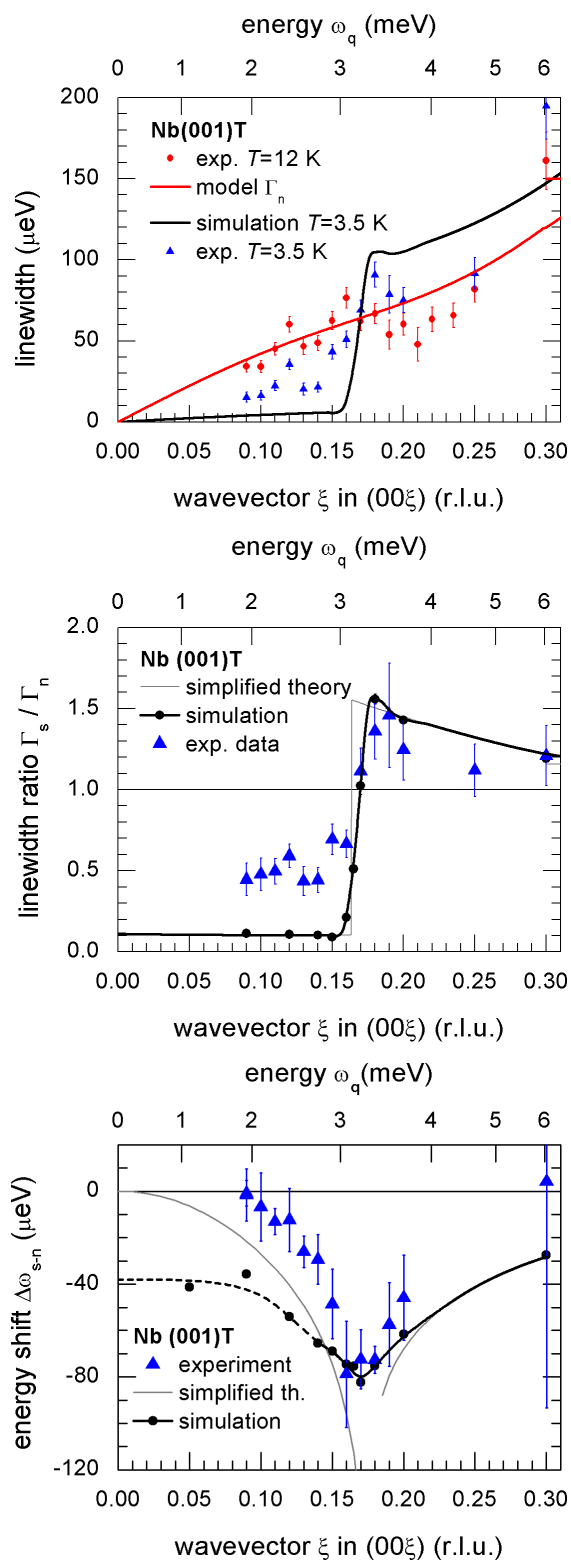
Figure 3.28.: *Experimental versus calculated energy shifts between the superconducting and the normal state in the Nb(001) T phonon branch.*
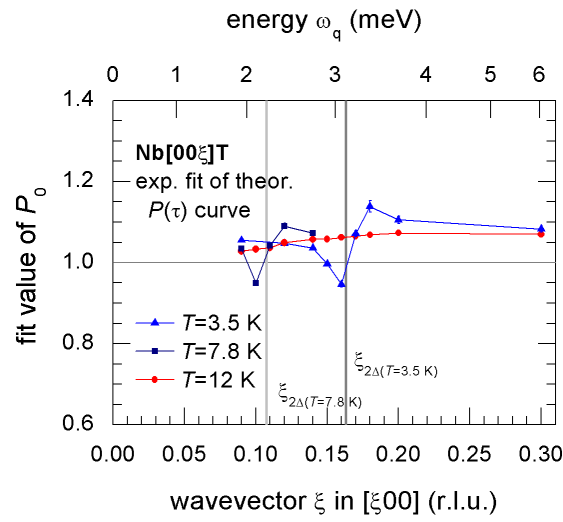
(a)
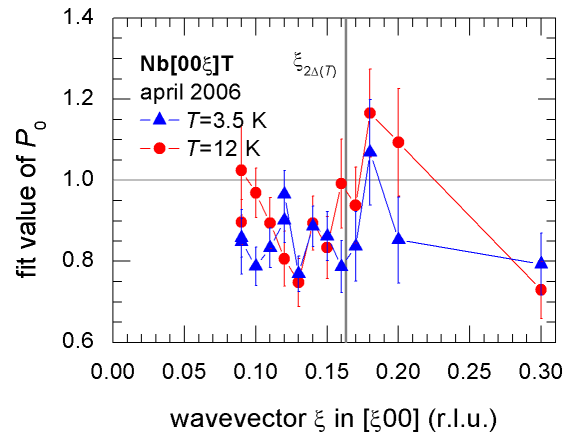
(b)
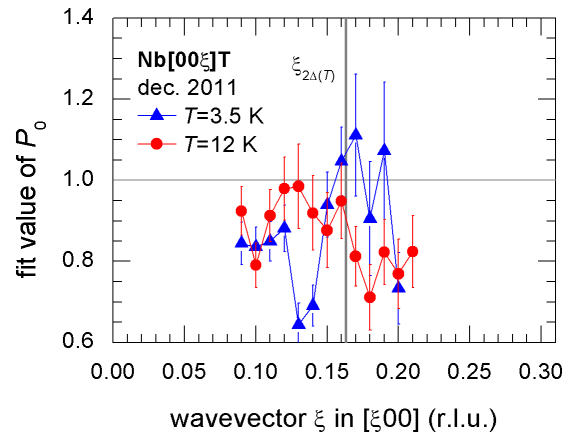
(c)

Figure 3.29.: *Fitted parameter P_0 of the exponential fits to the polarization profiles in Nb.*
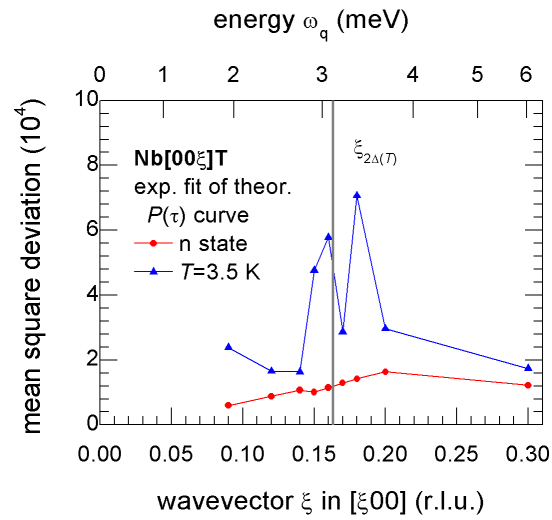
(a)
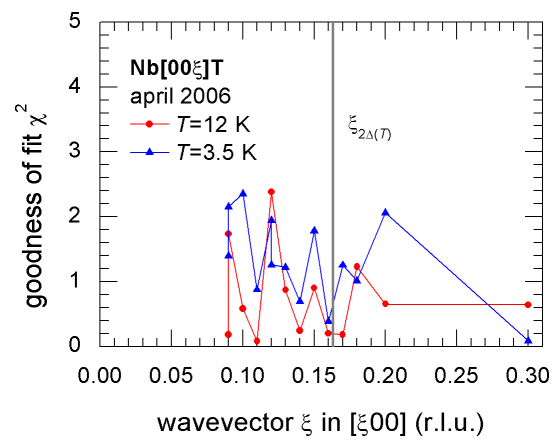
(b)
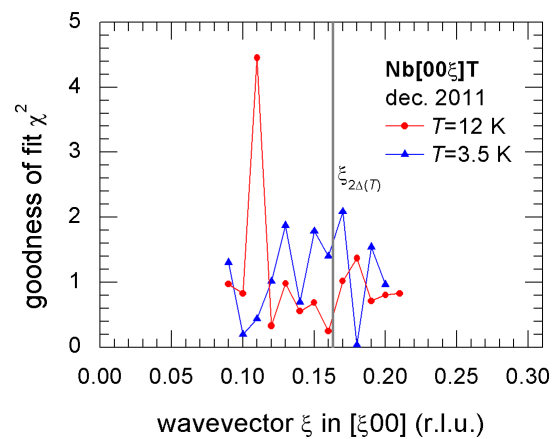
(c)

Figure 3.30.: *Experimental and theoretical goodness of the exponential fits to the polarization profiles in Nb.*
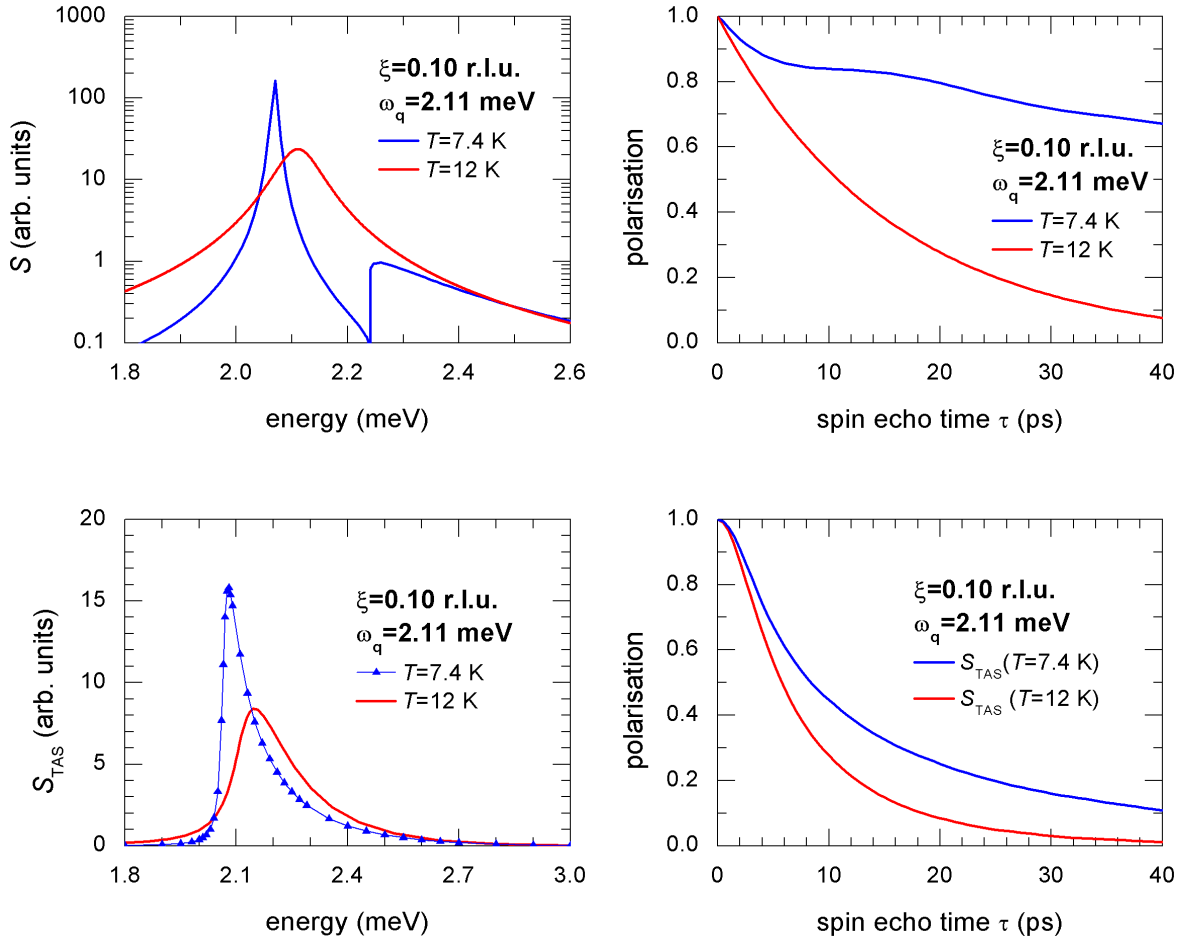
Figure 3.31.: *Calculated scattering functions at $T = 12\,K$ (red) and $7.4\,K$ (blue) (top left) and their Fourier transforms (top right) in the $Nb[00\xi]T$ phonon branch at $\xi = 0.10$. The scattering functions are shown on a logarithmic scale. (bottom left and right) Effective scattering functions and their Fourier transforms, assuming a resolution as in the April 2006-experiment.*

the gap: phonons may now interact with electrons that are excited beyond the gap in the electronic density of states. The overall phonon renormalization becomes less strong.
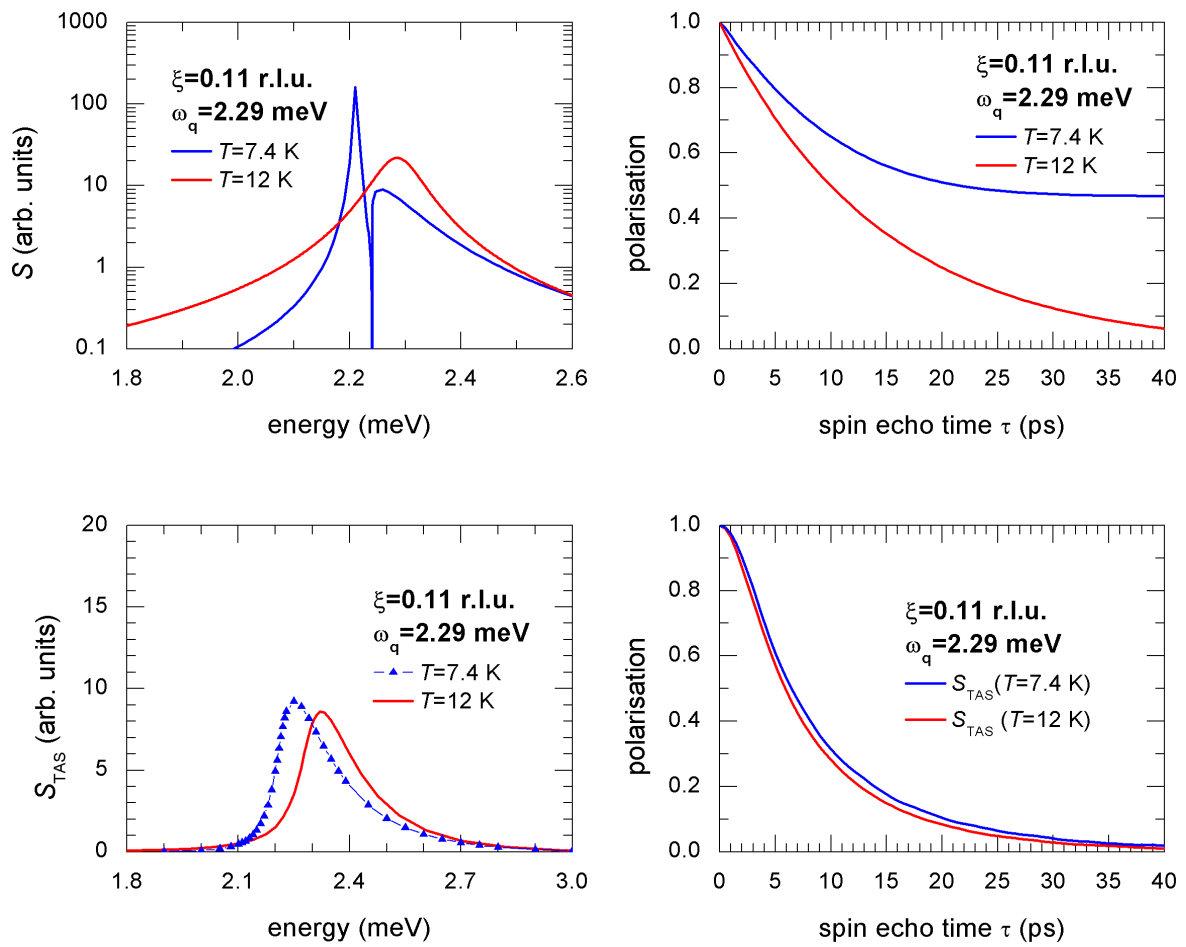
Figure 3.32.: *Same as Fig. 3.31 for $\xi = 0.11$.*
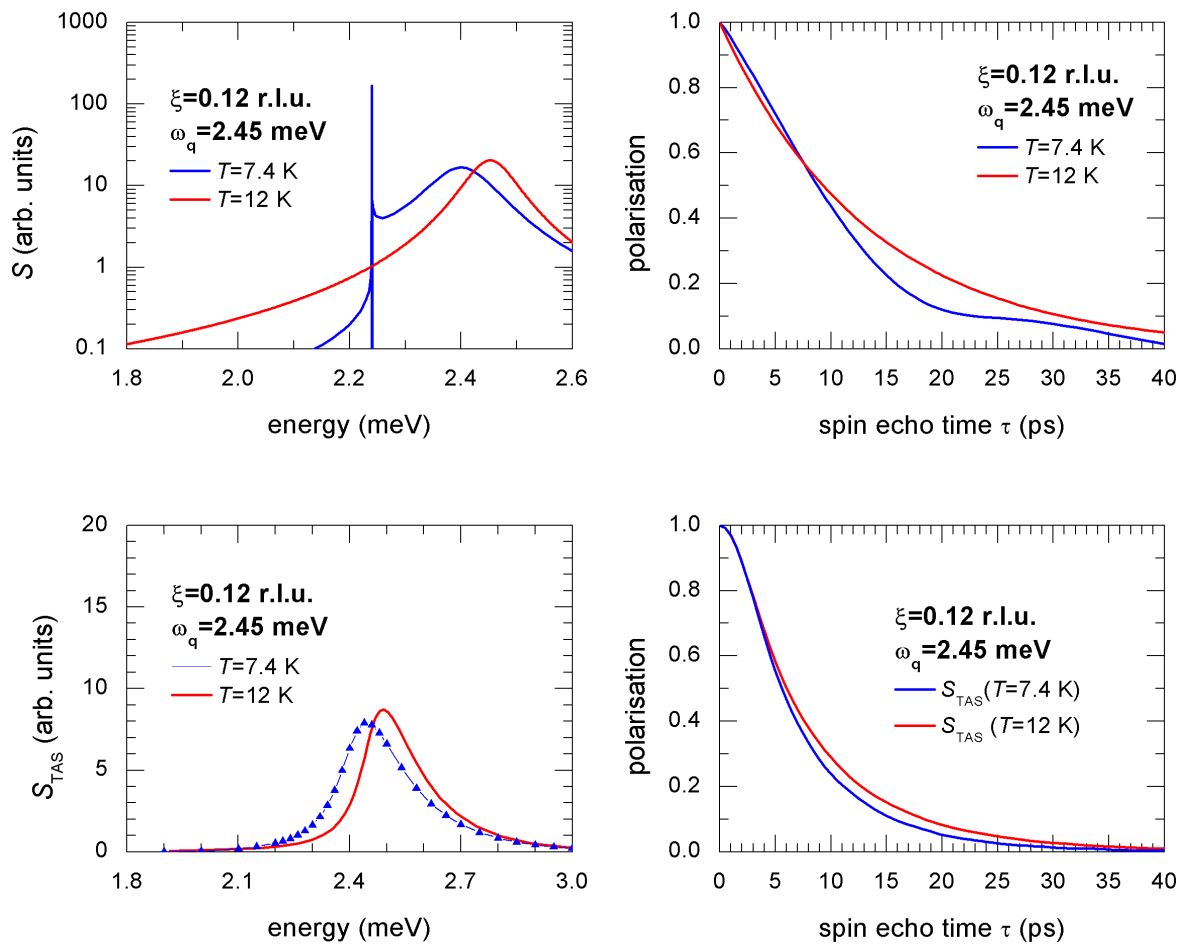
Figure 3.33.: *Same as Fig. 3.31 for ξ = 0.12.*
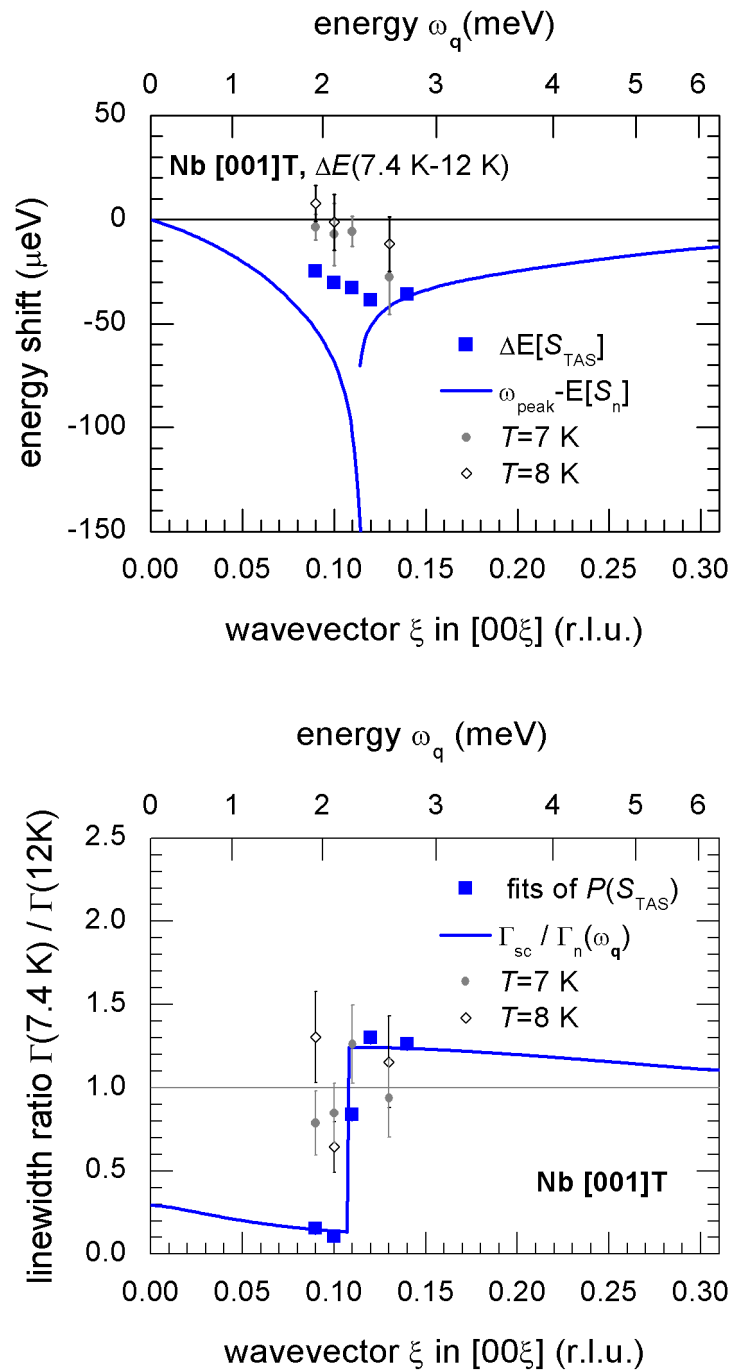
Figure 3.34.: *Energy shifts and linewidth ratio at $T/T_c = 0.8$.*

In the previous discussion, we observed several times that the absolute values of the linewidths deviate from the prediction of Allen's theory. The main reasons are a finite linewidth below the gap in the superconducting state and the Kohn anomaly, which adds an additional broadening to the N state values. The situation is summarized in Fig. 3.35, which shows the linewidths for both Nb and Pb for different **q**-directions. The situation becomes much clearer if only the differences of the linewidths and the energy shifts between sᴄ and N state are regarded. These are shown in Fig. 3.36 and Fig. 3.37. These differences agree very well with Allen's predictions if one chooses a model for the linewidths that neglects the broadening at finite ξ in the sᴄ state (the red curve in Fig. 3.35). This in turn again is an indication that the broadening in the sᴄ state has a different origin, not captured Allen's theory based on e-ph coupling and bᴄs theory.

From the linewidth and energy shift data values for $2\Delta(T)$ were extracted. These data are shown in Fig. 3.38 together with the standard bᴄs gap function. In Nb there is only a small difference between the (100) and the (110) directions. In lead, this difference is quite pronounced. This effect was already observed in tunneling experiments. As already pointed out earlier [20], this gap anisotropy might result from a variation of the Kohn anomaly along different crystallographic directions.
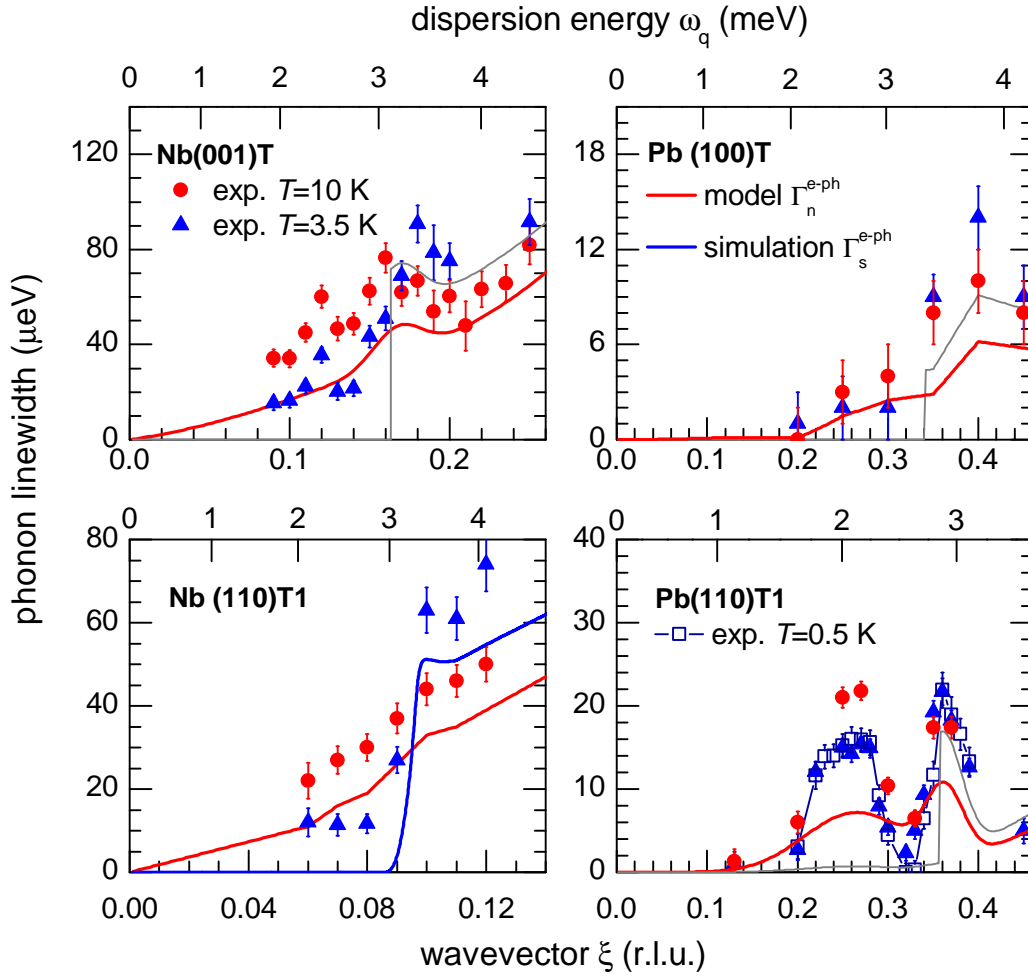
Figure 3.35.: *Intrinsic linewidth data below and above T_c (blue and red symbols, resp.) in niobium and lead, panels as in Fig. 3.36. Since the experimental linewidths of phonons that are well below the gap edge obviously do not take part in the renormalization, a phenomenological model for the share of the normal state linewidths that is affected is taken (green lines). The superconducting state simulations based on Allen's theory with finite NRSE resolution (black lines) agree well with the data.*
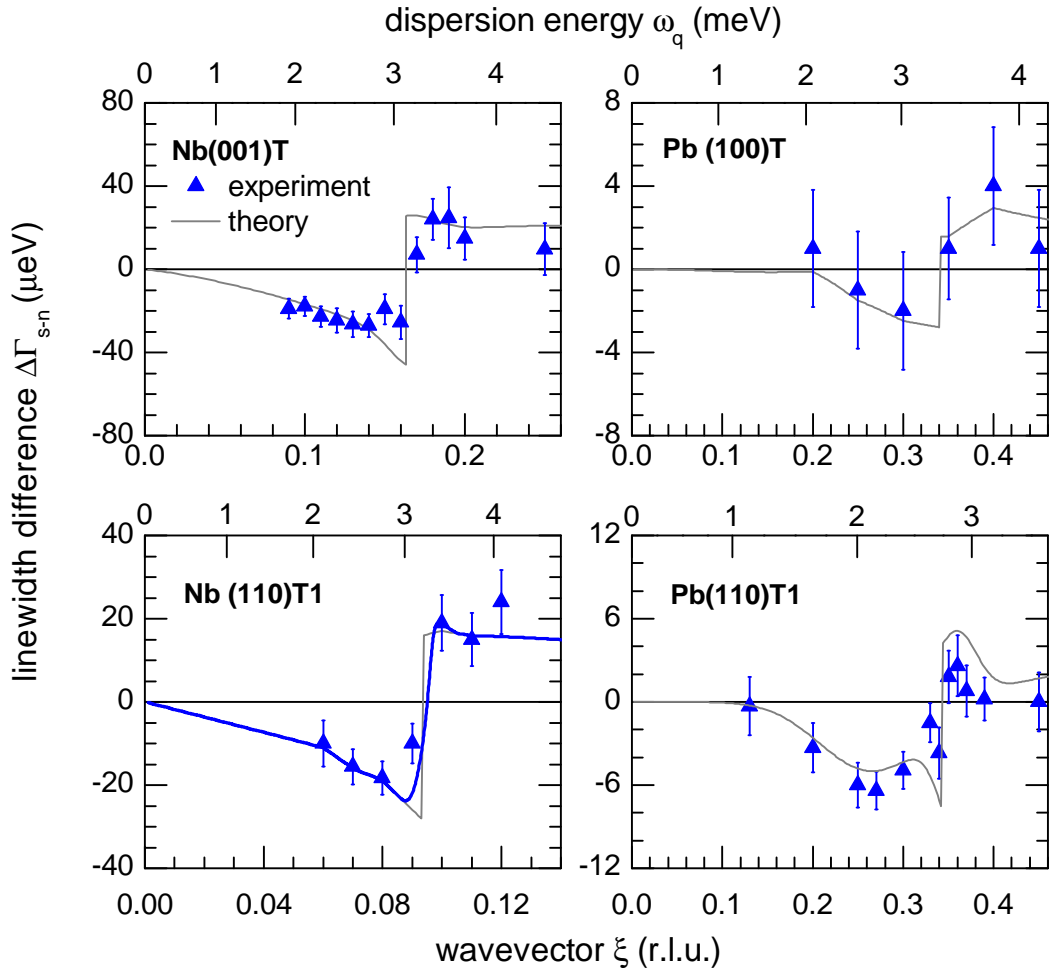
Figure 3.36.: *Difference between superconducting and normal state linewidths well below and just above T_c, respectively, in Nb $(100)T$ (top left), Nb $(110)T1$ (bottom left), Pb $(100)T$ (top right) and Pb $(110)T1$ (bottom right). The dispersion energy corresponding to the wavevectors is displayed on the top axes. Blue symbols denote experimental data, while black connected symbols denote the results of simulations based on Allen's theory that take the NRSE resolution into account. The grey thin lines give the local linewidth ratio at the dispersion energies according to theory.*
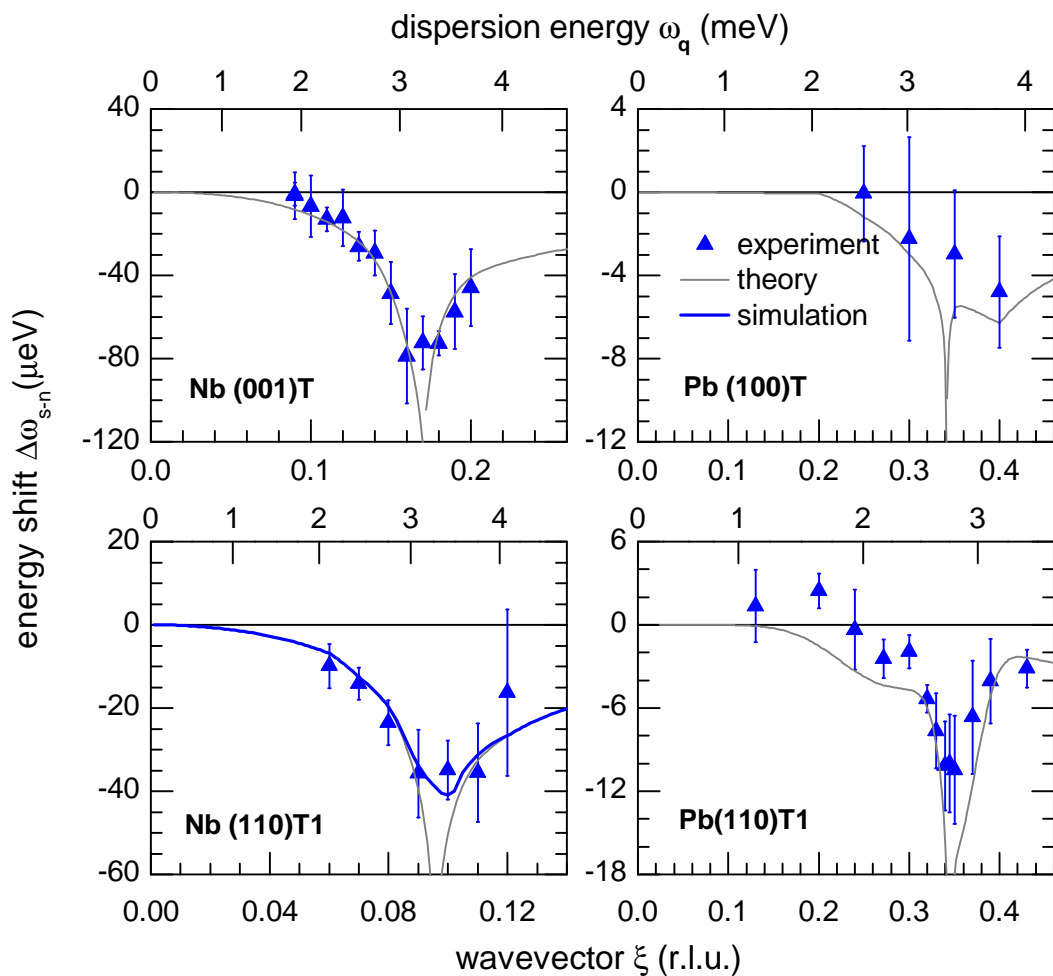
Figure 3.37.: *Energy shifts between superconducting and normal state phonons in niobium and lead, panels as in Fig. 3.36. Blue symbols denote* NRSE *data, while black connected dots denote the results of simulations based upon the normal state linewidth models shown in Fig. 3.35. Thin grey lines depict the local energy shifts at the dispersion energy according to theory.*
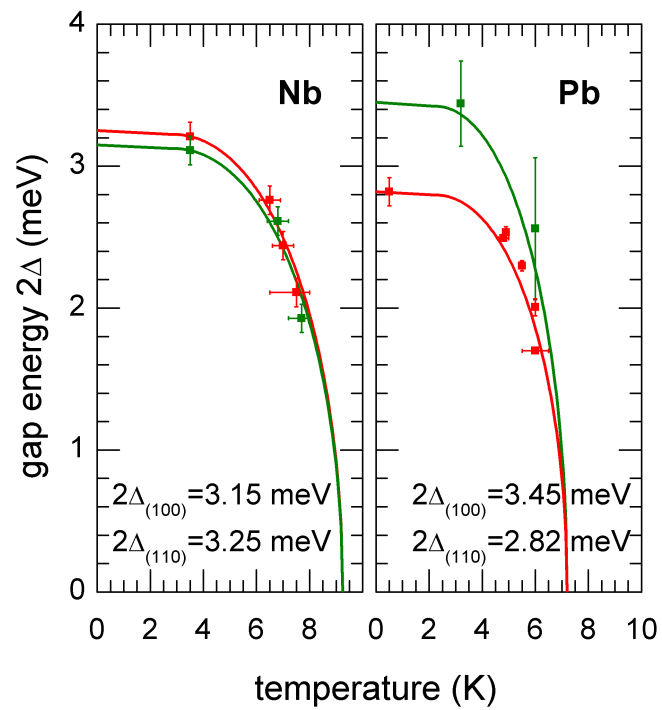
Figure 3.38.: *Temperature dependence of the energy gap in niobium (left panel) and lead (right panel), as determined from the lowest transverse acoustic phonon linewidths and energy shifts along (001) (green) and along (110) (red) and as a function of temperature. The lines represent the BCS expression for the energy gap.*

3.6. Summary and conclusions

From the analysis of the phonon renormalization in the superconducting state in different crystallographic directions in niobium and lead, respectively, the following conclusions can be drawn:

1. The qualitative behavior agrees with the predictions that come from the BCS theory, namely that a) phonons become sharper below the gap and broaden above the gap energy, while b) the dispersion softens at all times.

2. The linewidths are not reduced to zero in any of the cases even far below the gap edge. Most measurements were carried out at $3.5\,\mathrm{K}$, the only $0.5\,\mathrm{K}$ data are taken along the (110)T1 branch in Pb. This is a special case where the linewidths below the gap show a peak which is attributed to a three-phonon decay process. Other than this, the linewidths do not reduce to zero because: a) any other than electronic interaction. b) imperfect correction of the data c) the density-of-states in the gap is in fact not zero. In the tunneling density of states measurement, a Dynes gap is commonly used because of the finite temperature. A small current leakage that is linear in voltage persists, which is typically attributed to Andreev current, smeared density of states (DOS), nonvanishing DOS in the insulator within the gap, nonequilibrium quasiparticles, physical imperfections in the junction, or most recently, the electromagnetic environment of a tunnel junction (stray photon-assisted tunneling) [78]. Though the DOS is reduced, a superconductor with such a pseudogap is technically gapless. It was more recently argued that the Eliashberg complex gap function justifies such an alteration to the BCS gap function microscopically [79, 80].

3. While the relative broadening of the linewidths above the gap edge is consistent with prediction in three out of four cases, it is suspiciously low in Pb (110)T1. The relative broadening $\Gamma_s^{\mathrm{e-ph}}/\Gamma_n^{\mathrm{e-ph}}(\omega_{\mathbf{q}} \gtrsim 2\Delta(T))$ in Allen's theory depends on the gap to T_c ratio and the relative temperature T/T_c. Thus there is no other free parameter. It can only be suspected a) that part of the actual observed linewidth is not due to electron-phonon coupling and is unchanged in the superconducting state. This would mean that the Kohn anomaly actually does not extend beyond $\mathbf{q} \sim \mathbf{q}_{2\Delta}$. b) that there is ideal nesting here and the Allen approach does not capture the kinematic constraints.

4. In Nb (100)T, the energy shift below the gap edge is not as strongly curved in the simulation as in the simplified theory (which does not contain q resolution) and the experiment, because the increasing dispersion curvature makes the center of weight for different linewidths larger.

5. Apart from the oddity mentioned in (iv), the energy shifts in Nb match the simulations. This means that the e-ph coupling strength r is well chosen (i.e. the normal

state linewidths are exclusively due to e-ph interaction), and the gap width is well chosen in both cases. This speaks against solution a) and b) to point (ii).

6. The transitions in $\mathbf{q}$-space at $3.5\,$K (less than half of T_c) are nearly as acute as at $0.5\,$K and only broadened by the $\mathbf{q}$-resolution. The data are not inconsistent with the simulations, but they would be consistent with broader transitions as well.

7. From the linewidths at higher temperatures T/Tc 0.7,0.8 in Pb (110)T1 and from the temperature dependence at single points in Nb (110) and Pb (110) it follows that the transition is indeed broadened, and not only because the jump in Γ_s/Γ_n is less strong, but also intrinsically broadened. This means the Dynes gap is not a consequence of tunneling alone. More data are needed.

8. Concerning the pinpointing of 2Δ from the linewidth structure, the best method is to use the point where Γ_s changes from below to above Γ_n. This is different to using the peak position of the DOS, which is often done in ARPES and leads to slightly larger results.

Do these lineshape changes influence the congruence of the Kohn anomaly and the superconducting energy gap, as was found in several independent experiments? The answer is no: even if the gap estimate is smaller, still, the linewidth peak position of the Kohn anomaly coincides with the shoulder of the dip-hump structure in the superconducting state.

An open issue is to why the linewidth change for phonons across the energy gap go to zero much faster than predicted. Impurities tend to wash out the difference in the imaginary part of the self-energy [81]. Further, even low amounts of impurities reduce the energy shift below 2Δ. This could refine the match with the experimental results just as well as assuming a larger experimental broadening does. Square-root singularities drop faster than logarithmic ones do.

One dominant impurity in niobium might be hydrogen, which is easily dissolved in niobium. Hydrogen or deuterium atoms are distributed among the six tetrahedral interstitial sites. As deuterium is added to Nb, the anomalies in the dispersion curves of pure Nb are reduced because the loading with deuterium strongly affects the electron-phonon interaction which is responsible for the anomalies. A similar effect has been observed in the Nb-Mo alloy' where the anomalies are washed out as Mo is added, due to changes in the electronic structure, consistent with the rigid band model of Nb and Mo metal. The acoustic phonons at $473\,$K, which are very soft in pure Nb, tend to harden up when 15% H or more is present, especially around the Kohn anomalies [82]. However, such an effect was not observed here.

4. Superconductivity and electron-phonon interaction in Tl-Pb-Bi alloys

Inelastic neutron resonance spin-echo spectroscopy is used to measure acoustic phonon linewidths in lead alloyed with dilute concentrations of bismuth and thallium, respectively. The doping concentration is determined by prompt gamma activation analysis. The linewidths of the phonons, together with their dispersion, provide insight into the detailed electron-phonon (e-ph) interaction. Previous linewidth measurements in pure Pb and in Nb revealed Kohn anomalies in the lowest transverse acoustic branches that are not reproduced by *ab initio* calculations. A coincidence of the saturated superconducting energy gap magnitude $2\Delta_0$ with the energies of these anomalous phonons was found in both materials and in different crystallographic directions. Here we focus on the anomaly in Pb at the wavevector $\mathbf{q}_{\mathrm{KA}} \approx (0.36, 0.36, 0)$, where the phonon energy is $\hbar\omega_{\mathrm{KA}} = 2.85 \pm 0.10$ meV. This is equal to $2\Delta_{(110)}$, which was extracted from the same data by exploiting the change in e-ph coupling in the superconducting state with respect to the normal state. We show that the anomaly shifts to higher wavevectors when the electron-per-atom ratio increases. The energy gap rises with $\hbar\omega_{\mathrm{KA}}$, giving a further incentive to the notion that the two may be directly connected. Further we note that due to force constant and local environment disorder, the phonon linewidths in the alloys increase dramatically as a function of $\mathbf{q}$ with respect to the pure material [83].

4.1. Introduction

Though conventional BCS superconductors with s-wave symmetry are thought to be well-understood, the calculation of transition temperatures T_c from first principles is not straightforward. The exact value of T_c depends profoundly on the anisotropy of the energy gap on different parts of the Fermi surface (FS), which may be intricate [84]. Yet, a phenomenon observed by neutron inelastic scattering gives hope that the saturated energy gap $2\Delta_0$ may actually be tied to the Fermi surface topology in a surprisingly easy manner. A central role is taken by Kohn anomalies (KA), which appear as kinks in the phonon dispersion and peaks in the linewidth due to increased interaction with valence electrons

whenever the phonon wavevector $\mathbf{q}_{KA}$ connects substantial parts of the Fermi surface. Whenever acoustic phonons with energy close to $2\Delta_0$ are subject to a Kohn anomaly, the gap at the corresponding parts of the Fermi surface might conform to the energy of these phonons, $\hbar\omega_{KA}$. This was revealed by neutron resonance spin-echo (NRSE) measurements of the lowest transverse acoustic phonon linewidths in Pb and Nb [19, 23]. Just as remarkably, the Kohn anomalies that are involved are not reproduced by *ab initio* density-functional theory (DFT) calculations within the local-density approximation (LDA). The certainty that they are in fact due to the Kohn effect stems mainly from the temperature-independence of $\mathbf{q}_{KA}$ and the strong $\mathbf{q}$-dependence of the linewidths. Appropriate FS nesting conditions are present [22]. It was suggested that electronic correlations beyond the LDA might be responsible for making the phonons more prone to a Kohn anomaly [19], though this hypothesis has not been circumstantiated to date.

Here we study the phonon dispersion and linewidths of the (110)T1 lowest transverse acoustic phonon in lead with dilute concentrations of bismuth and thallium, respectively. Tl, Pb and Bi are neighbors in the periodic table, so that their alloys offer a gradually increasing electron concentration and electron-phonon (e-ph) coupling strength. The Tl-Pb-Bi substitutional system crystallizes in the face-centered cubic structure over an extended range from 80% Tl up to 20% Bi [85]. Since knowledge of the exact ratio of components in the studied parts of the samples is crucial to this study, prompt-gamma activation analysis (PGAA) was used to measure the doping concentration. Arbitrary force-constants in the randomly disordered alloys give rise to larger phonon linewidths with respect to pure Pb, which makes the identification of the Kohn anomaly harder. Nonetheless, the accompanying kink in the phonon dispersion is distinctly recognizable. We show that the nesting vector increases gradually as the number of electrons per atom increases. The energy of the phonon at the Kohn anomaly changes as much as the energy gap itself, giving further evidence that the two may be linked beyond the Eliashberg theory.

4.2. Experimental

One single lead-based crystal with thallium and two crystals with bismuth were grown with a nominal solute concentration of 15% each. Lesser-quality parts of the crystals were covered with neutron-absorbing cadmium during the experiment. To determine the true alloying concentrations and the homogeneity in the irradiated crystal parts, prompt-gamma activation upon neutron irradiation was used to measure the concentrations in 10 mm sections along the axial direction of the rods, as shown in Fig. 4.1. The relative concentrations of the neutron-capturing elements is revealed by the integrated area of each of the isotope-characteristic prompt-gamma peaks, divided by the respective cross section of the peak and detector efficiency at the peak energy. The lowest-energy peaks of Tl were not used, since the self-absorption by the lead in the sample is significant at these
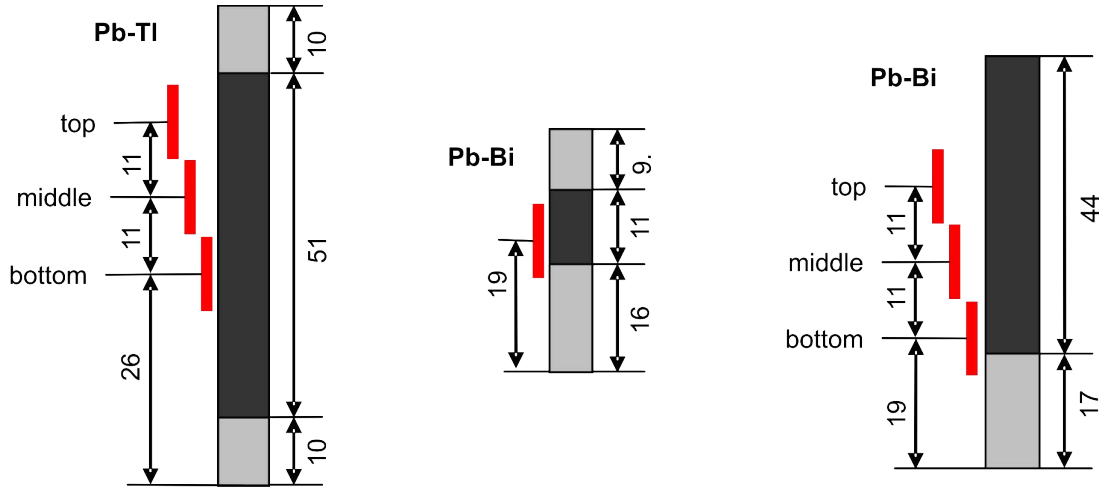
Figure 4.1.: *Schematic drawing of* PGAA-*illuminated areas (red) of the samples. Parts that were covered with Cadmium (light grey) in the neutron spectroscopic measurements at* TRISP *hence are not sampled; only the composition of the uncovered parts are of interest.*

Peak energy (keV)		
Tl	Bi	Pb
5180.38	4054.57	$\left.\begin{array}{l} 6729.38^a \\ 6737.62^a \end{array}\right\}$ doublet
5279.86	4101.76	
5641.57	$\left.\begin{array}{l} 4165.36^b \\ 4171.05 \end{array}\right\}$ doublet	7367.78
6166.61		
6514.57		
^{a}Only used in first experiment. ^{b}Not used.		

Table 4.1.: *Characteristic energies of prompt gamma rays used for calculation of the composition of the samples.*

energies. The peaks that were used are listed in Table 4.1. The cross sections of Bi were taken from the relatively recent publication of Borella and coworkers [86]. Results are listed in Table 4.2 and summarized in the end (Table 4.3). Since Tl, Pb and Bi have 3, 4, and 5 valence electrons, resp., the atomic ratio is simply expressed by the average number of valence electrons per atom n in the table. The thallium concentration of approx. 7% is considerably lower than that of the solution from which it was grown. The bismuth concentration in the effective volume of the smaller crystal ($V_{\text{eff}} = (\varnothing 6.3 \times 11)\,\text{mm}^3$) is ca. 9% and that in the larger crystal ($V_{\text{eff}} = (\varnothing 8 \times 44)\,\text{mm}^3$) is ca. 13%. While the distribution of thallium in lead is homogeneous, the concentration of bismuth in the large crystal varies up to a few atomic percent from one 10 mm-section to the next.

Neutron Larmor diffraction [34] was used to determine the gaussian full width at half-maximum (FWHM) of the mosaicity of the effective volume in the large Bi-crystal, $\eta =$

Crystal	x of entire crystal[a] (wt.%)	Average x of sections (wt.%)	Section name	x (wt.%)
Pb1-xTlx (∅7.5x71 mm)	-	6.68 (8)	top middle bottom	6.41 (18) 6.69 (10) 6.93 (10)
Pb1-xBix (∅6.3x36 mm)	7.8 (3)	9.25 (25)		9.25 (25)
Pb1-xBix (∅8x61 mm)	11.4 (5)	15.20 (22)	top middle bottom	17.93 (44) 14.67 (37) 12.99 (34)
[a] determined in first PGAA experiment.				

Table 4.2.: *Bismuth and thallium concentrations, respectively, in the three lead-based samples.*

$0.197 \pm 0.005°$, and the FWHM of the lattice constant spread, $\Delta a/a = (7.6 \pm 0.3) \cdot 10^{-4}$. The mosaicity of the Tl-doped specimen was estimated from neutron diffraction to be nearly one degree, which made it unsuitable for NRSE measurements.

The NRSE measurements of the acoustic phonon linewidths were performed on the thermal neutron spectrometer TRISP at the FRM II as described in detail before [18, 19]. The neutron beam is polarized with a supermirror guide and an energy is selected by a focusing pyrolytic graphite monochromator. The spin-echo is achieved by two sets of radiofrequency flipper coils, which can be tilted with respect to the beam direction to focus the spin-echo group onto the slope of the phonon dispersion. A Heusler analyzer is used to detect the final polarization and energy of the scattered neutrons. The linewidths are extracted from the polarization as a function of spin-echo time, which equals the Fourier transform of the Lorentzian spectral lineshape after correction for the instrumental resolution. Classic triple-axis measurements of the phonon dispersions were carried out on the same spectrometer. Higher-resolution dispersion measurements on the cold neutron spectrometer Panda at the FRM II were consistent with the values of TRISP for pure Pb up to 0.4 r.l.u. in the (110)T1 phonon branch. For the Pb-Tl sample however, measurements at wavevectors up to 0.44 r.l.u. at Panda yielded higher energies than at TRISP. The origin of this discrepancy could not be identified.

Since the samples were too large to fit into a regular physical property measurement system (PPMS), the T_c-measurements were carried out on TRISP as well, as explained in chapter 2. To this end, a magnetic field (roughly 10 Gauss) was applied in the sample area. The Larmor phase Φ averaged over the scattered neutrons jumps at the transition temperature since the magnetic field is expelled from the superconductor in the Meißner phase. Since the absolute Larmor phase angle is not relevant, Φ is set to zero at the lowest temperature. The results are shown in Fig. 4.2. The magnetic field in the sample region was weaker in the case of panel (a), hence the smaller phase jump. As can be seen, the onset of superconductivity occurred at 7.40 ± 0.10 K and 7.80 ± 0.06 K for the 9%-Bi

and the 13%-Bi sample, respectively. In the 7%-Tl alloy, T_c decreased to 6.97 ± 0.01 K compared to pure lead ($T_c = 7.20$ K).

4.3. Results and discussion

The dispersion curves of the lowest transverse acoustic phonons in the (110) direction in the two bismuth-doped samples at 10 K, well above T_c, are shown in the top panel of Fig. 4.3, next to the dispersion of pure lead [19]. The shape of each of the dispersion curves is notably similar but translated to higher wavevectors with increasing bismuth content. The curves appear to converge naturally near $(0.55, 0.55, 0)$. The energy at the zone boundary, not shown, tends to drop with increasing electron-per-atom ratio n in the Tl-Pb-Bi alloy system, as already known from previous experiments [8, 87]. As the overall phonon spectrum softens, the e-ph coupling constant λ rises [85].

The intrinsic linewidths measured by NRSE, shown in the bottom panel, display three distinct peaks for pure lead, as discussed in Ref. 19. The lowest-energy peak largely persists in the superconducting state at $T = 3.5$ K. Since the phonon energies around this point are not large enough to excite quasiparticles across the superconducting gap $2\Delta(T)$, the phonon broadening was not associated with e-ph coupling, but with spontaneous nearly collinear intra-branch phonon decay. Such decay processes are allowed under conservation of momentum and energy only because the phase velocity of the phonons exceeds the velocity of sound for small wavevectors [19]. The other peaks in the linewidth of pure Pb are Kohn anomalies, resulting from Fermi surface nesting. None of the peaks are captured by *ab initio* LDA calculations [19].

The Kohn anomaly centered at 0.360 ± 0.010 r.l.u. and 2.85 ± 0.10 meV is reflected as an upward kink in the dispersion. The point of highest slope in the dispersion, as determined from the inset, is marked by the dotted lines that are drawn all the way through the lower panel as well. It can be found at a slightly larger wavevector value than the center of the linewidth peak, which is to be kept in mind while we will refer to it as $\mathbf{q}_{KA}$. The order of magnitude of the modification of the dispersion induced by the KA can be estimated from the energy difference with respect to a fit with less oscillations. It is roughly ten times larger than the linewidth broadening, which implies that an ample scope in the energy continuum of the phonon self-energy $\Pi(\mathbf{q}, \omega)$ must be considered in the Kramers-Kronig transformation [88]. For the same reason, a quantitative analysis on the basis of these experimental data would be difficult. The kinks in both alloys are just as distinctive as in the pure material, suggesting that the Fermi surface is sufficiently well-defined and the nesting conditions remain pronounced.

However, the kinks in the dispersion are not accompanied by distinctive peaks in the linewidths for the alloys. In both samples, the linewidths climb from ca. $40\,\mu$eV up to

ca. $100\,\mu$eV in the range $0.36 - 0.40$ r.l.u. From the few data points at $T = 3.5$ K it can be concluded that the renormalization in the superconducting state is insubstantial, and thus that most of the phonon decay does not stem from e-ph interaction. Randomly substituted atoms destroy the translational symmetry and consequently wash out the electronic band structure and the phonon dispersion. Since mass disorder plays no larger role in these alloys than in pure Pb, which has several natural isotopes, the main sources of the phonon broadening are force-constant differences and the influence of the local environment in different random configurations of a super cell cluster. The density-functional super cell approach as described by Haverkort *et al.* [89] allows for randomness in the impurity contribution across super cell clusters. Regrettably, a feasibility study rendered that it is at present not economic to calculate the phonon linewidths caused by the $\sim 10\%$ share of random bismuth substitutions adopting this approach [90].

Previously, it was unexpectedly found that $\hbar\omega_{\mathrm{KA}}$ is equal to the gap averaged over the Fermi surface parts connected by the (110) phonons, $2\Delta_{(110)} = 2.82 \pm 6$ meV, in pure Pb. The gap $2\Delta_{(110)}$ was extracted from the same linewidth data by exploiting the change in e-ph coupling in the superconducting state with respect to the normal state. Here, the aim is to establish whether or not the saturated energy gap stays linked to the energy at the KA. Since the change of the linewidths in the superconducting state is insignificant in the alloys, the momentum-averaged gap values listed in Ref. 85 are used for reference. The momentum-averaged gap of Pb, 2.80 meV, agrees with $2\Delta_{(110)}$, so that gap anisotropy does not need to be considered. The values of $\hbar\omega_{\mathrm{KA}}$ and $2\Delta_0$ versus the electron-per-atom ratio in the samples are shown in Fig. 4.4. The upper value for the Tl-doped sample is taken at TRISP, while the lower value is taken from a fit to the dispersion recorded on the cold neutron triple-axis spectrometer Panda. Though the qualitative behavior of the two measured curves is identical, they drift apart for reasons unknown. The figure shows that the energy gap magnitude tends to stay just below the point of maximal slope in the dispersion curves measured on TRISP.

The lower panel of Fig. 4.4 shows the onset of superconductivity as a function of n compared to data from Ref. [85]. The error bars of T_c vary because of chosen temperature gradients during the measurement. This does not indicate that the transition would be less sudden. As can be seen, the values agree well with the literature.

The data are summarized in Table 4.3. Data on the KA from the Pb-Tl sample are not included due to the ambiguity discussed above.

4.4. Summary

The Kohn anomaly with $\hbar\omega_{\mathrm{KA}} \equiv 2\Delta_0$ in the lowest transverse acoustic phonon branch of pure lead was previously recognized by the distinct peak in the linewidth and upward

Sample	n	T_c (K)	$2\Delta_0$ (meV)	KA (r.l.u.)	KA (meV)
$Pb_{0.93}Tl_{0.07}$	3.933 (17)	6.97 (1)	2.72[b]	-	-
Pb	4	7.2[a]	2.82 (6)	0.371 (1)	2.96 (12)
$Pb_{0.91}Bi_{0.09}$	4.085 (10)	7.40 (10)	3.04[b]	0.390 (2)	3.02 (20)
$Pb_{0.87}Bi_{0.13}$	4.133 (27)	7.80 (6)	3.13[b]	0.437 (4)	3.32 (14)

[a] T_c from Ref. 91.

[b] Momentum-averaged gap, first order interpolation of data from Ref. 85.

Table 4.3.: *Coincidence between Kohn anomalies in the* (110) *T1 phonon dispersion and the energy gap in Pb-based alloys. The positions of the KAs are based on the kink in the dispersion.*

kink in the phonon dispersion. We found that as the Fermi level is modified by alloying with either thallium or bismuth, the upward kink is still clearly recognizable, but shifted, as expected. For each of the individual phonon dispersions, the energy at the Kohn anomaly stays close to the momentum-averaged energy gap magnitude from tunneling measurements for that alloying concentration. Of course, the energy gap shifts upward with increasing electron concentration for this system in agreement with the Eliashberg theory, just as the position of the upward Kohn anomaly is bound to shift upward. At the same time though, if it were not for the overall softening of the phonon spectra, then the energy at the Kohn anomaly would rise much faster than the energy gap. It is this delicate balance which is remarkable and gives gentle support to the hypothesis of a lock-in effect beyond, or hidden within, the accepted theory of superconductivity.

In principle, the strength of the lock-in effect could be tested under more adverse conditions using e.g. niobium doped with molybdenum or zirconium, respectively, because in this alloy system, the relevant nesting vector in the (001) direction moves to the origin as the superconducting transition temperature rises. However, in order to separate e-ph coupling from other effects, theoretical work is needed to quantify the increased acoustic phonon linewidths in alloys as a function of wavevector, specifically regarding random substitutions that are not dominated by mass difference.
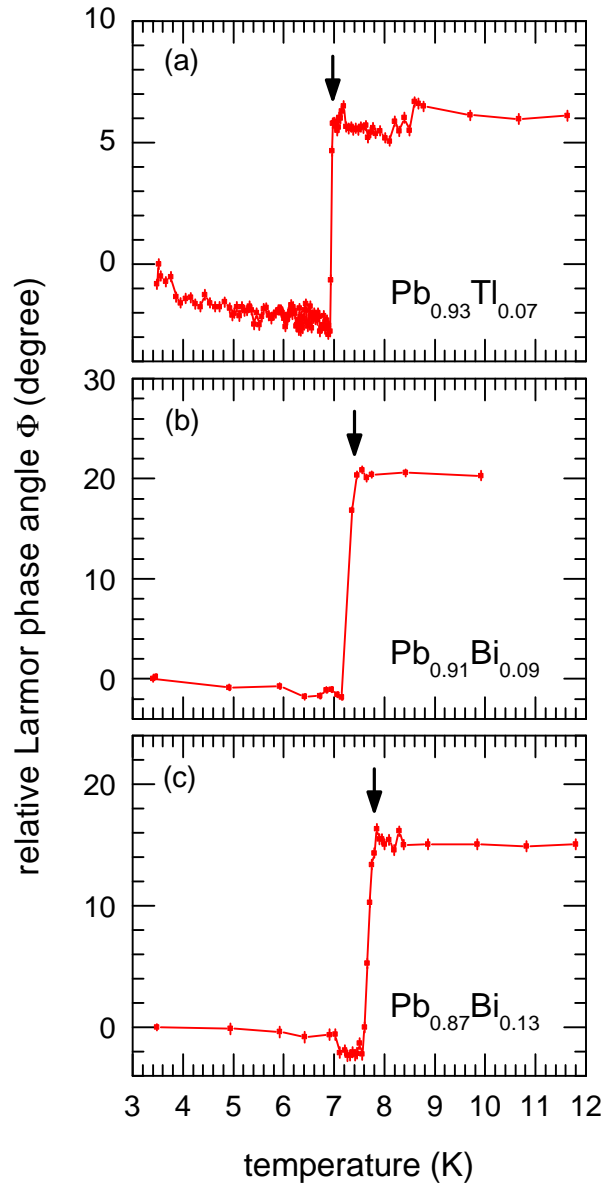
Figure 4.2.: T_c-measurements of the binary alloys on TRISP. The arrows indicate the onset of superconductivity. The data from panels (b) and (c) were shown previously in Aynajian's PhD thesis [20].
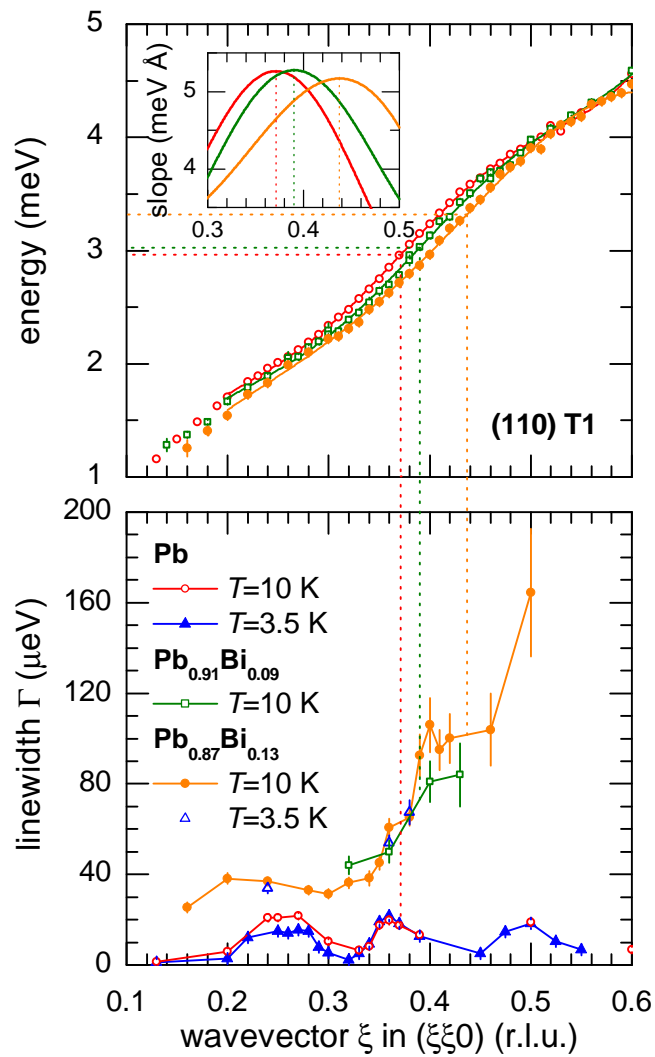
Figure 4.3.: *Dispersion (top) and intrinsic linewidths (bottom) of the* $(110)\,T1$ *phonon branch in pure Pb and in the two Pb-Bi samples. The dispersions are fitted in the range* $0.2 - 0.6\,r.l.u.$ *using a 5-parameter Born-Von Kármán (BvK) model. The respective position of each of the kinks near* $\xi \sim 0.4\,r.l.u.$ *(marked by intersecting lines) is determined from the slope of the fits (inset).*
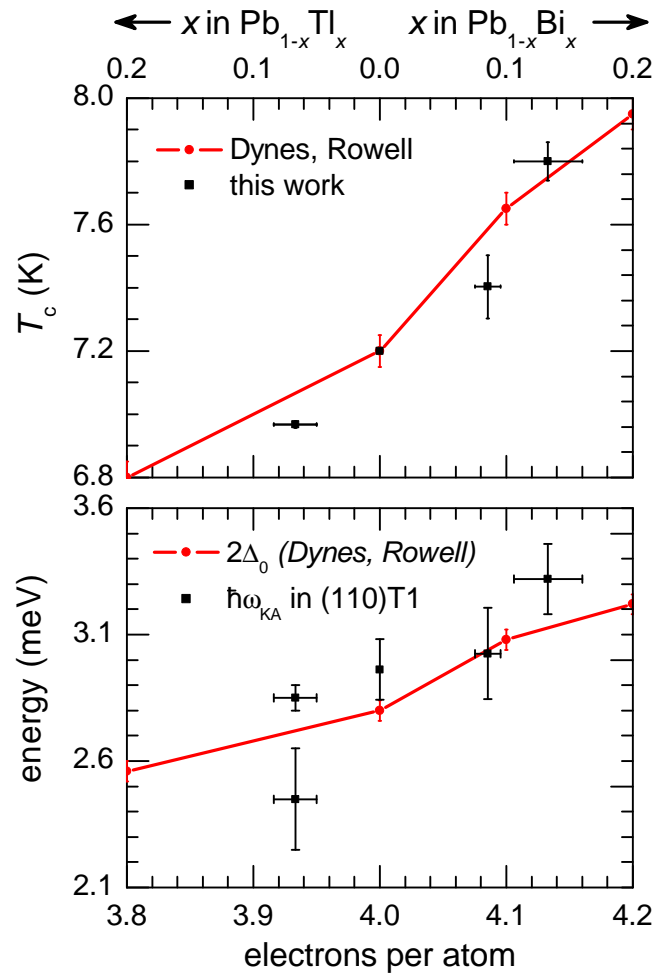
Figure 4.4.: *The top panel shows a comparison of the phonon energy at the Kohn anomaly taken from Fig. 4.3 (black symbols) with the momentum-averaged superconducting energy gap $2\Delta_0$ from tunneling data [85] (red line). Error bars do not include systematic errors. The lower panel shows the transition temperature of each sample (black symbols) compared to data from Ref. [85] (red line). Error bars of the data from the reference are based on the specifications made with regard to typical widths of the transition and reproducibility of the gap magnitude.*

Bibliography

[1] Bardeen, J., Cooper, L. N., and Schrieffer, J. R. *Phys. Rev.* **108**, 1175–1204 Dec (1957).

[2] Eliashberg, G. *Sov. Phys. JETP* **11**(3), 696–702 (1960). Vzaimodeistvie elektronov s kolebaniyami reshetki v sverkhprovodnike, ZhETF, 38(3), 966-974 (1960).

[3] Morel, P. and Anderson, P. W. *Phys. Rev.* **125**, 1263–1271 Feb (1962).

[4] Scalapino, D. J., Schrieffer, J. R., and Wilkins, J. W. *Phys. Rev.* **148**, 263–279 Aug (1966).

[5] McMillan, W. L. *Phys. Rev.* **167**, 331–344 Mar (1968).

[6] Hahn, A., Hofmann, S., Krause, A., and Seidel, P. *Phys. C Supercond.* **296**, 103 – 118 (1998).

[7] Tomlinson, P. G. and Carbotte, J. P. *Phys. Rev. B* **13**, 4738–4744 Jun (1976).

[8] Allen, P. B. and Dynes, R. C. *Phys. Rev. B* **11**, 1895–1905 Mar (1975).

[9] Savrasov, S. Y. and Savrasov, D. Y. *Phys. Rev. B* **54**(23), 16487–16501 Dec (1996).

[10] Kohn, W. *Phys. Rev. Lett.* **2**, 393–394 May (1959).

[11] Anderson, J. R. and Gold, A. V. *Phys. Rev.* **139**, A1459–A1481 Aug (1965).

[12] Taylor, P. L. *Phys. Rev.* **131**, 1995–1999 Sep (1963).

[13] Brockhouse, B. N., Arase, T., Caglioti, G., Rao, K. R., and Woods, A. D. B. *Phys. Rev.* **128**, 1099–1111 Nov (1962).

[14] Shapiro, S. M., Shirane, G., and Axe, J. D. *Phys. Rev. B* **12**(11), 4899–4908 Dec (1975).

[15] Axe, J. D. and Shirane, G. *Phys. Rev. B* **8**, 1965–1977 Sep (1973).

[16] Gähler, R. and Golub, R. *Z. Phys. B* **65**, 269–273 (1987). 10.1007/BF01303712.

[17] Habicht, K., Golub, R., Mezei, F., Keimer, B., and Keller, T. *Phys. Rev. B* **69**, 104301 Mar (2004).

[18] Keller, T., Aynajian, P., Habicht, K., Boeri, L., Bose, S. K., and Keimer, B. *Phys. Rev. Lett.* **96**, 225501 Jun (2006).

[19] Aynajian, P., Keller, T., Boeri, L., Shapiro, S. M., Habicht, K., and Keimer, B. *Science* **319**(5869), 1509–1512 (2008).

[20] Aynajian, P. *Electron-Phonon Interaction in Conventional and Unconventional Superconductors.* PhD thesis, Max Planck Institute for Solid State Research, Stuttgart, (2009).

[21] Scalapino, D. J. *Science* **319**(5869), 1492–1493 (2008).

[22] Johnston, S., Sorini, A. P., Moritz, B., Devereaux, T. P., and Scalapino, D. J. *Phys. Rev. B* **84**, 174523 Nov (2011).

[23] Munnikes, N., Aynajian, P., Keller, T., Boeri, L., and Keimer, B. to be published, (2013).

[24] Kawano, H., Yoshizawa, H., Takeya, H., and Kadowaki, K. *Phys. Rev. Lett.* **77**(22), 4628–4631 Nov (1996).

[25] Allen, P. B., Kostur, V. N., Takesue, N., and Shirane, G. *Phys. Rev. B* **56**(9), 5552–5558 Sep (1997).

[26] Weber, F. and Pintschovius, L. *Phys. Rev. B* **82**(2), 024509 Jul (2010).

[27] Reznik, D. *Phys. C Supercond.* **481**(0), 75 – 92 (2012).

[28] Carbotte, J. P., Timusk, T., and Hwang, J. *Reports on Progress in Physics* **74**(6), 066501 (2011).

[29] Inosov, D. S., Park, J. T., Charnukha, A., Li, Y., Boris, A. V., Keimer, B., and Hinkov, V. *Phys. Rev. B* **83**, 214520 Jun (2011).

[30] Scalapino, D. J. *Rev. Mod. Phys.* **84**, 1383–1417 Oct (2012).

[31] Mezei, F., editor. *Neutron Spin Echo*, volume 128 of *Lecture Notes in Physics.* Berlin: Springer, (1979).

[32] Mezei, F., editor. *Neutron spin echo and polarised neutrons*, Proc. Int. Symp. on Neutron Scattering. Vienna, (1977).

[33] Pynn, R. *J. Phys. E* **11**(11), 1133 (1978).

[34] Rekveldt, M. T., Keller, T., and Golub, R. *Europh. Lett.* **54**(3), 342 (2001).

[35] Squires, G. *Introduction to the Theory of Thermal Neutron Scattering.* Cambridge University Press, (1978).

[36] G. Shirane, S. S. and Tranquada, J. *Neutron Scattering with a Triple-Axis Spectrometer: Basic Techniques.* Cambridge University Press, (2002).

[37] Cooper, M. J. and Nathans, R. *Acta Crystallogr.* **23**(3), 357–367 Sep (1967).

[38] Popovici, M. *Acta Crystallogr. Sec. A* **31**(4), 507–513 Jul (1975).

[39] Habicht, K. SeRescal v1.0, distributed by K. Habicht: habicht@hmi.de, (2003). NRSE-TAS resolution matrix calculations based on the RESCAL code for Matlab by D.A. Tennant and D. McMorrow.

[40] Zheludev, A. ResLib v3.4c, distributed by A. Zheludev: www.neutron.ethz.ch/research/resources/reslib, Oct (2009). Popovici and Cooper-Nathans resolution matrix calculations and other in Matlab.

[41] Byrne, J. *Neutrons, nuclei, and matter: an exploration of the physics of slow neutrons.* Institute of Physics Publishing, (1994).

[42] Rabi, I. I., Ramsey, N. F., and Schwinger, J. *Rev. Mod. Phys.* **26**, 167–171 Apr (1954).

[43] Gähler, R. and Golub, R. *J. Phys. France* **49**, 1195 – 1202 (1988). 10.1051/jphys:019880049070119500.

[44] Bloch, F. and Siegert, A. *Phys. Rev.* **57**, 522–527 Mar (1940).

[45] Habicht, K., Keller, T., and Golub, R. *J. Appl. Crystallogr.* **36**(6), 1307–1318 Dec (2003).

[46] Keller, T. and Habicht, K. "2ndorderCANNSERESx07thomasversion.pdf", (2005). Resolution Function for TAS with NSE II: Dispersive Excitations.

[47] Keller, T., Rekveldt, M., and Habicht, K. *Appl. Phys. A Mater. Sci. Process.* **74**, s127–s129 (2002). 10.1007/s003390101082.

[48] www.frm2.tum.de. Research neutron source Heinz Maier-Leibnitz (FRM II).

[49] Habicht, K., Enderle, M., Fåk, B., Hradil, K., Böni, P., and Keller, T. *J. Phys.: Conf. Ser.* **211**(1), 012028 (2010).

[50] Náfrádi, B., Keller, T., Manaka, H., Zheludev, A., and Keimer, B. *Phys. Rev. Lett.* **106**(17), 177202 Apr (2011).

[51] Allen, P. B. *Phys. Rev. B* **6**(7), 2577–2579 Oct (1972).

[52] Dynes, R. C., Narayanamurti, V., and Garno, J. P. *Phys. Rev. Lett.* **41**, 1509–1512 Nov (1978).

[53] Maris, H. J. and Tamura, S.-i. *Phys. Rev. B* **47**, 727–739 Jan (1993).

[54] de L. Kronig, R. *J. Opt. Soc. Am.* **12**(6), 547–556 Jun (1926).

[55] Kramers, H. *Atti Cong. Intern. Fisica, (Transactions of Volta Centenary Congress) Como* **2**, 545–557 (1927).

[56] Toll, J. S. *Phys. Rev.* **104**(6), 1760–1770 Dec (1956).

[57] Butler, W. H., Pinski, F. J., and Allen, P. B. *Phys. Rev. B* **19**(7), 3708–3721 Apr (1979).

[58] Alers, G. A. and Waldorf, D. L. *Phys. Rev. Lett.* **6**(12), 677–679 Jun (1961).

[59] Mattheiss, L. F. *Phys. Rev. B* **1**(2), 373–380 Jan (1970).

[60] Lam, P. K., Dacorogna, M. M., and Cohen, M. L. *Phys. Rev. B* **34**(8), 5065–5069 Oct (1986).

[61] Weber, F., Kreyssig, A., Pintschovius, L., Heid, R., Reichardt, W., Reznik, D., Stockert, O., and Hradil, K. *Phys. Rev. Lett.* **101**(23), 237002 Dec (2008).

[62] Schuster, H. G. *Solid State Commun.* **13**(10), 1559 – 1562 (1973).

[63] Zeyher, R. *Phys. Rev. B* **44**(17), 9596–9604 Nov (1991).

[64] Marsiglio, F. *Phys. Rev. B* **47**(9), 5419–5427 Mar (1993).

[65] Kee, H.-Y. and Varma, C. M. *Phys. Rev. Lett.* **79**(21), 4250–4253 Nov (1997).

[66] Karakozov, A. and Maksimov, E. *J. Exp. Theor. Phys.* **88**, 987–996 (1999). 10.1134/1.558881.

[67] Klam, L. private communication, (2010).

[68] Clem, J. R. *Ann. Phys.* **40**(2), 268 – 295 (1966).

[69] Nakagawa, Y. and Woods, A. D. B. *Phys. Rev. Lett.* **11**(6), 271–274 Sep (1963).

[70] Trivisonno, J., Vatanayon, S., Wilt, M., Washick, J., and Reifenberger, R. *J. Low Temp. Phys.* **12**, 153–169 (1973). 10.1007/BF00654733.

[71] Landa, A., Klepeis, J., Söderlind, P., Naumov, I., Velikokhatnyi, O., Vitos, L., and Ruban, A. *J. Phys. Condens. Matter* **18**(22), 5079 (2006).

[72] Landa, A., Söderlind, P., Velikokhatnyi, O. I., Naumov, I. I., Ruban, A. V., Peil, O. E., and Vitos, L. *Phys. Rev. B* **82**(14), 144114 Oct (2010).

[73] Struzhkin, V. V., Timofeev, Y. A., Hemley, R. J., and Mao, H.-k. *Phys. Rev. Lett.* **79**(21), 4262–4265 Nov (1997).

[74] Boeri, L. unpublished, (2011). Dft-lda calculation of the nesting function in Nb(001).

[75] Crabtree, G. W., Dye, D. H., Karim, D. P., Campbell, S. A., and Ketterson, J. B. *Phys. Rev. B* **35**(4), 1728–1741 Feb (1987).

[76] Fawcett, E., Reed, W. A., and Soden, R. R. *Phys. Rev.* **159**, 533–539 Jul (1967).

[77] Reed, W. A. and Soden, R. R. *Phys. Rev.* **173**, 677–679 Sep (1968).

[78] Pekola, J. P., Maisi, V. F., Kafanov, S., Chekurov, N., Kemppinen, A., Pashkin, Y. A., Saira, O.-P., Möttönen, M., and Tsai, J. S. *Phys. Rev. Lett.* **105**, 026803 Jul (2010).

[79] Mitrovic, B. and Rozema, L. A. *J. Phys.: Condens. Matter* **20**(1), 015215 (2008).

[80] Noguchi, T., Suzuki, T., Endo, A., and Tamura, T. *Phys. C Supercond.* **469**, 1585–1588 (2009).

[81] Marsiglio, F., Akis, R., and Carbotte, J. P. *Phys. Rev. B* **45**, 9865–9871 May (1992).

[82] Rowe, J. M., Vagelatos, N., Rush, J. J., and Flotow, H. E. *Phys. Rev. B* **12**, 2959–2964 Oct (1975).

[83] Munnikes, N., Aynajian, P., Keller, T., Keimer, B., and Canella, L. to be published, (2013).

[84] Floris, A., Sanna, A., Massidda, S., and Gross, E. K. U. *Phys. Rev. B* **75**, 054508 Feb (2007).

[85] Dynes, R. C. and Rowell, J. M. *Phys. Rev. B* **11**, 1884–1894 Mar (1975).

[86] Borella, A., Moens, A., Schillebeeckx, P., Van Bijlen, R., Molnar, G., Belgya, T., Revay, Z., and Szentmiklosi, L. *J. Radioanal. Nucl. Chem.* **265**, 267 (2005).

[87] Ng, S. and Brockhouse, B. *Neutron Inelastic Scattering - International Atomic Energy Agency, Vienna* **1**, 253–266 (1968).

[88] Dolgov, O. V., Andersen, O. K., and Mazin, I. I. *Phys. Rev. B* **77**(1), 014517 Jan (2008).

[89] Haverkort, M. W., Elfimov, I. S., and Sawatzky, G. A. *ArXiv e-prints 1109.4036* Sep (2011).

[90] Boeri, L. and Haverkort, M. private communication, (2012). Feasibility study of numerical phonon linewidth calculations for a randomly disordered Pb-Bi alloy.

[91] Carbotte, J. P. *Rev. Mod. Phys.* **62**, 1027–1157 Oct (1990).

Acknowledgements

List of Figures

Nomenclature

$(\hbar)\omega$ (phonon) energy, page 21

$(\mathbf{Q}_0, \omega_0)$ average momentum and energy transfer for a given TAS configuration, page 21

$2\Delta_0$ superconducting energy gap at zero temperature, page 10

$2\mathbf{k_F}$ Fermi surface spanning vector, page 7

$\alpha^2(\omega)$ electron-phonon coupling factor in Eliashberg theory, page 6

$\Delta(\omega)$ generalized energy gap equation in Eliashberg theory, page 7

$\Delta\omega$ energy difference with respect to the most probable energy transfer, page 67

Γ phonon linewidth, page 40

$\hbar$ Planck's constant, page 7

λ electron-phonon coupling parameter, page 6

λ wavelength, page 19

$\hat{\epsilon}$ phonon polarization, page 21

$\mathbf{C}$ slope of the surface of constant spin-echo phase, page 29

$\mathbf{G}$ reciprocal lattice vector, page 20

$\mathbf{k_{I,F}}$ most probable neutron wavevectors, page 19

$\mathbf{k_{i,f}}$ neutron wavevectors before and after the sample, resp., page 19

k   electron or neutron momentum, page 43

M   triple-axis resolution matrix, page 22

Q   neutron momentum loss, page 19

q   phonon momentum, page 20

X   four component vector in momentum and energy space, page 22

$\Omega_{\mathbf{q}}$ phonon energy if all interactions were switched off, page 44

$\omega_{\mathbf{q}}$ normal state phonon dispersion energy, page 44

ω_{peak} energy of the phonon resonance peak in the superconducting state, page 65

ϕ Larmor precession phase, page 30

Π self-energy, page 42

σ scattering cross section, page 18

τ spin-echo time, page 29

ε electron energy, page 43

$\varepsilon_{\mathbf{k}}^{0}$ electron band dispersion, page 44

b scattering length, page 18

c_{T} transverse acoustic phonon slope for $\omega \to 0$, page 11

D_{0} bare Green's function, page 42

E_{i} neutron energies before and after the sample, resp., page 19

$E_{I,F}$ most probable neutron energies, page 20

F NRSE resolution function, page 32

f Fermi-Dirac distribution, page 50

$F(\omega)$ phonon density of states, page 6

g electron-phonon coupling constant, page 43

G^0 electron propagator, page 43

m_n neutron mass, page 19

$N(0)$ electronic density of states at the Fermi surface, page 7

R triple-axis resolution function, page 21

r ratio of phonon linewidth and dispersion energy, page 49

S spectral function, page 42

S_{TAS} effective spectral function after integration over the NRSE resolution, page 69

$T(\mathbf{k_i}, \mathbf{k_f})$ instrument transmission probability, page 32

T_c superconducting transition temperature, page 8

v_F Fermi velocity, page 43

A1...A6 incident and scattering angles at the monochromator, sample and analyzer, in due order, page 20

Glossary

ARPES angle-resolved photoemission spectroscopy. 95

bcc body-centered cubic (crystal structure). 8, 60

BCS theory microscopic theory of superconductivity proposed by Bardeen, Cooper and Schrieffer. 4–8, 11, 13, 40, 41, 48–50, 89, 93, 94, 96, 121–123, 125–127

BvK fit fit of the phonon dispersion based on the Born-Von Kármán boundary conditions in a periodic lattice. 50, 54, 61, 62, 104

DFT density functional theory. 51, 53, 97, 127

DOS density of states. 6, 7, 94, 95

e-ph interaction electron-phonon interaction. 6, 7, 42, 43, 45, 46, 61, 62, 89, 94–97, 100–102, 125, 127–129, 131

fcc face-centered cubic crystal structure. 7

FRM II research reactor Heinz Maier-Leibnitz. 10, 17, 24, 37, 38, 99, 113, 120, 122

FS fermi surface. 7, 96, 97

FWHM full width at half maximum. 10, 30, 70, 71, 98, 99

HWHM full width at half maximum. 40, 45

KA Kohn anomaly. 102, 115, 127, 129–131

LDA local-density approximation. 51, 97, 100, 127, 129

A. Erweiterte Deutsche Zusammenfassung

In dieser Arbeit wurden Anomalien akustischer Phononen in den elementaren Supraleitern Nb und Pb und in supraleitenden Blei-Thallium und Blei-Wismuth Legierungen untersucht. Mittels hochauflösender Spin-Echo Neutronenspektroskopie wurden Auflösungen im Bereich einiger μeV erreicht, was einer Verbesserung von mehreren Größenordnungen im Vergleich zu konventioneller Neutronenspektroskopie entspricht. Bei Phononen-Energien nahe der Energielücke 2Δ und bei Temperaturen um die Sprungtemperatur T_c treten verschiedene Renormalisierungseffekte und Anomalien auf. Während die relativen Änderungen der Linienbreiten und der Energien gut mit Vorhersagen basierend auf der BCS-Theorie übereinstimmen, weichen die Absolutwerte signifikant davon ab. Überraschend ist die Koinzidenz der zu einer Kohn-Anomalie gehörigen Phononenenergie mit $2\Delta(T = 0\,\mathrm{K})$, sowohl in Nb als auch in Pb. Mittels Neutronenspektroskopie an verschiedenen $\mathrm{Pb}_{1-x}\mathrm{Bi}_x$ und $\mathrm{Pb}_{1-x}\mathrm{Tl}_x$ Legierungen konnte gezeigt werden, dass die Energielücke $2\Delta(T = 0\,\mathrm{K})$ der Energie der sich mit x in den Legierungen ändernden Kohn Anomalie folgt.

A.1. Methode

Die Dispersion akustischer Phononen in Blei und Niob wurde schon in den sechziger Jahren mit Hilfe der Dreiachsen-Neutronenspektrometrie gemessen. Die Messung der zugehörigen Spektrallinienbreiten gestaltet sich jedoch schwieriger, da Phononen bei niedrigen Temperaturen generell langlebig sind und ihre Linienbreiten einige mueV oder weniger betragen. Diese Auflösung kann unter Ausnutzung des Spin-Echo Prinzips [31] erreicht werden, das die Larmor-Präzession der Neutronenspins in einem Magnetfeld vor der Probe und einem entgegengesetzten Magnetfeld nach der Probe als eine Art "innere Uhr" des Neutrons nutzt. Wenn Neutronen mit unterschiedlichen Geschwindigkeiten die gleiche Trajektorie und den gleichen Streuprozess durchlaufen, ist ihre Spinrichtung am Ende gleich und die gemessene Polarisation maximal. Falls die übertragenen Energien während des Streuprozesses jedoch unterschiedlich sind, so spreizen sich die Spinphasen und die Polarisation sinkt. Demnach ist die Genauigkeit, mit der die Spektralverteilung der Anregung bestimmt wird, von der Spektralverteilung des Neutronenstrahls entkoppelt und sehr hohen Energieauflösungen werden möglich.

Eine ausgeklügelte Fokussierungstechnik, vorgeschlagen von Mezei [32, 31] und ausgearbeitet von Roger Pynn [33], bietet zudem eine Lösung für die unerwünschte zusätzliche Energieverteilung dispersiver Anregungen: Durch Verkippen der Magnetfeldgrenzen bezüglich der Haupt-Neutronenstrahlrichtung können die Spinphasen unter verschiedenen Winkeln gestreuter Neutronen aneinander angeglichen werden. Mit diesem Freiheitsgrad kann das Spin-Echo der Steigung der Dispersionskurve angepasst werden. 1987 schlugen Golub and Gähler die Neutronen Resonanz Spin-Echo (NRSE) Technik vor, die die notwendigen Kippwinkel technisch ermöglicht. Hierbei werden die Zylinderspulen zur Erzeugung des homogenen Magnetfelds durch eine Folge aus Radiofrequenzspulen ersetzt, die die Spins in der Streuebene umklappen (π-Flip) und die jeweiligen Bereiche ohne Magnetfeld scharf begrenzen. In diesem Aufbau gibt es keine klassische Spin-Präzession, jedoch ergibt sich aus der Wechselwirkung des Spins mit den oszillierenden Resonanzfeldern ein Phasenwinkel, der zur Flugzeit des Neutrons im Nullfeldbereich im Verhältnis steht. Dieser Aufbau wurde 2004 am Dreiachsenspektrometer TRISP an der Forschungs-Neutronenquelle Heinz Maier-Leibnitz (FRM II) realisiert und bietet damit das für diese Arbeit nötige NRSE mit thermischen Neutronen.

NRSE Messungen liefern im Ergebnis die Fourier-Transformierte der Spektrallinie einer Anregung. Harmonische Anregungen haben eine lorentzförmige Spektralform mit voller Halbwertsbreite 2Γ. In der Polarisation äußert sich dies als exponentieller Abfall derselben. Gibt es zwei benachbarte Moden, so zeigt das Polarisationsprofil eine Schwebung, die von der Gewichtsverteilung zwischen den Peaks und der Distanz zwischen deren Zentren abhängt.

A.2. Spektrallinien akustischer Phononen nahe der Energielücke in Nb und Pb

Bisher wurden mit der NRSE-Methode Linienbreiten in den transversal-akustischen Phononenzweigen in den konventionellen BCS-Supraleitern Nb und Pb im normalleitenden und supraleitenden Zustand gemessen [20]. Die Elektron-Phonon-Wechselwirkung ist bei niedrigen Temperaturen die dominante Ursache der Linienverbreiterung. Im Suprazustand wurde wie erwartet bei der Phononenenergie, die der Energielücke $2\Delta(T)$ entspricht, eine Diskontinuität in den Linienbreiten beobachtet. Phononen mit geringerer Energie sind nicht imstande, Elektronen über die Energielücke hinweg anzuregen, und leben deshalb länger als im Normalzustand.

Tatsächlich ist die Spektrallinie jedes einzelnen akustischen Phonons an verschiedenen Stellen im Bezug auf $2\Delta(T)$ unterschiedlich von der diskutierten Renormalisierung betroffen, was eine Linienformänderung verursacht [25]. Dieser Energielückengrenzeffekt wurde zuerst in den Nickelborokarbiden [24] beobachtet und als nicht signifikant eingestuft, außer unter extremen Bedingungen. Da neuere Neutronenstreudaten aus konventioneller

Dreiachsenspektroskopie an einem transversal-akustischen Zweig in Nb jedoch ebenfalls eine entsprechende Asymmetrie zeigten (Weber und Pintschovius, Ref. 26), stellt sich die Frage, wieso dies nicht schon früher in den NRSE Messungen erkannt wurde: Hier wurden keine Abweichungen des exponentiellen Abklingens der Polarisation beobachtet.

In dieser Arbeit werden nun diese NRSE Daten mit den entsprechenden Dreiachsendaten in Einklang gebracht. Zu diesem Zweck wurden Spin-Echo Polarisationsabklingprofile neu gemessen, mit verbesserter Impulsauflösung und über eine größere Spin-Echo Zeitskala. Die Polarisationsabklingprofile und Linienbreiten im Suprazustand werden anhand der Beschreibung von Allen *et al.* [25], die auf der BCS-Theorie basiert, ausführlich analysiert. Die Verschiebungen des Erwartungswerts der Spektrallinie im Vergleich zum Normalzustand werden den bereits vorhandenen und neuen NRSE Daten entnommen, sowohl für Nb als auch Pb. Dies ergibt zusammengenommen ein vollständiges Bild der Phononenrenormalisierung, anhand deren die Größe der Energielücke in verschiedenen kristallographischen Richtungen bestimmt werden kann.

A.2.1. Ergebnisse und Diskussion

Abbildung A.1 zeigt die effektiven Spektrallinien der $(\xi 00)$T Phononen in Nb für $\xi = 0.16$, 0.17 und 0.18 reziproke Gittereinheiten (r.l.u.) im Normal- und Suprazustand, nachdem die dreidimensionale Dispersion und die Auflösung der NRSE Messung mit berücksichtigt wurden. Die Dispersion im Normalzustand, ω_n, beruht auf Born-Von Kármán-Fits von am TRISP aufgenommenen Dreiachsendaten. Die Linienbreiten im Normalzustand wurden in einer ersten Näherung proportional zu ω_n gesetzt, $\Gamma_n = 0.02\omega_n$. Die effektiven Spektrallinien sind auch oberhalb der Sprungtemperatur $T_c = 9.3\,\mathrm{K}$ wegen der Krümmung der Dispersion leicht asymmetrisch. Die Spektrallinien im Suprazustand wurden aus denen des Normalzustands mit Hilfe der Theorie von Allen *et al.* [25] berechnet. Es wurde eine typische BCS-Temperaturabhängigkeit der Energielücke mit einem Sättigungswert $2\Delta_0 = 3.15\,\mathrm{meV}$ angenommen. Die Resonanz unterhalb von 2Δ verschmilzt wegen der endlichen Energieauflösung mit dem Rest-Phonon oberhalb von 2Δ.

Während die zugehörigen Polarisationsprofile oberhalb von T_c ein Exponentialverhalten zeigen, weicht die Kurve bei $T = 3.5\,\mathrm{K}$ vor allem für $\xi = 0.17$, bei dem die Energie des akustischen Phonons den Energielückenrand kreuzt, von einer Exponentialkurve ab. Dies macht sich deutlich im Verhältnis P_{sc}/P_n zwischen den beiden Kurven bemerkbar. P_{sc}/P_n ist zudem unabhängig von Datenkorrekturen hinsichtlich der Probenkristallinität und der instrumentellen Unvollkommenheit, da diese Faktoren sich im Quotient annulieren. Die Simulation bei $\xi = 0.16$ im Suprazustand ist offensichtlich nicht im Einklang mit den Daten, ebenso wie bei $\xi < 0.16$ (nicht gezeigt). Dies lässt sich mit einer Restlinienbreite unterhalb der Energielücke erklären: Die Polarisation klingt dadurch schneller ab als vorhergesagt. Die Quelle der Restlinienbreite ist uneindeutig. Bei $\xi = 0.17$ lässt die statistische Ungenauigkeit der Daten keine Unterscheidung zwischen eine gerade P_{sc}/P_n-Linie und der
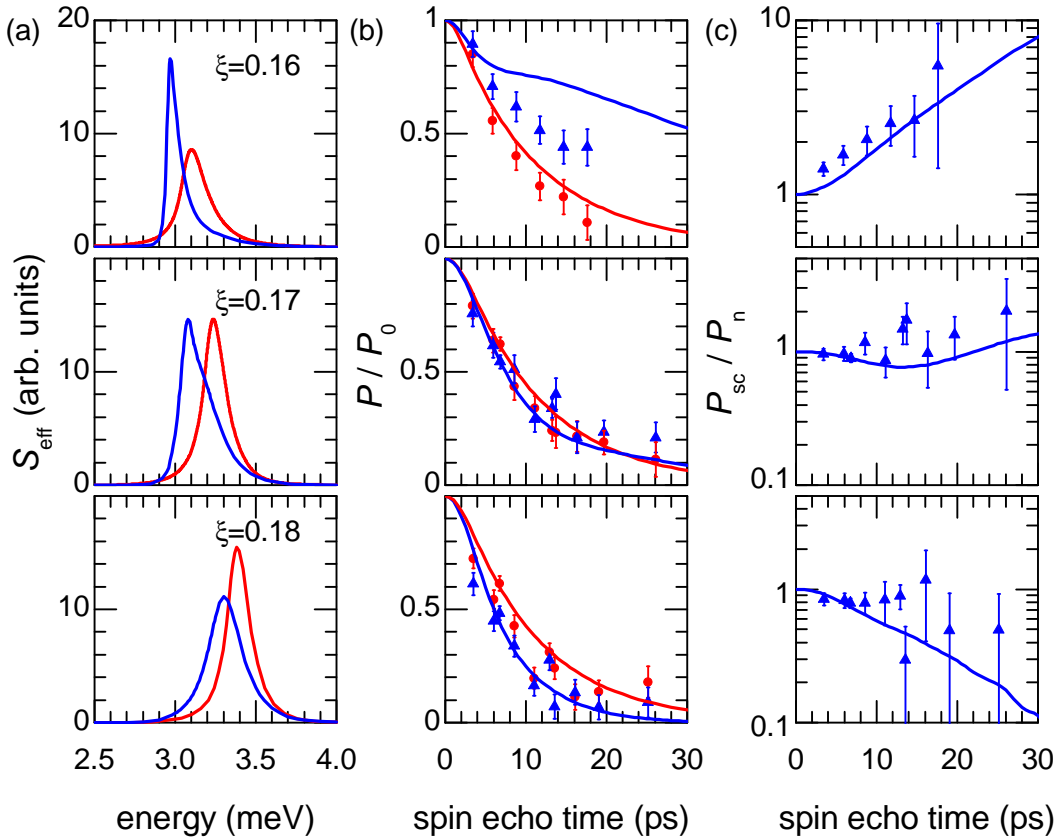
Figure A.1.: *(a) Simulierte Linienform der* $(\xi 00)T$ *Phononen in Nb für* $\xi = 0.16$, 0.17 *und*
0.18 *r.l.u. im Normal- und Suprazustand unter Berücksichtigung der experimentellen*
NRSE-*Auflösung. Rote (blaue) Kurven beziehen sich auf* $T = 12\,K$ $(T = 3.5\,K)$. *Für*
die Simulation wurde $\Gamma_n/\omega_n = 0.02$ *und* $2\Delta_0 = 3.15\,meV$ *benutzt. (b) Zugehörige*
Polarisationsprofile und experimentelle Daten (Symbole). Die Daten wurden um
den nicht durch die intrinsische Linienbreite verursachten Polarisationsabbau kor-
rigiert, z.B. die aus der Mosaizität der Probe und der Krümmung der Dispersion im
Normalzustand verursachten Effekte. (c) Verhältnis P_{sc}/P_n *der Polarisationsprofile*
(logarithmische Skala).

gezeigten Kurve zu. Demnach können keine Rückschlüsse auf die Linienform gemacht
werden. Die NRSE Daten stehen also zwar nicht im Widerspruch zu den Dreiachsendaten
von Weber und Pintschovius, sind aber auch nicht direkt bestätigend.

Abbildung A.2 zeigt die gemessenen Linienbreiten (zum Teil bereits in der Doktorarbeit von
P. Aynajian veröffentlicht [20]) und die Energieverschiebungen der niedrigsten akustischen
Phononen im Normal- und Suprazustand in verschiedenen kristallographischen Richtungen
in Niob und Blei. Die Linienbreiten in Nb (100)T wurden erneut gemessen. Da die
Linienformänderung im Suprazustand unerheblich ist, wurden die experimentellen Polari-
sationsdaten mit Exponentialfunktionen gefittet. Die simulierten Daten im Suprazustand
(durchgehende Kurve, Datenpunkte als Quadrate) wurden generiert, indem die effektive
Spektralfunktion und der Polarisationsabfall jeweils wie in Abb. A.1 gezeigt berechnet

wurden. Die Polarisationskurve wurde im experimentell zugänglichen Bereich mit einer Exponentialfunktion gefittet.

Das qualitative Verhalten stimmt mit den Voraussagen von Allen *et al.* überein. Während die Linienbreite unterhalb der Energielücke schmäler als im Normalzustand und oberhalb der Energielücke breiter ist, zeigt die Differenz der Schwerpunkte der jeweiligen Spektralverteilungen ein Minimum in der Nähe von 2Δ. Der Erwartungswert der Spektralverteilung liegt im Suprazustand niemals höher als im Normalzustand.

Bei $3.5\,$K ist der Sprung von Γ_s/Γ_n nahe dem Wellenvektor $\mathbf{q}_{2\Delta}$ scharf und nur durch die Auflösung verbreitert. Für vereinzelte Messungen bei höheren Temperaturen $< T_c$ stimmt dies jedoch nicht mehr, hier versagt die Theorie von Allen *et al.* In Tunnelmessungen wird gewöhnlicherweise die Dynes-Gleichung zur Beschreibung der Lücke benutzt, wobei eine phänomenologische temperaturabhängige Verbreiterung eingesetzt wird. Neben einer Reihe vorgeschlagener messtechnischer Begründungen wurde kürzlich demonstriert, dass eine komplexwertige Energielücke, deren Imaginärteil der Lebensdauer der Quasiteilchen am Lückenrand entspricht, eine solche Änderung der BCS-Energielücke mikroskopisch rechtfertigt [79, 80].

Weit unterhalb des Rands der Energielücke sind die Linienbreiten sowohl in Nb als auch Pb in verschiedenen Kristallrichtungen größer Null. Im (110)T1-Zweig in Pb zeigen die Linienbreiten unterhalb der Energielücke einen Peak, der einem im Normalfall kinetisch verbotenen Drei-Phononen Zerfall zugeschrieben wurde. Dies ist im Einklang mit einer beobachteten anomalen Dispersion, ähnlich wie in ^{4}He. Die sonstigen Linienbreiten könnten bedingt durch nicht-elektronische Wechselwirkungen ebenfalls endlich sein. Verunreinigungen neigen dazu, die Differenzen in der Selbstenergie zu verwaschen [81]. Da die Datenanalyse auf gemessenen Werten, u.A. der Dispersionskrümmung und der Mosaizität der Probe, basiert und sich als Funktion von $\mathbf{q}$ tendenziell langsam ändert, ist es unwahrscheinlich, dass den endlichen Linienbreiten eine unvollständige Korrektur zugrunde liegt. Eine tatsächlich vorhandene Zustandsdichte unterhalb 2Δ wäre nicht im Einklang mit der Theorie von Allen *et al.*

Die relative Verbreiterung der Linienbreiten oberhalb der Energielücke ist bemerkenswert niedrig im Falle von Pb (110)T1. Es kann nur vermutet werden, dass ein Teil der verzeichneten Linienbreite nicht durch Elektron-Phonon (e-ph) Wechselwirkungen verursacht wird. Dies bedeutet, dass die Kohn-Anomalie weniger ausgeprägt ist als zunächst angenommen.

Die Energielücke 2Δ kann anhand des Sprungs in den Linienbreiten festgelegt werden, wobei der Punkt benutzt wird, wo $\Gamma_s(\mathbf{q})$ über $\Gamma_n(\mathbf{q})$ hinaus schießt. Die Energie-Erwartungswert-Änderung liefert einen zusätzlichen Anhaltspunkt.

Die Linienformänderungen haben keinen Einfluss auf die gefundene Gleichheit der Kohn-Anomalien und der Energielücken im Suprazustand, die im nächsten Abschnitt besprochen werden.
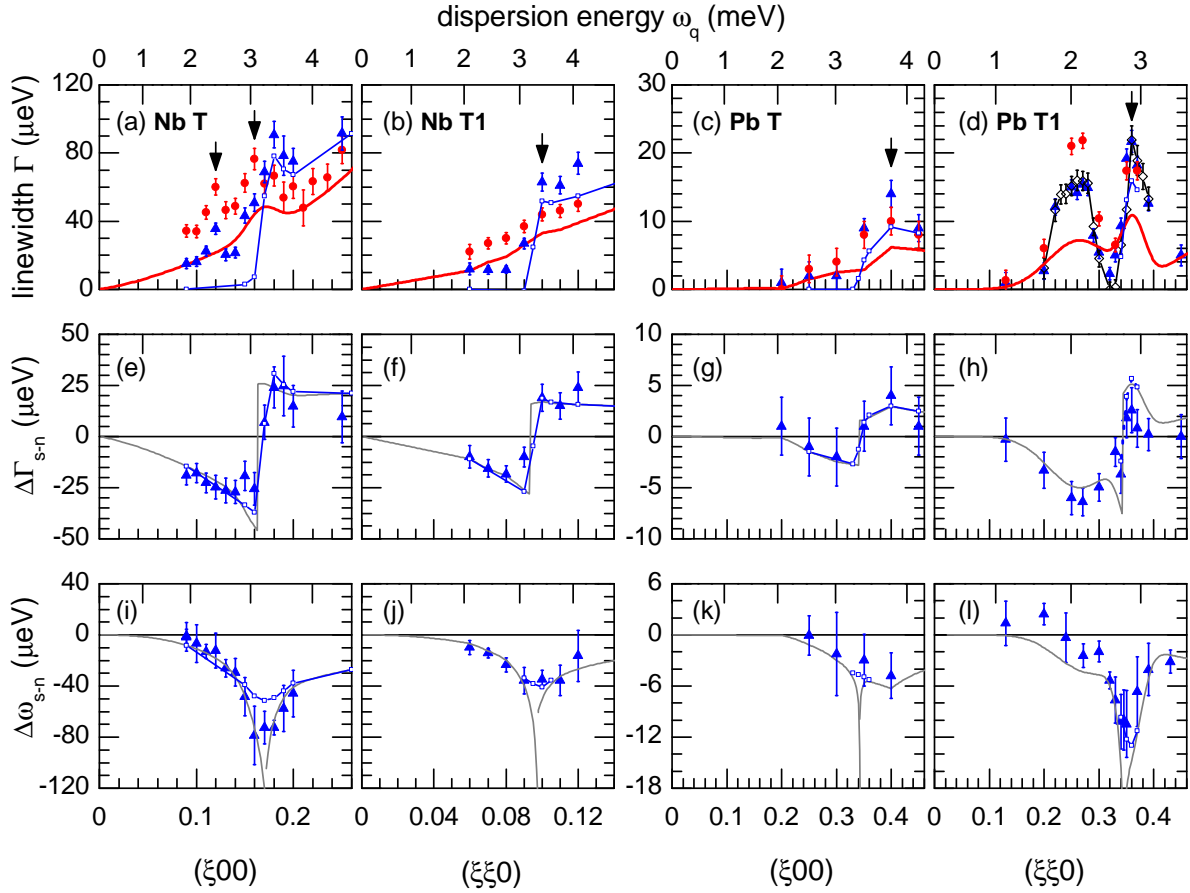
Figure A.2.: *(a-d) Experimentelle Linienbreiten bei $T = 3.5\,K$ (Dreiecke), $T = 0.5\,K$ (Diamanten) und oberhalb von T_c, bei $T = 12\,K$ und $10\,K$ in Nb resp. Pb (Kreise). V.l.n.r.: Nb $(100)\,T$ und $(110)\,T1$, Pb $(100)\,T$ und $(110)\,T1$. Die zugehörige Phononenenergie im Normalzustand ist auf den oberen Achsen eingezeichnet. Rote Linien sind Modelle für den Teil der Linienbreiten, der im Suprazustand renormalisiert ist. Durchgezogene Kurven mit Datenpunkten als Quadrate zeigen das entsprechende Verhalten nach der BCS-Renormalisierung von Allen et al., wobei die NRSE-Auflösung berücksichtigt wurde. (e-h) Differenzen zwischen Supra- und Normalzustand. Verbundene Vierecke richten sich nach dem Fall, dass nur der in den Modellen in (a-d) gezeigte Teil der experimentellen Linienbreiten renormalisiert ist. Die grauen Linien lassen die Auflösung außer Acht. (i-l) Energiedifferenz zwischen den spektralen Schwerpunkten im Supra- und Normalzustand. Symbole und durchgezogene Linien beschreiben die Energiedifferenz mit resp. ohne Auflösung.*

A.3. Kohn Anomalien und die Energielücke im Suprazustand in Tl-Pb-Bi

Obwohl allgemein anerkannt wird, dass konventionelle BCS Supraleiter mit s-Wellen-Symmetrie gut verstanden sind, wird die *ab initio* Berechnung der Sprungtemperatur T_c dadurch erschwert, dass die Energielücke an verschiedenen Stellen der Fermioberfläche verschiedene Werte annimmt [84]. Ein Phänomen, das mit NRSE an den niedrigsten transversal-akustischen Phononenlinienbreiten in Pb und Nb beobachtet wurde, deutet jedoch darauf hin, dass die gesättigte Energielücke $2\Delta_0$ in einer unerwarteten Art mit der Fermioberflächentopologie verbunden sein könnte. Eine zentrale Rolle nehmen dabei die Kohn-Anomalien (KA) ein, die als Knickstelle in der Phononendispersion und als Peaks in der Linienbreite auftauchen können. Sie entstehen durch erhöhte Wechselwirkung mit Valenzelektronen wenn der Wellenvektor $\mathbf{q}_{KA}$ substanzielle Teile der Fermioberfläche verbindet. Das von Aynajian [19] beobachtete Phänomen besagt, dass falls akustische Phononen mit Energien nahe $2\Delta_0$ einer KA unterliegen, sich die Lücke auf den entsprechenden Teilen der Fermioberfläche an die Energie $\hbar\omega_{KA}$ dieser Phononen anpasst. Die beteiligten Anomalien werden nicht von *ab initio* Dichtefunktionaltheorie-Rechnungen innerhalb der lokale Dichtenäherung (engl. DFT-LDA) reproduziert. Die Temperaturunabhängigkeit von $\mathbf{q}_{KA}$ und die starke $\mathbf{q}$-Abhängigkeit des Peaks in den Linienbreiten zeigen, dass es sich dennoch um Kohn-Anomalien handelt. Es gibt geeignete Verschachtelungsmöglichkeiten der Fermioberfläche (engl. *nesting*), die dies erklären [22].

Die Frage ist, ob das Phänomen des "Einrastens" der Energielücke allgemeingültig ist. In dieser Arbeit werden dazu die Dispersion und Linienbreiten des niedrigsten (110)T1 transversal-akustischen Zweiges in Blei mit geringfügigen Beimischungen von Wismuth resp. Thallium gezeigt. Tl, Pb and Bi sind Nachbarn im Periodensystem, so dass ihre Legierungen eine allmählich zunehmende Elektronenkonzentration und damit einen steigenden Fermi-See sowie eine zunehmende e-ph-Kopplungsstärke zeigen. Da die Energielücke in dieser Arbeit aus Literaturdaten entnommen wird, ist es entscheidend, das präzise Verhältnis der Komponenten in den untersuchten Teilen der Proben zu messen, weshalb diese mit einer Prompten-Gamma Aktivierungsanalyse (PGAA) bestimmt wurden.

A.3.1. Ergebnisse und Diskussion

Die Dispersionskurven der niedrigsten transversal-akustischen Phononenzweige in Richtung (110) in den beiden Bi-dotierten Proben im Vergleich mit reinem Pb [19] bei 10 K, oberhalb T_c, sind in Abb. A.3 gezeigt. Die Form der einzelnen Kurven ist ähnlich, jedoch mit zunehmender Wismuthgehalt zu höheren Wellenvektoren hin verschoben. Die Kurven fallen in der Nähe von $(0.55, 0.55, 0)$ zusammen. Die Energie an der Zonengrenze (nicht gezeigt), neigt im Tl-Pb-Bi-System wie schon aus früheren Experimenten bekannt [8, 87]
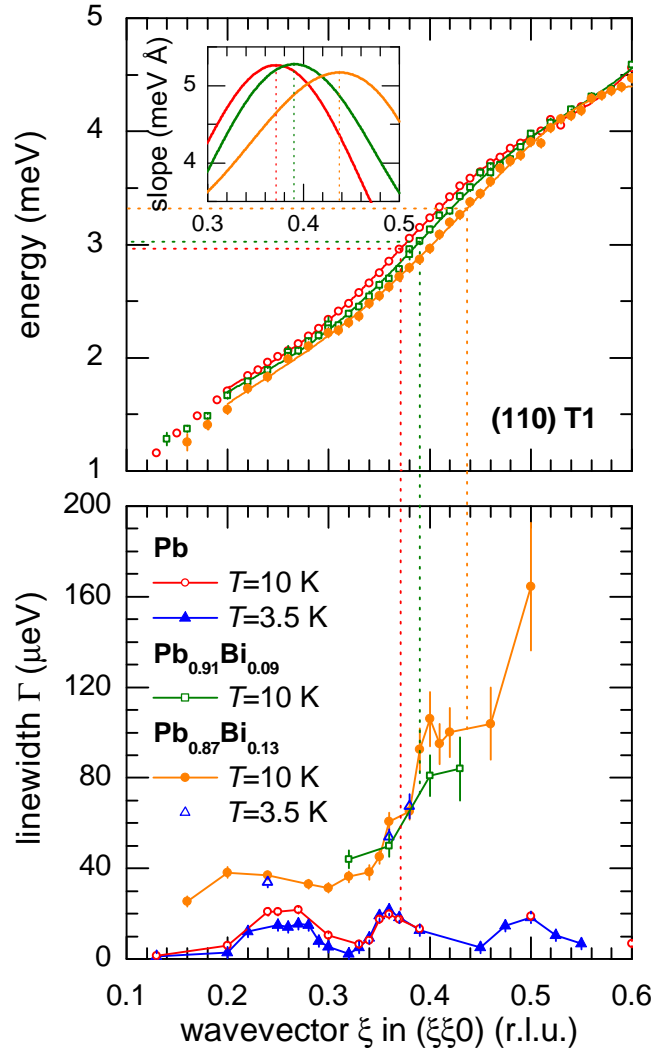
Figure A.3.: *Dispersion (oben) und intrinsische Linienbreiten (unten) des* (110) *T1 Phononen-zweiges in reinem Pb und in den beiden Pb-Bi Proben. Die Dispersion wurde im Bereich* $0.2 - 0.6\,r.l.u.$ *mit einem 5-Parameter Born-Von Kármán-Modell gefittet. Die jeweilige Position der einzelnen Knickstellen nahe* $\xi \sim 0.4\,r.l.u.$ *wurde anhand der Steigung der Fits bestimmt (Inset).*

dazu, mit zunehmender Anzahl an Elektronen n pro Atom abzunehmen. Während das Phononenspektrum insgesamt weicher wird, nimmt die e-ph Kopplungskonstante λ zu [85].

Die mit NRSE gemessenen Linienbreiten, unten im Bild, zeigen für reines Blei [19] drei ausgeprägte Peaks (teilweise bereits gezeigt in Abb. A.2). Der Peak bei der niedrigsten Energie bleibt im supraleitenden Zustand bei $T = 3.5\,K$ weitgehend unverändert. Die Energien sind hier nicht groß genug sind um Quasiteilchen über die Energielücke $2\Delta(T)$ hinweg anzuregen. Diese Phononenverbreiterung stammt stattdessen aus spontanem (fast) kollinearen innerzweiglichen Phononenzerfall. Die anderen beiden Peaks in der Linienbreite

von reinem Blei sind Kohn-Anomalien, die sich aus einer Fermioberflächenverschachtelung ergeben. Keiner der Peaks wird von *ab initio* LDA-Rechnungen erfasst [19].

Die KA in reinem Pb, die um $\xi_{KA} = 0.360 \pm 0.010$ r.l.u. und $\hbar\omega_{KA} = 2.85 \pm 0.10$ meV zentriert ist, zeichnet sich als aufwärts gerichtete Knickstelle in der Dispersion ab. Der Punkt der größten Steigung ist von gepunkteten Linien markiert, die auch durch das untere Panel gezogen sind. Die Knickstellen in beiden Legierungen sind genauso ausgeprägt wie im reinen Material, was darauf hindeutet, dass die Fermioberfläche ausreichend gut definiert ist und dass die Voraussetzungen für das Nesting weiterhin vorhanden sind. Indem das Ferminiveau des Bleis durch Legieren mit Wismuth modifiziert wird, verschiebt sich die Knickstelle erwartungsgemäß zu höheren ξ-Werten.

In den Legierungen sind die Knickstellen in der Dispersion jedoch nicht von deutlichen Peaks in den Linienbreiten begleitet. In beiden Proben steigen die Linienbreiten im Bereich $0.36 - 0.40$ r.l.u. von ca. $40\,\mu$eV bis ca. $100\,\mu$eV an. Von den wenigen Datenpunkten bei $T = 3.5$ K kann rückgeschlossen werden, dass die Renormalisierung im Suprazustand unerheblich ist, und folglich dass die Mehrzahl der Phononenzerfälle nicht von e-ph Wechselwirkung herstammt. Die willkürlich ersetzten Atome in den Legierungen brechen die Translationssymmetrie, so dass die elektronische Bandstruktur und die Phononendispersion verblassen. Weil Massenunordnung in den Legierungen keine größere Rolle spielt als in reinem Blei, das mehrere natürliche Isotope hat, liegt die Hauptquelle der Verbreiterung in Kraftkonstanten-Unterschieden und dem Einfluss von Verspannungen in der lokalen Umgebung verschiedener willkürlicher Konfigurationen eines Clusters. Die von Haverkort *et al.* [89] entwickelte Dichtefunktional-Superzellennäherung lässt Zufälligkeiten im Verunreinigungsanteil zwischen Multizellenclustern zu. Eine Machbarkeitsstudie hat gezeigt, dass es zur Zeit nicht ökonomisch ist, mit dieser Methode die von einem $\sim 10\%$-Anteil von zufallsbedingten Bi-Substitutionen verursachten Phononen-Linienbreiten zu berechnen [90].

Die Energielücke in reinem Blei, $2\Delta_{(110)} = 2.82 \pm 0.06$ meV, wurde den Linienbreiten-Daten entnommen, indem die Änderung der Linienbreiten im Suprazustand verglichen mit dem normalleitenden Zustand ausgenutzt wurde. Da die Änderung der Linienbreiten im Suprazustand in den Legierungen insignifikant ist, werden die impulsgemittelten Werte der Lücke aus der Einelektron-Tunnelstrom durch dünnen Aluminium-Aluminiumoxid-Bleilegierung-Schichten [85] benutzt. Die impulsgemittelte Lücke in Pb, 2.80 meV, stimmt mit $2\Delta_{(110)}$ überein, so dass die Anisotropie nicht berücksichtigt werden muss. Die Energielücke steigt mit zunehmender Elektronenkonzentration für dieses System in Übereinstimmung mit der Eliashberg-Theorie. Die Werte von $2\Delta_0$ und $\hbar\omega_{KA}$ in Vergleich mit der Valenzelektronenzahl n in den Legierungen werden in Abb. A.4 gezeigt. Der untere Wert der Tl-dotierten Probe für $\hbar\omega_{KA}$ ist an TRISP gemessen worden, während der obere Wert am kalten-Neutronen-Dreiachsenspektrometer Panda gemessen wurde: Obwohl das qualitative Verhalten der beiden gemessenen Dispersionskurven identisch ist, weichen sie aus bisher unerklärtem Grund mit zunehmendem Quasi-Impuls voneinander ab. Für jede der einzelnen Legierungen bleibt der impulsgemittelte Betrag der Energielücke aus
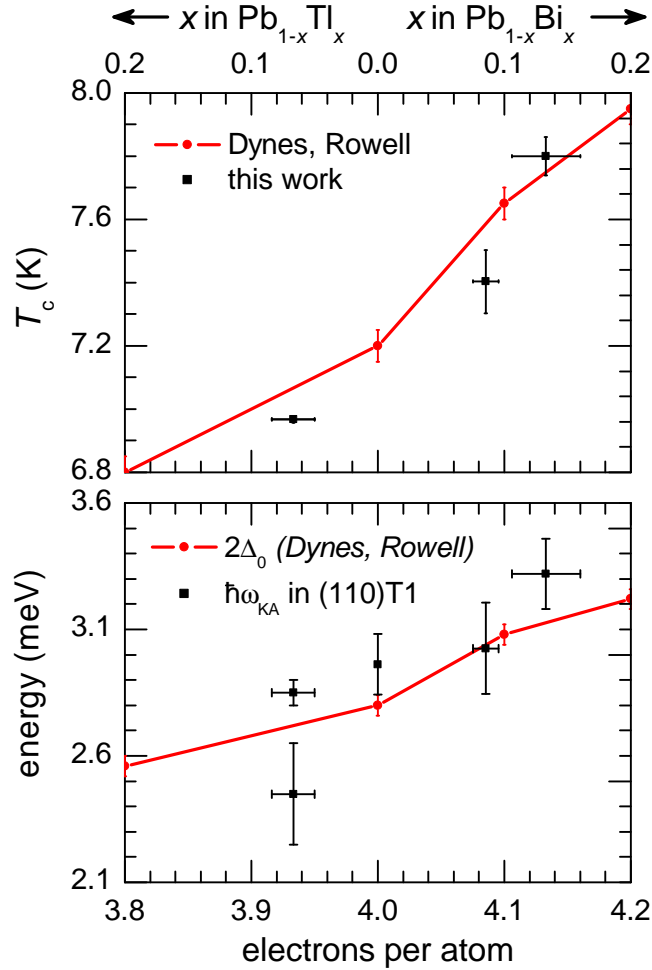
Figure A.4.: *Oben: Sprungtemperatur der Proben (schwarze Symbole) verglichen mit Daten aus Ref. 85 (rote Linie). Die Zahl der Valenzelektronen n ergibt sich aus dem mittels* PGAA *bestimmten Beimischungsverhältnis x (obere Skala). Unten: Vergleich der Phononenenergie bei der* KA *aus Abb. A.3 (schwarze Symbole) mit der impulsgemittelten Energielücke* $2\Delta_0$ *[85] (rote Linie). Fehlerbalken der Daten aus der Bezugsquelle sind auf der typischen Breite des Übergangs und der Reproduzierbarkeit der Energielücke basiert.*

Tunnelmessungen für die jeweilige Legierungskonzentration nahe der Energie an der Stelle der Kohn-Anomalie im (110)T1-Zweig.

Abb. A.4 zeigt außerdem die anhand des Meißner-Effekts gemessene Temperatur T_c, bei der die Supraleitung einsetzt, als Funktion von n verglichen mit Daten aus Ref. 85. Die Fehlerbalken von T_c variieren wegen des gewählten Temperaturgradienten während der Messung. Es bedeutet nicht, dass der eigentliche Übergang weniger rasch stattfindet. Die Werte stimmen gut mit der Literatur überein.

Ohne das insgesamte Erweichen der Phononenspektra würde die Energie der KA weiter ansteigen als die Energielücke. Es ist dieses empfindliche Gleichgewicht, das die Hypothese des "Einrasten" der Energielücke, möglicherweise jenseits der anerkannten Theorie der Supraleitung, unterstützt. Prinzipiell könnte die Kraft dieses Einrastens unter widrigeren Bedingungen getestet werden, z.B. in mit Molybden oder Zirkon dotiertem Niob, da sich der relevante Nestingvektor in diesem System in Richtung (001) mit zunehmender Sprungtemperatur zum Ursprung hin bewegt. Die Herausforderung ist jedoch, die gesteigerten Linienbreiten der akustischen Phononen in Legierungen als Funktion des Wellenvektors quantitativ zu bestimmen, damit die e-ph-Wechselwirkung von anderen Effekten unterschieden werden kann.